CHARGE-TRANSFER AND OTHER EXCITONIC STATES IN CONJUGATED POLYMER:FULLERENE BLENDS - IMPLICATION IN PHOTOVOLTAICS

A Dissertation

presented to

the Faculty of the Graduate School

at the University of Missouri-Columbia

In Partial Fulfillment

of the Requirements for the Degree

Doctor of Philosophy

---

by

DHANASHREE MOGHE

Dr. Suchi Guha, Dissertation Supervisor

MAY 2014

The undersigned, appointed by the dean of the Graduate School, have examined the dissertation entitled

CHARGE TRANSFER AND OTHER EXCITONIC STATES IN CONJUGATED POLYMER:FULLERENE BLENDS - IMPLICATION IN PHOTOVOLTAICS

presented by Dhanashree Moghe

A candidate for the degree of Doctor of Philosophy

and hereby certify that, in their opinion, it is worthy of acceptance.

Professor Suchismita Guha

Professor Ping Yu

Professor Carsten Ullrich

Professor H. R. Chandrasekhar

Professor Rainer Glaser

Dedicated to my beloved parents

ACKNOWLEDGEMENTS

I would like to express my sincerest gratitude to my advisor, Dr. Suchi Guha: whose enthusiasm for research and unsurpassed knowledge, offered me the opportunity to work on various research projects. Without her patience, guidance, insightfulness and encouragement, this task would not have been accomplished.

I would like to thank Dr. Ping Yu for his immense help and valuable discussions regarding the setting of Fourier transform infrared spectrometer for photocurrent spectroscopy. In addition, I am very thankful to Dr. Samiullah for all his help with the photoinduced absorption measurements and his insights on various topics during our discussion. Further, I am thankful to Dr. Satish Patil and his students for providing us with the samples. I would also like to thank Dr. Carsten Ullrich for his valuable inputs during the theoretical calculations. I extend my sincere thanks to all my committee members: Dr. Suchi Guha, Dr. Ping Yu, Dr. Carsten Ullrich, Dr. H. R. Chandrasekhar and Dr. Rainer Glaser, for giving me the opportunity to present my work.

I am deeply grateful to my parents, brother and sister-in-law for their unequivocal support and encouragement throughout my graduate studies at Mizzou. A special thanks to my adorable niece and nephew for the enthusiasm they show upon my visits and for making the stay during my PhD, memorable. Last but not the least, I extend my thanks to all my fellow colleagues in our lab for their prompt help, and my friends for making the period of my graduate study a wonderful and enriching experience.

TABLE OF CONTENTS

LIST OF TABLES

LIST OF ILLUSTRATIONS

LIST OF ABBREVIATIONS

BE	Binding energy
BHJ	Bulk hetrojunction
CP	Conjugated polymer
CT	Charge-transfer
CTC	Charge-transfer complex
D-A	Donor-acceptor
DPP	Diketopyrrolopyrrole
EQE	External quatum efficiency
FT	Fourier transform
FTIR	Fourier transform infrared
FTPS	Fourier transform photocurrent spectroscopy
HOMO	Highest occupied molecular orbital
Intra CT	Intramolecular charge-transfer
Inter CT	Intermolecular charge-transfer
ISC	Intersystem crossing
LPPP	Ladder-type poly para phenylenes
LUMO	Lowest occupied molecular orbital
MeLPPP	Methyl substituted LPPP
MQW	Multiple quantum well
NIR	Near-infrared

OPV	Organic photovoltaic
P3HT	Poly (3-hexylthiophene)
PC	Photocurrent
PCBM	Phenyl-C_{61}-butyric acid methyl ester
PCE	Power conversion efficiency
PhLPPP	Adiaryl (diphenyl)-substituted LPPP
PIA	Photoinduced absorption
RT	Room temperature
S_0	Ground state energy
S_1	Singlet state
T_1	Triplet state
T-T	Triplet-triplet
UV-Vis	Ultraviolet-Visible
WM	Wannier-Mott

ABSTRACT

Over the last few decades there has been tremendous progress in organic photovoltaics (OPVs), with efficiencies reaching over 10%. Still, many factors including the origin and the dynamics of charge carrier involved are debatable. New and sensitive techniques are constantly being devised to identify the origin of free charges. At the same time, lot of research has also been devoted to synthesize low bandgap material such that its absorption spectra overlap with that of the solar spectrum.

The most important hindrance in organic semiconductors is the formation of bound electron-hole (exciton) charge pair upon photoexcitation. Additional energy is required to dissociate the bound pair to generate free charges for photovoltaic application. The most popular and efficient way to dissociate excitons is to fabricate a bulk heterojunction solar cell, which comprises of a blend of at least two polymers: one donor and the other acceptor. It is very well established that the presence of fullerene (acceptor) helps in transfer of the negative charges from the donor polymer to fullerene, making the exciton slightly less bound. The nanometer scale islands further help in migration of charges.

A crucial aspect of our studies has been evaluating the role of various excitonic states such as charge-transfer and triplet excitonic states in device efficiencies. The focus of this work was on diketopyrrolopyrrole (DPP)-based donor-acceptor (D-A) type conjugated copolymers which have low bandgap energies and have been known to show high efficiency in organic photovoltaics. These copolymers have D-A unit present in the same chain, which lowers the optical bandgap of the material. Variation of either the donor or the acceptor fraction offers an option to tune the optical bandgap by using the same D-A

chromophores. The D-A configuration also results in the separation of positive and negative charges within the same polymeric chain, which is the intramolecular charge-transfer excitonic state. We analyze the intramolecular charge-transfer state using bias dependent absorption studies, which allowed us to estimate the binding energy of intramolecular exciton. Later, we performed density functional theory (DFT) and time dependent DFT calculations to identify the origin of the intramolecular exciton absorption.

Taking the copolymers as donor (and fullerene as acceptor) in an organic photovoltaic device, we probe the (intermolecular) charge-transfer states formed at the copolymer/fullerene interface. We utilize monochromatic photocurrent method and a highly sensitive (and fast) Fourier transform photocurrent spectroscopy technique to probe the intermolecular charge-transfer states in the device. Our analyses show that the optical bandgap difference between the copolymers and fullerene plays a pivotal role in stabilization/destabilization of charge-transfer states in copolymer-fullerene systems.

The triplet excitons are also known to play an important role in OPV efficiency. We probe the diffusion length of triplet exciton in ladder-type polymers by devising a simple, yet efficient method using optical modulation spectroscopy (photoinduced absorption spectroscopy). The diffusion length of triplet excitons is estimated to be almost three orders of magnitude more than the singlet excitons. Further, by implementing a 1D random-walk model to the photoinduced absorption data, we estimate diffusivities of the triplet exciton in our sample.

1.

INTRODUCTION

1.1 Conducting Polymers

With the discovery of organic semiconductors there have been tremendous advances in the synthesis and electronic application of conducting organic materials. The initial conductivities of organic crystal were almost four orders of magnitude less than doped inorganic semiconductors such as silicon. Around 1862, Henry Letheby prepared polyaniline which had shown conductive properties.[1] Though it's exact electronic properties were unknown at that time, its derivatives were used in textile printing and dyeing. Later melanin, a biological pigment and another derivative of aniline, showed properties of tunable conductivity. Due to the dark color of many organic polymers their application was limited to non-electronic application such as antistatic coating, additives to corrosive primers, and energy storage. In 1960's polyaniline-iodine complex were synthesized that showed conductivities of around 1 Scm^{-1}. By 1974, polyacetylene and polypyrrole were found to exhibit conductivities in the range of 5-30 Scm^{-1}. A major breakthrough was in 1977 with the results published on polyacetylene doped with halogen film with metallic luster showed conductivities close to several hundred Scm^{-1}.[2] Along with the electrical conductivities, several groups were involved in the application of the conducting polymers in photoconductivity.

Anthracene was the first organic crystal which showed photoconductivity.[3,4] In the late 1950s and 1960s the organic materials were also used as photoreceptors in imaging

systems. Photoconductivity was observed in many dyes, important biological molecules such as carotenes, chlorophylls and other porphyrins. Since the early 1990's conducting polymers were used in a variety of electronic devices such as in organic light emitting diodes (OLEDs), organic field-effect transistors (OFETs), solar cell etc. The initial polymers showed low solubility and stability, and hence, poor processing. Many of the current polymers are easily soluble in organic solvents such as dichlorobenzene and toluene. Hence, it is possible to create composites or blend polymers for thin film application.

This thesis describes the systematic optical and electrical studies performed on organic semiconductor in the solid state (thin films~100-200 nm) for application in organic photovoltaics. The chapters/sections have been arranged as follows: the next few sections in Chapter 1 introduce the type of polymers chosen and the nature of optical transitions in organic semiconductors. Chapter 2 describes the optical and optical-electrical assemblies for the present studies and the methods utilized to identify excitonic states in the organic semiconductors. It also gives an introduction of the working of an organic photovoltaic device, elaborates on the device structure and the device fabrication techniques. Chapters 3, 4, 5, and 6 discuss the experimental results and theoretical calculations-involving charge-transfer and triplet excitons in neat and blended polymer films. Finally, the summary and suggestions for future work are presented in Chapter 7.

1.2 Pi-Conjugated Polymers

There are four types of bonding found in solids. The ionic bond results from columbic attraction between ions and counter charges. The metallic bonds are also ionic in nature, but the negative charges are free mobile electrons which account for high conductivities in metals. The covalent bond formed due to sharing of electrons between neighboring atoms. Most commonly known covalent solids are diamond, silicon and germanium. The weakest of all is the van der Waals bonds. Because of the weak nature of van der Waals bonds the electronic properties of individual atom is mostly retained. Since organic semiconductor imply compounds consist of carbon, it is important to elaborate on the properties of atomic carbon.

The electronic configuration of a carbon atom is given by $1s^2 2s^2 2p^2$. It is possible to combine the one 2s and three 2p orbital in two ways. In one way, the 2s combines with three 2p to give four sp^3 hybridizations as shown in fig. 1.1(a). Another way is to combine 2s with p_x and p_y to give three sp^2, while leaving the p_z unaltered. The three sp^2 have a planar arrangement while the p_z orbital is perpendicular to the plane (fig. 1.1(b)). When the sp^2 orbital combines with 1s orbital of H atom a σ-bond is formed. When two p_z from each C atom combine as in shown in fig. 1.1(c), a highly localized electron density cloud results in the plane containing C and H atoms. It is termed as the double bonds or π bonds. In the case of aromatic compounds such as benzene the overlap of p_z orbital of each carbon is such that it generates high electron density above and below the plane, but not in the plane. The π-bonds in benzene are delocalized. An alternate single and double bond formed by out of plane overlap of p_z orbital is termed conjugation. The

conductivity in a conjugated polymer (CP) is the result of the delocalized π-electrons and the transitions from filled to unfilled π-orbital, are the π- π* transitions. The molecular orbitals i.e., π- π* are also the bonding-antibonding orbitals. Analogous to the valence-conduction band, the molecular orbitals are denoted by highest occupied molecular orbital (HOMO) and lowest unoccupied molecular orbital (LUMO). In this work we analyze different classes of π-conjugated polymers which have potential application in photovoltaics.

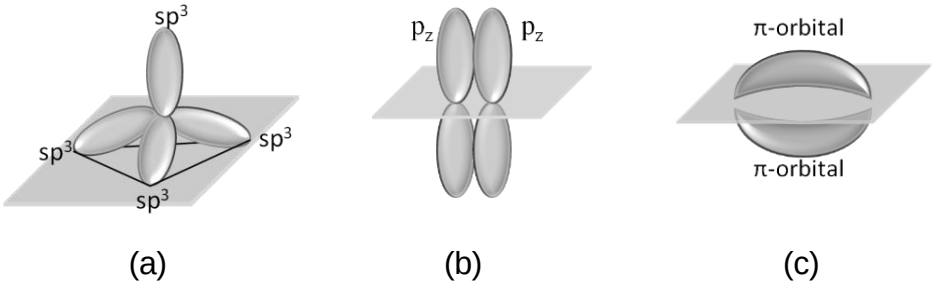

Figure 1.1(a) sp^3 orbital (b) p_z orbital and (c) π-orbital formed due to the overlap of p_z orbitals.

1.3 Excited States and Excitons

Compared to inorganic semiconductors (ε_r ~10), the dielectric constant of organic semiconductor polymers is small (ε_r ~2-4). Hence, excitations in the molecular crystal result in a bound electron-hole pair (exciton). The exciton can be categorized as (a) Frenkel (b) Wannier-Mott or (c) intermediate or charge-transfer (CT) exciton and is shown in fig. 1.2(b).[5] Frenkel exciton can be described as an electron-hole pair located on the same molecular site. It also diffuses as a pair. In simple terms, if the lattice constant of molecular crystal is a_L, the radius of Frenkel exciton would be less than a_L.

Typically, for organic crystals the radius of Frenkel exciton is < 5 Å. Here, the radius of exciton is defined as the average separation of the electron from its correlated hole. A Wannier-Mott (WM) exciton is shown in fig 1.2. The WM excitons are mostly detected in inorganic systems due to the high dielectric constant of the medium. Since the Coulomb force is inversely proportional to the dielectric constant, a high dielectric constant lowers the force of attraction between the electron and hole, increasing the separation between electron and the hole. The radius of the WM exciton is ~40-100 Å. The charge-transfer (CT) exciton, as shown in fig. 1.2 as (c), is encountered in organic systems, where the exciton radius is only few times the nearest-neighbor distance. The CT exciton is also characterized by the fact that the electron and hole are situated on two different molecular sites. As an example, the CT state (dashed circle) in anthracene is shown in fig. 1.2(b). Note that the positive and negative charges reside on two different chromophore sites.

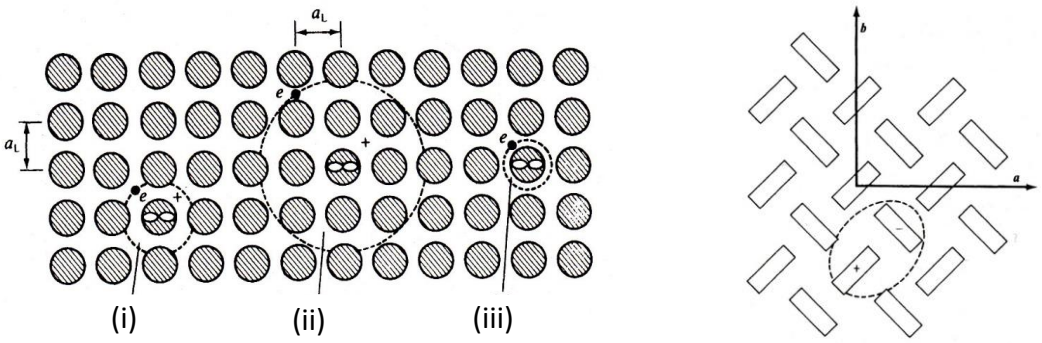

Figure 1.2 Schematics of exciton in organic semiconductors. (a) (i) Frenkel (ii) Wannier-Mott (iii) Charge-transfer (CT) exciton. (b) A CT state in an anthracene crystal.[Ref. 5]

Excitons with total spin S=0 (anti-parallel) are the singlet exciton (S_0), where as those with S=1 (parallel spins) are the triplet excitons (T_1). The different types of excitation process are shown in fig. 1.3.[6] The ground state, first singlet excited state, triplet ground state and higher triplet excited states, is represented by S_0, S_1, T_1 , T_N, respectively. The incident light will generate S_1 or higher singlet excitonic states. It is possible for the S_1 state to decay back to the S_0 state by either radiative or non-radiative (NR) emission. The radiative emission is the photoluminescence (PL) emission. If the triplet state is accessible via an intersystem crossing (ISC), then the lowest singlet state can depopulate to the T_1 state, leading to the formation of triplet excitons. In this thesis, the $T_1 - T_N$ or T-T absorption has been probed in ladder-type polymers using photomodulation spectroscopy. It is also possible for the S_1 state to depopulate to a low lying CT state. A central role in the photovoltaic process in the organic solar cells is played by CT complex states, which are intermediate steps between exciton dissociation at the heterointerface and free charge generation. In the work presented here, the CT states have been identified using photocurrent spectroscopy in a bulk heterojunction organic solar cell. The dissociation of the CT state results in formation of one negative and one positive charge. Since there is “mass” due to the coupling of the lattice vibrations associated with the charge, such charges are termed polarons. In fig. 1.3, the intra polaron absorption is represented by P.

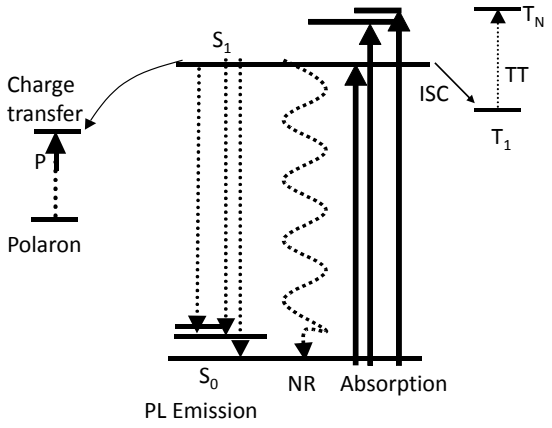

Figure 1.3 The possible transitions in an organic semiconductor upon optical excitations. [Ref. 6]

1.4 Materials

1.4.1 Poly (3-hexylthiophene) or P3HT

The chemical structure of P3HT monomer is shown in fig. 1.4(a). The hexyl group is attached to the thiophene group at position "3". The regio-regular (RR) P3HT with molecular weight 20,000-70,000 was purchased from American Dye Society (ADS). P3HT is an electron rich polymer with a planar structure leading to a close packed π-stacked backbone. It is found to have the ability to crystallize when annealed, that helps in the charge transport along the polymer chain.

1.4.2 Ladder-type polymers

The optical and electronic properties of conjugated polymers are highly dependent on the backbone geometry of polymer. The various rings (such as phenyl) in most of the conjugated polymers are linked by single C-C bonds which are prone to rotation or

twists. They have small conjugation length leading to structural defects which severely affect their optical and electronic properties. It is possible to introduce a double stranded molecule which introduces rigidity and a planar backbone to the polymer. Ladder-type poly para-phenylenes (LPPP) belong to such class of polymers. The rigidity is also reflected in their ability to show high degree of purity and lowering of the optical band gap due to delocalized π electrons along the polymer backbone. [7,8]

The ladder-type polymers studied in this work are methyl substituted LPPP (MeLPPP) and adiaryl (diphenyl)-substituted LPPP derivative (PhLPPP) as shown in fig. 1.4(b). It was found that a trace amount of Pd in the PhLPPP backbone results in a higher fraction of triplet excitons compared to MeLPPP at room temperature. The Pd concentration as estimated by inductively coupled plasma optical emission spectroscopy is less than 5 ppm for MeLPPP and less than 120–200 ppm for PhLPPP.

1.4.3 Diketopyrrolopyrrole (DPP) based copolymers and statistical copolymers

A very strong emphasis is being placed on achieving stable, low bandgap and enhanced molecular packing of conjugated polymeric semiconductors for an improved performance of organic optoelectronics. The requirement of low band gap material arises from the fact that photon flux from the sun varies with the wavelength (data from NREL).[9] Since most of the photon flux lies above 600nm, for a better performance of OPV, the solar spectrum emission must overlap with the absorption spectrum of the material in the infra-red region.[10,11] The low band gap materials or copolymers can be synthesized by introducing alternative electron rich and electron deficient units in the

polymer backbone. In general, copolymers can be broadly classified as alternating copolymers, periodic copolymers, block polymers, and statistical copolymer. The design of systems incorporating both donor and acceptor chromophore in the same chain are of particular interest for applications in field-effect transistors and OPVs since they have a high degree of tunability of their electronic and optical properties. Several works incorporating D-A and donor-acceptor-donor (D-A-D) units in oligomers/polymers have reported improved efficiencies in OPVs.[12-16]

Diketopyrrolopyrrole (DPP) containing copolymers have been used as high performance industrial pigment due to their thermal and photo-stability are now being considered for photovoltaic application.[17-22] Organic PVs based on DPP polymer show an overall PCE of 6.9%.[23] Copolymers of DPP that we have used in this work show p-type FET mobilities ~10^{-3} cm^2Vs^{-1} from spin coated film [20] and yield ~3% PCE when utilized in unoptimized solar cell.[21] DPP-based low bandgap materials are not just useful for device applications, but are designed to achieve environmentally stable organic semiconductors.[24] In the present work, the DPP based polymers used are poly{2,6'-4,8-dihexyloxybenzo[1,2-b;3,4-b]dithiophene-alt-2,5-dihexyl-3,6-bis-(4-phenyl-1-yl) pyrrolo [3,4c] pyrrole-1, 4-dione} (PDPP-BBT) and poly{2,60-4,8-dihexyloxybenzo[1,2-b;3,4-b]dithiophene-alt-2,5-dihexyl-3,6-bis(5-thiophen-2-yl) pyrrolo [3,4-c] pyrrole-1,4-dione} (TDPP-BBT), along with a set of DPP-based statistical polymers. The statistical copolymers have also shown applicability in OPVs. In the synthesis of copolymers, the same monomer or a set of comonomers can be combined to obtain molecular weight and copolymer sequence with different properties. Combining

different comonomers in random fashion, results in statistical copolymers.[25] The statistical copolymers have been designed to alter their band-gap and tune the morphology for controlling phase segregation.[26,27]

The synthesis of the DPP copolymers is discussed in references.[20,21,28] The chemical structure for PDPP-BBT, TDPP-BBT and statistical copolymers is shown in fig. 1.4(d), (e) and (f), respectively. Note the factor x in fig. 1.4(f). A higher value of x represents a higher value of DPP. Thus, Poly B has a higher DPP fraction than Poly A.

1.4.4 Phenyl-C_{61}-butyric acid methyl ester or PCBM

The modified fullerenes or C_{60} was first synthesized by Jan C. Hummelen et al. [29] with the aim of application in biological and photophysical studies. The chemical structure of one of the modified fullerene, PCBM, is shown in fig. 1.4(c). The electron mobility of PCBM is around 0.002 $cm^2\ V^{-1}\ s^{-1}$ which is almost an order of magnitude more than its hole mobility.[30] PCBM is soluble in most of the organic solvents (dichlorobenzene, toluene etc.). When blended with P3HT and annealed, it also forms an interpenetrating network with P3HT [31,32] and appropriate phase segregation with DPP-based polymer, which is desirable for photovoltaic applications.[33,34] The high electron mobility, relatively low-cost, and easy processing from solution, make it a suitable and the most widely used acceptor in the bulk heterojunction organic solar cells.

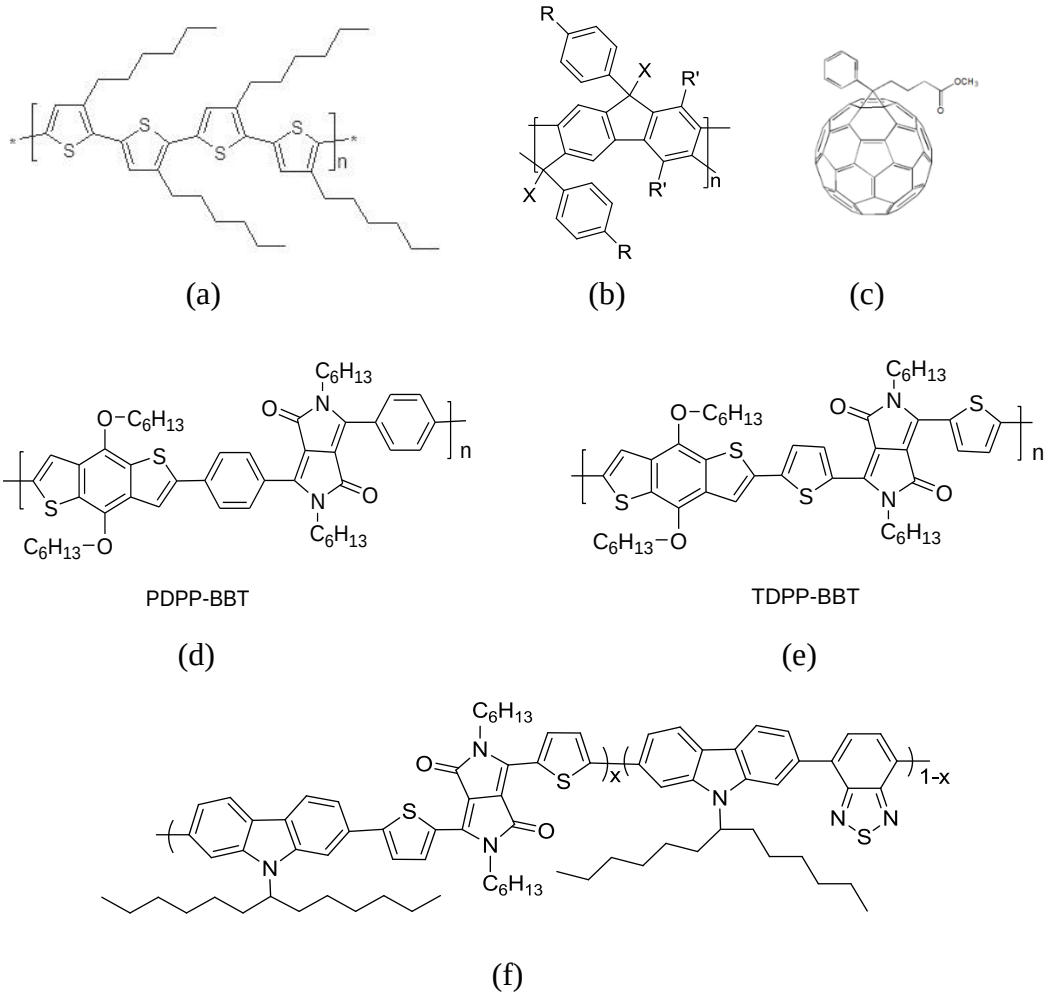

Figure 1.4 Chemical structure of (a) P3HT (b) X- methyl for MeLPPP and X- phenyl for PhLPPP (c) PCBM (d) PDPP-BBT (e) TDPP-BBT (f) Statistical copolymers where x= 0.25 (Poly A) and x=0.50 (Poly B).

2.

EXPERIMENTAL TECHNIQUES

For the work presented here, we have utilized optical: ultraviolet-visible (UV-Vis) and near-infrared (NIR) absorption spectroscopy along with electrical measurements. The UV-Vis provides an estimate of the S_1 band gap, while NIR has been utilized to provide information about low energy (such as T-T absorption). The optical modulation techniques: photomodulation and photocurrent spectroscopy, have also been used to gain access to weak transitions. Photocurrent spectroscopy was utilized to calculate the responsivity of OPV devices. Further, electrical characterization of solar cells was also performed. In the next few sections, we discuss each method in detail.

2.1 Absorption

The absorption is the simplest optical technique which is often utilized to get an estimate of the optical bandgap and absorption coefficient of a material. In amorphous organic polymers, the bandgap of material can be calculated from the onset of absorption from a solution or in a solid state (such as a thin film of few hundred nm). We utilized the absorption spectra of thin films of polymer to countercheck the stated bandgap of the materials provided.

The absorption coefficient can be calculated using the Beer-Lambert law. Consider light of intensity $I_0(\lambda)$ incident on a medium. The intensity transmitted through a uniform thickness t of medium, $I(\lambda)$ can be written as,

$$I(\lambda) = I_0 \exp(-\alpha(\lambda)t), \quad (2.1)$$

where, $\alpha(\lambda)$ is the spectral absorption coefficient. Simplifying Eq.2.1, for a uniform thickness of material,

$$\alpha(\lambda) = \frac{1}{t}\ln(\frac{I_0}{I(\lambda)}), \quad (2.2)$$

The absorption was measured using Shimadzu UV-2401 PC with the absorption setting with glass as a reference sample. The light source is a halogen lamp for the visible region and deuterium lamp for the ultra-violet region while the detector is photomultiplier R-928. When the absorption from the device structures was measured, the reference sample had exactly the same thickness of glass, ITO, PEDOT-PSS, and Ca/Al layers. To calculate the absorption curve, the instrument measures $I_0(\lambda)$ and $I(\lambda)$ through a reference sample and the actual sample simultaneously, and gives the final absorption coefficient spectrum time *t*. Since *t* is considered a constant, the obtained spectrum has same features as a true absorption spectrum.

2.2 Photomodulation Spectroscopy

Modulation spectroscopy is a very sensitive technique used to identify weak signal from a strong background. The optical response of a semiconductor, which includes absorption, reflection, and transmittance, may be monitored by modulation spectroscopic techniques. The modulation is a small repetitive perturbation which can be internal or external. The internal perturbation includes photomodulation of incident light obtained by modulating frequency, wavelength or amplitude modulation (AM) of incident light.

External perturbation includes electric field (such as electroabsorption or EA), temperature or strain. Modulation spectroscopy makes it possible to identify spectral features from a feature less spectra with high accuracy, even at room temperature.

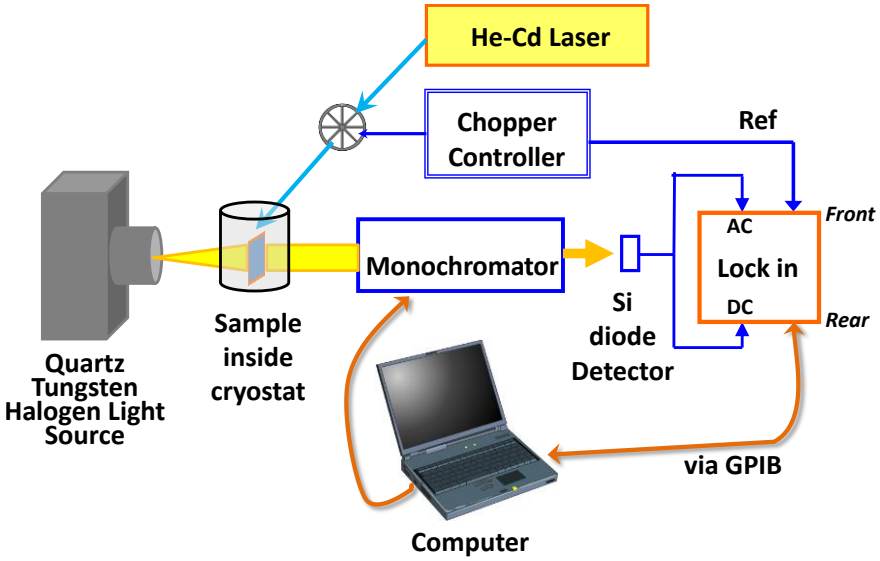

Figure 2.1 The pump-probe set up.

Photomodulation spectroscopy, also known as pump-probe technique has been used to identify charged and neutral excited states in a wide variety of material.[35] The assembly of the pump -probe technique generally involves a lock-in amplifier. The lock-in amplifier uses a phase-sensitive technique i.e. require a reference frequency to separate the perturbed (ac) from the steady state (dc) components. The SR810 amplifier can detect ac signal of even few nanovolts.

In our setup, a mechanical chopper chops the incident beam of light with reference frequency (ω_r). Since the lock-in is "referenced" at ω_r , the lock-in detects signal at ω_r .

To simplify, consider the reference signal as a sine wave at frequency ω_r. If V_{sig} is the amplitude of the signal, at time *t*

$$V_S(t) = V_{sig}\sin(\omega_r t + \theta_{sig}). \tag{2.3}$$

The phase-sensitive detector in the lock-in generates its own signal given by,

$$V_L(t) = V_{lock}\sin(\omega_L t + \theta_{lock}) \tag{2.4}$$

The SR810 amplifies $V_S(t)$ and then multiplies it with $V_L(t)$ using a multiplier. The resultant is,

$$V_{result}(t) = V_{lock}\sin(\omega_L t + \theta_{lock}) \times V_{sig}\sin(\omega_r t + \theta_{sig}). \tag{2.5}$$

Simplifying the above equation, we get,

$$V_{result}(t) = \frac{1}{2}V_{sig}V_{lock}\cos[(\omega_L - \omega_r)t + \theta_{sig} - \theta_{lock}] - \frac{1}{2}V_{sig}V_{lock}[\cos(\omega_r + \omega_L)t + \theta_{sig} + \theta_{lock}]. \tag{2.6}$$

$V_{result}(t)$ consists of two ac signals: one at $\omega_L - \omega_r$, and the other at $\omega_L + \omega_r$. If now $\omega_L = \omega_r$, we have,

$$V_{result}(t) = \frac{1}{2}V_{sig}V_{lock}\cos[\theta_{sig} - \theta_{lock}] - \frac{1}{2}V_{sig}V_{lock}[\cos(2\omega_r)t + \theta_{sig} + \theta_{lock}]. \tag{2.7}$$

The first (second) term is the dc (ac) signal. By suitable filters, the lock-in separates ac (front port e.g. "A") and dc (rear port e.g. AUX Port 1). In fig 2.1 the front/rear correspond to the front/rear interface of lock-in. Note: For mathematical simplicity, equation have been written in terms of $\omega(rad/\sec)$ and $\theta(rad)$. The lock-in will report frequency in as Hz and phase angle in degrees.

The setup for pump-probe technique is shown in fig. 2.1. A quasi pump-probe technique was used to measure the photoinduced absorption (PIA) spectrum from thin films in our work. PIA was measured using the 325 nm line of a He-Cd laser as the pump beam, modulated by a mechanical chopper. A 100 W quartz tungsten halogen lamp focused using a lens, was used as a probe beam. The sample is placed in the evacuated chamber (cryostat) and the transmitted light is dispersed through a Spectral Product CM110 monochromator. A silicon detector, Thorlabs DET110, was used to detect the transmitted light. The small changes (ΔT) in transmission were obtained by passing the signal from the detector to a preamplifier and then to a lock-in amplifier (SR810) referenced to the chopper frequency. The signal from the detector is fed to port A (front) which filters the ac signal (ΔT). The same detector signal is fed to rear port (AUX port 1) gives the dc component (T). All photomodulation spectra are given by $-\Delta T$ divided by the transmission (T). The SR810 lock-in amplifier can measure sine component of signal (X) and the vector magnitude (R) of the signal. The sine component of the amplitude depends on the reference frequency as well as on the phase difference between the signal and the lock-in reference oscillator. The R signal does not depend on the phase, but depends only on the reference frequency. Since, we are interested only in the amplitude of the periodic signal and not its phase, the lifetime and the photocurrent data was acquired by selecting R display of the lock-in amplifier.

2.3 Photocurrent Spectroscopy

2.3.1 Monochromatic photocurrent spectroscopy

The setup for monochromatic photocurrent (PC) is shown in fig. 2.2. In monochromatic PC, the photocurrent is measured as a function of the incident photon energy. The PC spectra were collected by illuminating the device (sample) with a 100W quartz tungsten halogen lamp focused using a lens (L) where the incident beam is modulated using a mechanical chopper and dispersed through a monochromator. The photocurrent was measured using a lock-in amplifier referenced to the chopper frequency and calibrated by a Si photodetector.

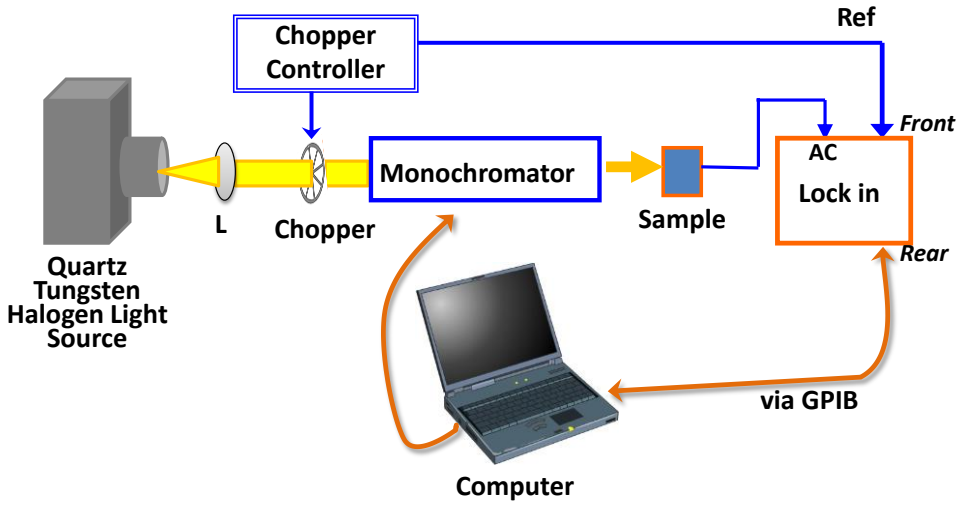

Figure 2.2 The monochromatic PC setup.

2.3.2 Fourier transform photocurrent spectroscopy

Fourier transform photocurrent spectroscopy (FTPS) has been shown to be a sensitive tool for the measurement of sub-band gap features in amorphous silicon [36] and organic

solar cell.[37-39] FTPS is a fast and a high resolution technique compared to the conventional photocurrent measurements using a monochromatic light.

The FTPS signal is measured using Fourier transform infrared spectrometer (FTIR). The most important component of the FTIR is the Michelson interferometer which is the main source of high resolution and accuracy of this technique. The Michelson interferometer is a two beam interferometer. It divides a single beam originating from the source using a beam splitter and then combines them back after introducing a path difference to generate an interference pattern. The intensity of the interference pattern can be measured with respect to the path difference created by a detector. A simplified set-up for the Michelson interferometer is shown in fig 2.3. The interferometer consists of a source (S) that generates a single beam. This beam is partially transmitted and refracted by the beamsplitter to the mirror M_1 and to mirror M_2, respectively. The mirrors M_1 and M_2 are mutually perpendicular and also perpendicular to the beam. The mirror M_1 is fixed, while mirror M_2 is movable along the beam but perpendicular to the beam. The beams are reflected off the mirrors, return to the beamsplitter, interfere, and are again partially transmitted and refracted. Thus there is a difference in the intensity of signal reaching back to the source (almost negligible) and to the detector (significant) D. Usually, the difference in the intensity reaching the detector is considered and the intensity difference as a function of the path difference yields the spectral signal in an FTIR.

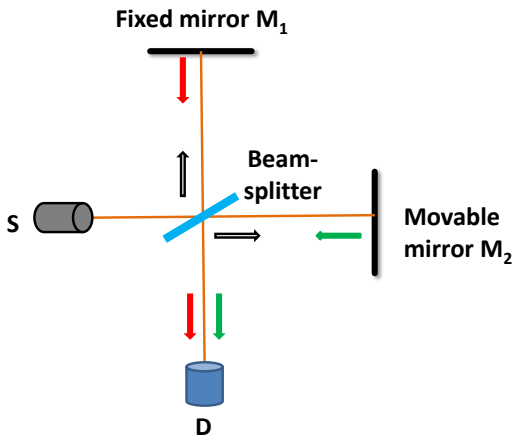

Figure 2.3 A simple Michelson interferometer setup.

To understand the process of an interferogram generation, consider an ideal monochromatic source of wavelength $\lambda_0(cm)$ with wavenumber is $\bar{\upsilon}(cm^{-1}) = \frac{1}{\lambda_0}$ and intensity $I_0(\nu_0)$. Let the beamsplitter refract and transmit exactly 50% of the intensity. The intensity at the detector when the M_2 is fixed at a certain position as a function of the path difference can be calculated as follows. The path difference between the beams travelling to M_1 and M_2 is,

$$\text{Path difference} = \delta = \left| OM_1 - OM_2 \right| , \tag{2.8}$$

When the two mirrors are at the same distance from the beam splitter, i.e, $\delta = 0$, the beams are in phase and interfere constructively at the detector. All the light reaches the detector. Now, if M_2 moves by a distance $\frac{1}{4}\lambda_0$, the path difference would be $\delta = \frac{1}{2}\lambda_0$. At

the detector, this results in destructive interference. If M2 is displaced further by $\frac{1}{4}\lambda_0$, it would again result in a constructive interference.

If M_2 is moved with a constant velocity, the signal at the detector will vary sinusoidally. The signal will be a maximum when the path difference is an integral multiple of λ_0. The intensity at the detector can be given by,

$$I(\delta) = \frac{1}{2} I(\bar{\upsilon})\{1 + \cos(2\pi \frac{\delta}{\lambda_0})\} \tag{2.9}$$

$$= \frac{1}{2} I(\bar{\upsilon})\{1 + \cos(2\pi \bar{\upsilon}\delta)\}. \tag{2.10}$$

It can be seen that $I(\delta)$ is composed of a constant (dc) component and a modulated (ac) component. The modulated component

$$I'(\delta) = \frac{1}{2} I(\bar{\upsilon})\cos(2\pi \bar{\upsilon}\delta) \tag{2.11}$$

is the interferogram. $I'(\delta)$ is the cosine Fourier transform of $I(\bar{\upsilon})$. The term $I(\bar{\upsilon})$ can be calculated using the inverse Fourier transformation.

In most of the commercial interferometers, the movable mirror moves with a constant velocity (v). It is customary to express the resultant intensity at the detector as a function of time t. The path difference between the two beams from mirror M_1 and M_2, after time t seconds is given by,

$$\delta = 2vt + \delta_0, \tag{2.12}$$

where δ_0 is the initial path difference and can be taken as zero. Using equation the intensity as a function of time can be written as

$$I'(t) = \frac{1}{2} I(\bar{\upsilon}_0) \cos(4\pi \bar{\upsilon}_0 vt) = A_0 \cos(2\pi ft), \qquad (2.13)$$

where the frequency of the interferogram is, $f = 2\bar{\upsilon}_0 v = 2\frac{v}{\lambda_0}$.

The setup of the interferometer of the ATI Mattison Infinity 60AR FTIR is shown in fig 2.4. Here the source is the lamp L_1 (tungsten halogen) for visible or NIR, and L_2 for mid-infrared source. "Q" is the quartz beam splitter for scanning the visible or NIR range. Mirrors M_1 and M_2 are not shown in the figure. M_3, M_4 and M_5 are the mirrors that deflect the beam externally. A He-Ne laser is also included in the FTIR. The monochromatic wavelength of the He-Ne laser is used as a reference to calibrate the path difference.

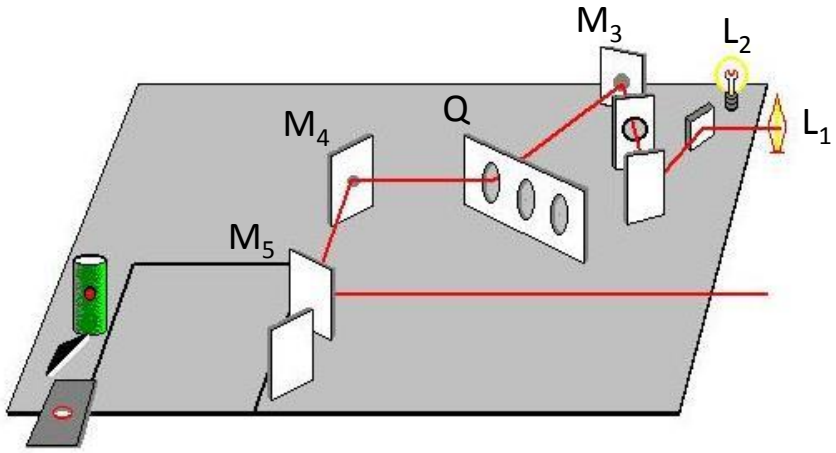

Figure 2.4 The setup of FTIR in the external mode.

The setup for FTPS is shown in the fig. 2.5. The FTIR is used in the external mode wherein the light beam from a tungsten halogen lamp inside the FTIR is focused on the device using a suitable mirror. The interferogram generated by the beam incident on the

device, is the photocurrent as function of time. An interferogram from a Si photodetector is shown in fig. 2.6(a). The Fourier transform of the signal (fig 2.6(b)) is the photocurrent as a function of the incident photon energy. The interferometer was scanned at a mirror speed of 0.16 cm/s which corresponds to modulation frequency of few kilohertz. Since the FTIR spectrometer does not allow the spectrum above and below the He-Ne laser frequency to be collected in one scan, the scans were limited to 2 eV only.

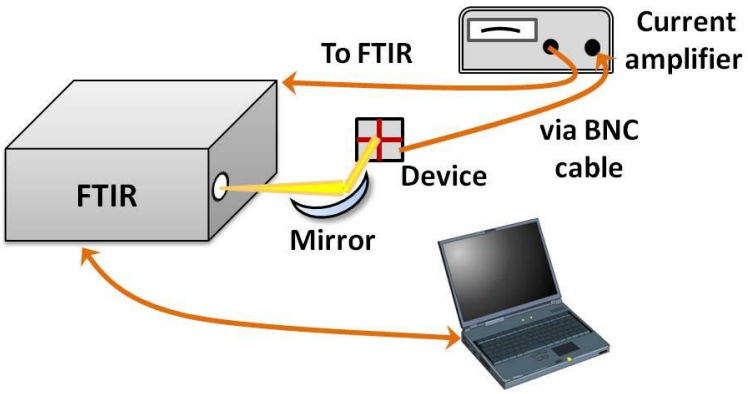

Figure 2.5 The FTPS setup.

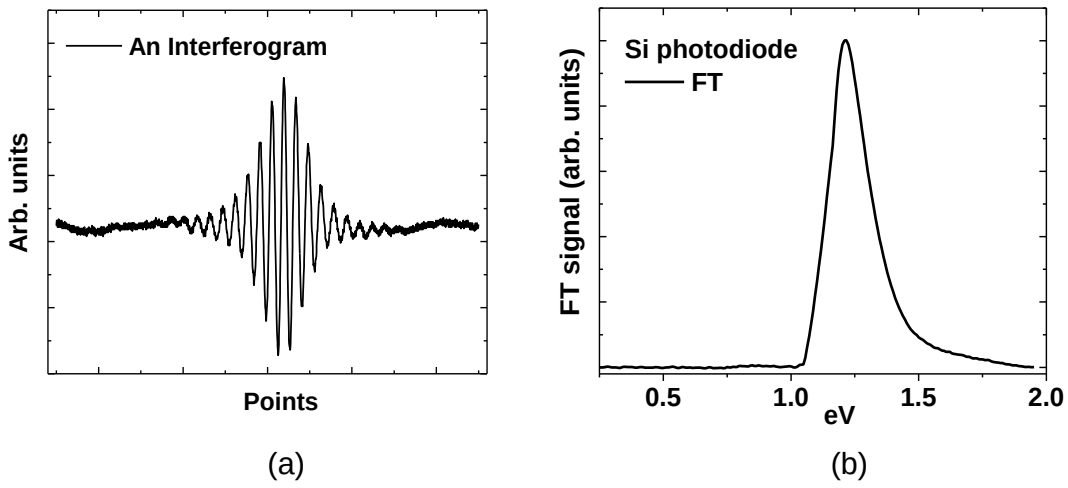

Figure 2.6(a) An interferogram from a Si photodiode (b) The Fourier transformed signal of the interferogram.

2.4 Organic Photovoltaics

Over the past two decades, extensive research has focused on optimizing the performance of organic bulk heterojunction (BHJ) solar cells. In the past few years, the efficiencies of OPVs have reached over 10%.[40] Several factors such as the bulk transport properties, morphology, band gap, band offsets and intermediate states such as CT states play a significant role in deciding the efficiency of a BHJ device. The organic PV process constitutes (i) absorption of photons, (ii) conversion of solar photons into excitons (singlet excitons), (iii) exciton diffusion, (iv) formation of intermediate states, and (v) dissociation of exciton into free charge carriers.[40,41] Most BHJs use a polymer-fullerene blend as an active layer where the absorption mainly takes place either within the donor polymer or the acceptor. The conversion of solar photons into excitons is usually an ultrafast process. The process (iii)-(v) depend strongly on the constituent materials, the fabrication techniques as well as the morphology of the thin film. The active layer films are often annealed to improve the morphology of the active layer. The annealing results in a phase segregation between the donor and the acceptor within the bulk, which may vary from few hundred nm to few micrometers.[42] The formation of nanoscale morphology due to phase segregation leads to an efficient charge generation at interface.[43] Finally, an interpenetrating network is formed within the bulk. Since the diffusion length of singlet excitons is close to few nanometers, the network is known to enhance the diffusivity of the charges within the device.[44] It is very well established that the presence of a fullerene helps in an efficient and an ultrafast CT from the donor to the fullerene, which is an acceptor. The CT may result in the formation of intermediate

electronic states at the interface called the charge transfer complex or the CT states. The CT states may dissociate into free charges. Since the goal of the work presented here is to elucidate role of the CT excitonic states, BHJ solar cells were fabricated. To quantify the results on the basis of donor polymer or copolymers only, $PC_{61}BM$ has been used as an acceptor in all the devices.

A BHJ solar cell is most commonly characterized by its power conversion efficiency (PCE). The PCE is calculated from the current-voltage (J-V) characteristic of the device and Eq. 2.14. The J-V curve of P3HT:PCBM (1:1) device is shown in fig. 2.7. In the figure, J (current density) is calculated by normalizing the current with the device area. For Ossila ITOs, the device area is $0.046 cm^2$.

$$\eta = FF \frac{I_{SC}.V_{OC}}{P_{IN}}, \tag{2.14}$$

where I_{SC} is the short circuit voltage, V_{OC} is the open circuit voltage and P_{IN} is the input power from AM 1.5 source and FF is the fill factor given by,

$$FF = \frac{I_{MAX}V_{MAX}}{V_{OC}I_{MAX}}. \tag{2.15}$$

In Eq. 2.15, I_{MAX} and V_{MAX} is the current density and voltage at maximum power output. For the J-V characteristics shown in fig. 2.7, the fill factor and efficiency (η) is 0.68 and 1.7%, respectively.

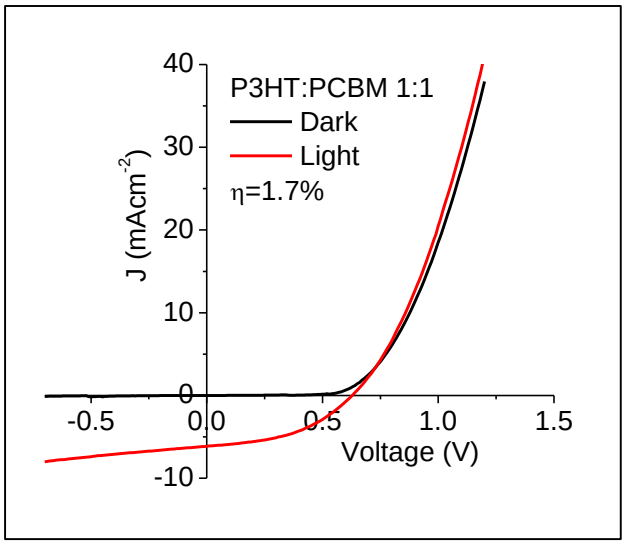

Figure 2.7 The J-V characteristics of a P3HT:PCBM (1:1) device.

Another way to evaluate the device performance is by measuring the external quantum efficiency (EQE) or responsivity as function of incident photon energy. The responsivity is calculated using,

$$R(\lambda) = \frac{I_{Device}(\lambda)}{I_{Si}(\lambda)} R_{Si}(\lambda). \tag{2.16}$$

$I_{Device}(\lambda)$ and $I_{Si}(\lambda)$ are the spectral photocurrent of device and calibrated silicon photodiode respectively. $R_{Si}(\lambda)$ is the calibrated responsivity of the Si photodiode. The EQE can then be calculated by,

$$EQE(\lambda) = R(\lambda)E(\lambda), \tag{2.17}$$

where $E(\lambda)$ is the incident photon energy.

2.5 Sample Preparation and Device Fabrication

2.5.1 Sample preparation for PIA studies

We have used PIA to probe the triplet states in PhLPPP. The goal of this experiment was to measure the triplet diffusion length. In Chapter 6 we illustrate our method by the quenching of T-T absorption in two different PhLPPP polymer samples,[7] a high molecular weight (M_n=14,700 g/m) (PhLPPP-H) with polydispersity of 1.3 and a low molecular weight (M_n=3800 g/m) (PhLPPP-L) with polydispersity of 1.6, by an electron acceptor, PCBM, which was purchased from Sigma-Aldrich Co. The main advantage of using PhLPPP is that the experiments could be performed at room temperature (RT) since a trace amount of Pd in the PhLPPP backbone results in a high fraction of triplet excitons at RT.[45] PhLPPP:PCBM blends were prepared in various molecular ratios, from 50:1 to 10000:1 by dissolving the components in dichlorobenzene. Equal volumes of various blends were carefully drop cast onto glass substrates so that the final dried sample areas are same for all blends as determined by visual inspection. No phase separation in the mixture was observed for low concentrations of PCBM as verified by an atomic force microscope.

2.5.2 Device fabrication

A BHJ solar cell and a schematic are shown in fig. 2.8(a) and fig. 2.8(b), respectively. For preparation of the solar cell, an indium tin oxide (ITO) coated glass substrate was first cleaned with soap solution and rinsed in deionized water. The cleaned substrates were submerged in diluted aqua regia for 10-15 mins, rinsed in deionized water and then

ultra-sonicated in acetone and isopropyl alcohol. For devices prepared using the Ossila ITO, the ITOs were first ultra-sonicated in warm water for 5 mins in 10% NaOH solution (deionized water). The substrates were then ultra-sonicated in deionized water for another 5-10 mins. Later, the substrates were ultra-sonicated in organic solvents. A filtered (polyvinyl difluoride 0.45µm) layer of poly (3,4-ethylene dioxy-2, 4-thiophene) poly sulphonate (PEDOT:PSS) is spin coated on ITO at 5000 rpm and baked at $100°C$ for 25-30 min. For the active layer, separate donor and acceptor solutions were prepared, individually filtered and then blended in desired ratio. The polymer blend layer is then spin coated at 700 rpm and baked at 100^0C for 5 min after which the device is encapsulated. In order to obtain a better crystalline film, they may also be solvent annealed immediately after spin coating. All the solar cell fabrication steps were carried out in a N_2 glove-box.

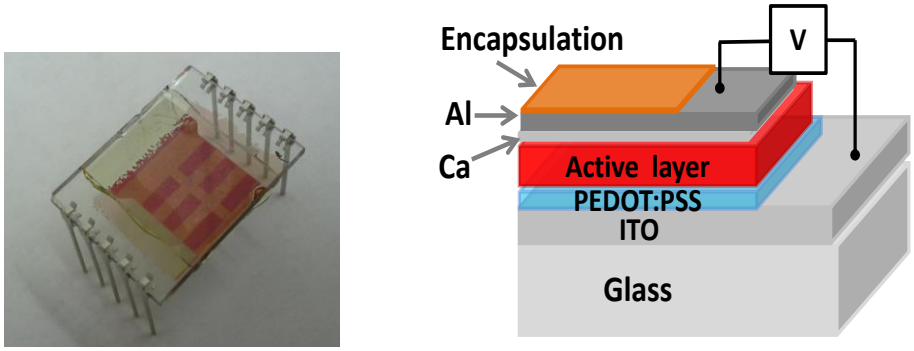

(a) (b)

Figure 2.8 (a) A P3HT: PCBM solar cell device fabricated using Ossila components (ITO and connecting legs). (b) The structure of a BHJ device.

3.

CHARGE TRANSFER EXCITONIC STATES IN POLYTHIOPHENE BASED SOLAR CELL

Poly(3-hexylthiophene) (P3HT) is one of the most extensively analyzed homopolymer.[46] Thanks to its easy availability and ability to form a suitable morphology, the efficiency of the solar cell can reach up to 5%.[46] Its combination with fullerene offers researchers, a platform to probe various excitonic states in a BHJ-type system. In this chapter, we introduce the concept of CT states in the polymer:fullerene bulk systems and discuss their relevance to device function. We probe the CT excitonic states using PC spectroscopy in P3HT:PCBM devices fabricated in our lab. These studies also provide a preliminary basis of cross checking the validation of our experimental set-ups and its results.

3.1 Introduction

In a BHJ solar cell the active layer comprises of two or more blended materials. The photoexcitation process of the blend in a BHJ solar cell, results in generation of singlet as well as other excitonic states, diffusion and finally charge separation. Recent reports indicate that the process of photoinduced charge separation in polymer BHJs involve charge transfer complex (CTC) states or intermolecular CT (inter CT) that are formed at the interface of the polymer and fullerene phases in the blend.

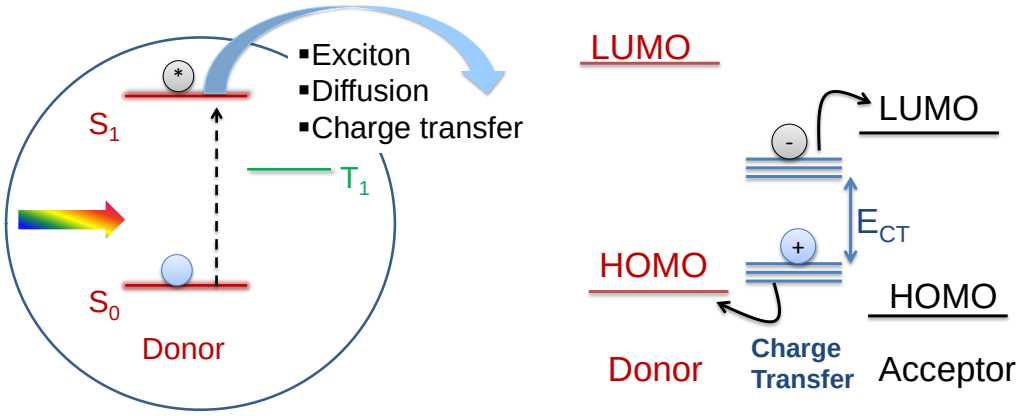

(a) (b)

Figure 3.1 (a) Schematics of the donor excitation. The ground-state (S_0), first singlet (S_1) and first triplet state (T_1) are shown. (b) The HOMO and LUMO levels of the donor is denoted by HOMO(D) and LUMO(D), respectively. The HOMO and LUMO levels of the acceptor is denoted by HOMO(A) and LUMO(A), respectively. The energy of the inter-CT state is denoted by E_{CT} [Ref. 47].

To visualize the concept of the inter-CT state, consider a combination of two organic polymers; one donor and the other acceptor.[47] In molecular picture, the electron-hole pair is considered as a single particle and the relevant energy levels are depicted in fig. 3.1(a). Excitation of the donor results in a transition from the S_0 to S_1 the of the donor. This singlet exciton then diffuses to the donor-acceptor interface and may dissociate if the conditions are favorable. The same picture can also be visualized by considering the HOMO-LUMO levels of the donor and the acceptor. In this picture the excitation of donor results in electron transfer from HOMO of donor (HOMO(D)) to LUMO of donor (LUMO(D)). The electron in LUMO(D) can be transferred to LUMO of the acceptor

(LUMO(A)). The separated, yet weakly bound electron-hole pair is the CT exciton. The CT states are electronic states (with energy E_{CT}) formed at the donor-acceptor interface as shown in fig. 3.1 (b). If there are other energy levels present, such as a triplet energy level (T_1) with energy E_T lower than the E_{CT}, it is possible for the CT state to recombine as a triplet state. The unstable CT state may also recombine to a lower energy state by photon emission which is one of the major loss mechanisms in BHJ.[47] Throughout this thesis, inter CT and CTC states are used with similar meaning.

The CTC states are energetically deep inside the optical gap of the polymer and fullerene constituents.[48] Drori and coworkers have recently shown the existence of below-gap (midgap) CTC states by photomodulation techniques.[49] Subsequently, they have shown that interfacial polarons generated with below-gap excitation do not effectively contribute to the photocurrent density for typical thicknesses of polymer films used in current BHJ architecture.[50] Since the CTC states play a pivotal role in generation of free charge carriers and photocurrent density, understanding the origin of CTC states is vital for improving device performance.

The energy of the CTC state is given by

$$E_{CT} = \text{LUMO(A)-HOMO(D)-}P_{eh}(r)\text{-C(r)}, \tag{3.1}$$

where $P_{eh}(r)$ is the polarization energy and C(r) is the Coulomb energy.[51] The C(r) is given by,

$$C(r) = \frac{e^2}{4\pi\varepsilon_0 r_{CT}}, \tag{3.2}$$

where e is the electron charge, ε is the dielectric constant of the blend and r_{CT} is the separation between the positive and negative charge in the CTC state. The $P_{eh}(r)$ results from separation of charges. For organic crystals, $P_{eh}(r)$ is estimated to vary from 0.2-0.4eV due to charge transfer between the same chromophore.[51] Theoretical calculations for a single crystal DPP show that the polarization energy varies from -0.65 eV to 0.14 eV, depending on the nature of the chromophore and the orientation of the chromophore.[52] Thus, the $P_{eh}(r)$ is specific to the chromophore and varies over a large range. The C(r) term is the result of the attraction between the spatially separated positive and negative charges of the CTC state. In general, the r_{CT} for a CTC state may be close to few nm; then, C(r) varies from 0.1-0.5eV. If some theoretical or experimental estimates of $P_{eh}(r)$ and C(r) for the polymer:fullerene system were available, then E_{CT} can be calculated using Eq. (3.2). The HOMO/LUMO energy levels of the polymers are typically known from cyclic voltammetry measurements. In the following sections, we elaborate on identifying the inter CT states using two PC techniques; monochromatic PC and FTPS, in the P3HT based devices.

3.2 Photocurrent Spectroscopy- Probing Intermolecular Charge-Transfer States

The normalized absorption spectrum of a spin coated thin film of pristine P3HT is shown in the fig. 3.2(a) (black). In its solid state form, the lowest absorption feature at approximately 2 eV is attributed to the interchain interaction between P3HT chromophore.[53] In general, both the intra and the interchain interactions are involved in the absorption feature of P3HT. From fig. 3.2(a), it is seen that the absorption onset is

approximately at 1.9 eV (optical bandgap of P3HT).[54] We note that the HOMO and LUMO level of P3HT is -5.08 eV and -3.17 eV, respectively.[55] The difference between the HOMO and the LUMO level gives the electronic bandgap, which is greater than the optical bandgap. The normalized absorption of P3HT:PCBM (1:1) (blue) is shown in fig, 3.2(a) along with P3HT:PCBM (1:2) (green). Notice that inclusion of the fullerene does not significantly shift the onset of the absorption. Shrotriya et al. have observed significant changes in the overall features in P3HT-PCBM blends at higher concentration (>65%) of PCBM.[56] They also observed that the addition of PCBM decreases the absorption in the 2 - 3 eV region. The spectral changes in the blended samples are the result of lowering of the inter-chain interaction between the neighboring P3HT chromophores. By replacing PCBM with C_{60}, Shrotriya et al. observed a significant difference between the absorption in P3HT:PCBM (1:1) and P3HT:C_{60} (1:1) films. Since P3HT is oxidized by PCBM and C_{60}, the difference in absorption indicates that the transfer of charges between P3HT-PCBM is different than in P3HT-C_{60}.

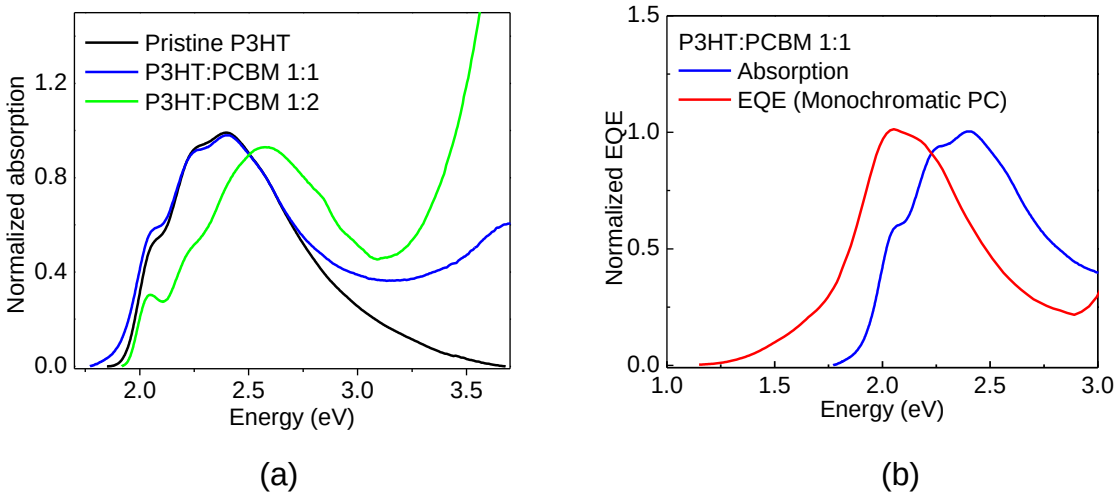

Figure 3.2 (a) Normalized absorption of pristine P3HT, P3HT:PCBM (1:1) and P3HT:PCBM (1:2) spin coated films. (b) Normalized EQE using monochromatic PC (red) and the absorption spectrum (blue) from a P3HT:PCBM (1:1) photovoltaic device.

The normalized absorption in P3HT:PCBM (1:1) sample and the responsivity (1:1 device) measured using monochromatic PC is shown in fig. 3.2(b). The responsivity is measured by first normalizing the measured PC with the device area, which gives current density. Next, we need to divide the current density with the lamp profile. To obtain the lamp profile, the current density is measured using a Si detector (preferably ON) and then normalized by the responsivity of Si. Since the current density from the device (say P3HT:PCBM) and lamp profile depend on the experimental setup, the division results in nullifying the effect of setup.

The FTPS spectra of P3HT:PCBM (1:1) device is plotted as the normalized EQE and is shown in fig. 3.3. To calculate the normalized EQE, the Fourier transform (FT) signal from the P3HT:PCBM device is first normalized by the area of the device. The FT signal

is the required PC, but with arbitrary units. The FTPS PC has been normalized with the lamp profile obtained from the monochromatic PC set up. Ideally, one would normalize the FTPS PC by the lamp profile of the tungsten lamp in the FTIR. Note that the PC from the Si detector is a narrow signal and is centered at ~1.1 eV (bandgap of Si). This suggests that the FTPS method detects the onset of any state with a finite width. Hence, FTPS PC of Si photodiode should not be used to calibrate the FTPS PC of other samples. To overcome the difficulty of calibration, we use the lamp profile of monochromatic PC set up. Also note that both PC methods utilize tungsten halogen as source, so the lamp profile is expected to be identical except for the difference in the exact intensity of the lamp profile. The responsivity calculated by the FTPS PC will have arbitrary units but correct spectral features, especially the onset of the CT state. The responsivity curve is normalized and represented as the normalized EQE. The FTPS and the monochromatic PC spectra are identical and both the PC methods show a feature lower than the onset of absorption in the blend. The low energy onset is the signature of a weak sub bandgap inter CT band, as observed in other polymer BHJ solar cells.[37,38] Vandewal et al.., in a recent work show that a functional fit given by Eq. (3.3) to the FTPS EQE using Marcus's theory, yields accurate values of the E_{CT}.[57] Using a similar approach, we fit the FTPS and PC spectra by

$$R(E) = a + \frac{b}{E}\exp\left(-\frac{(E_{CT} + \lambda - E)^2}{4\lambda kT}\right), \tag{3.3}$$

where a and b are fitting constants, E_{CT} is the onset of the charge transfer state, λ is the reorganization energy whose value was fixed at 0.25eV, E is the incident photon energy, k_B is the Boltzmann constant, and T is the temperature. Since the inter CT states observed

from the EQE spectra extend below the absorption edge, the fit was applied from low energies to 1.6 eV, depending on the best fit parameters. The E_{CT} from the monochromatic PC is 1.21 eV and 1.24 eV from the FTPS measurement. The E_{CT} values in our P3HT:PCBM device corroborates with other works using (1:1) weight ratio of P3HT and PCBM solar cells.

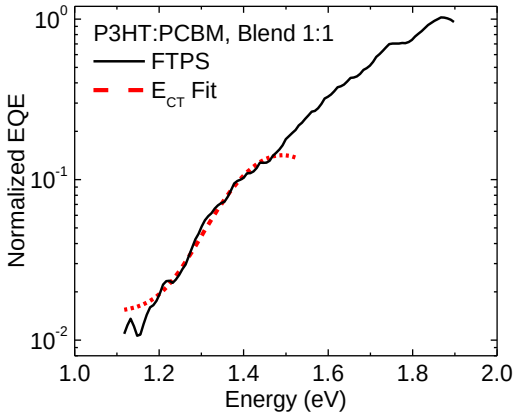

Figure 3.3 Marcus fit (dashed) to the normalized FTPS photocurrent (solid line) in P3HT:PCBM.

From fig. 3.2(a), the onsets of absorption in pristine P3HT and P3HT:PCBM (1:1) are not significant different indicating that the ground state charge transfer has a very weak oscillator strength. On the other hand, the onset of CT emission is known to shift as a function of the acceptor due to the changes in the average dielectric constant.[58] The shift in the onset of the emission indicates the involvement of CT excitons in the emission. To confirm the CT nature of the low energy feature in our PC measurements in the P3HT:PCBM devices, the monochromatic PC was measured in a P3HT:PCBM (1:2) sample. Figure 3.4 shows the normalized absorption from a P3HT:PCBM 1:1 sample

(blue), and the normalized EQE by monochromatic PC from P3HT:PCBM 1:1 (red) and 1:2 (green) devices. Even though the steady state absorption onsets (fig. 3.2(a)) don't shift significantly, the PC onset for the 1:2 sample shifts considerable. Thus, the addition of PCBM shifts the onset of PC, which proves the "polar" nature of the inter CT excitons. Note that the 1:1 blend shows the lowest onset of PC. In general for P3HT based devices, the blend formed close to 50% of each polymer is found to give a better overall PCE.

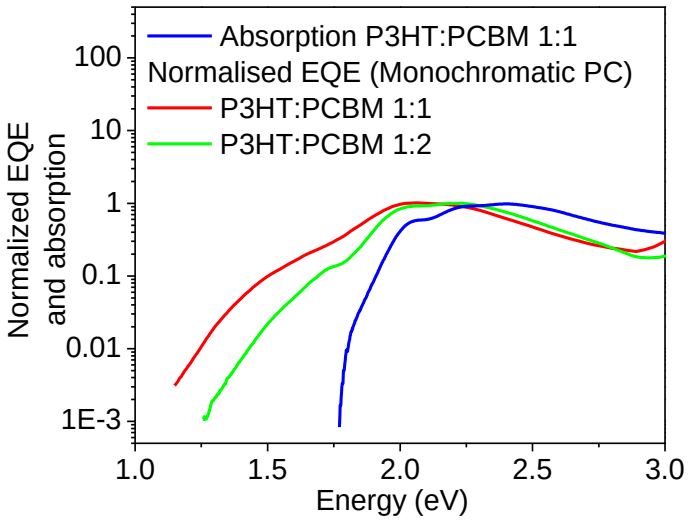

Figure 3.4 Normalized EQE of pristine P3HT, P3HT:PCBM (1:1) and P3HT:PCBM (1:2) by monochromatic PC .

Although the recent studies show clear evidence of CT states governing the voltage dependent and independent photocurrent [30,59] as well as the open circuit voltage (Voc),[39] the exact role of inter CT states in controlling PCE is still debated.[60] Lee et al. have shown that the low energy stabilized CT state may not contribute significantly to the photocurrent.[61]

A large discrepancy is observed between the experimental lifetimes (~100 ns)[62,63] and theoretical predictions of CT lifetimes (~μs to ms).[30,64,65] A recent study by Bakulin et al.. shows that the driving energy for the charge separation in organic PVs occurs through the formation of excited, delocalized band states, which are typically extremely short lived (< 1ps).[66] Apart from the estimation of the lifetime of CT states, emphasis has also been placed on the dissociation efficiency of the CT states. Yamamoto et al. have shown almost instantaneous formation of CT states from the singlet states, and have calculated the dissociation efficiency as 70%.[67,68] We revisit the issue of the CT states in other polymer:fullerene systems in the next chapter.

3.3 Temperature Dependence of Photocurrent

In a blended sample, excitation of the donor polymer results in the formation of singlet exciton. After diffusing to the donor-acceptor interface, the exciton can transfer its negative charge to the acceptor, leaving positive charge behind on the donor polymer. The separated, yet, weakly-bound positive-negative charge pair may recombine again or simply dissociate. Since the weakly-bound positive-negative charge pair can be one of the source of free charges, it is worthwhile to understand the dynamics of a weakly-bound charge pairs. In the literature, temperature dependent studies have been performed to distinguish between the localized and the delocalized nature of charges.[69-71]

Other studies in the literature have probed the dynamics of the singlet and CT states. Using transient and temperature dependent photoluminescence (PL) studies on PCPDTBT and its blend Jarzab et al. have separated the dynamics of singlet and CT

exciton.[72] Even though the peak intensity of the steady state CT exciton emission changed over the range of temperature (5 K- 294 K), the lifetime of the CT exciton state probed did not change with temperature and bias. The localized nature of the state suggested that this state does not contribute to the diffusion.

The population dynamics can also be probed using PC yield, I_{yeild}. The resultant PC yield I_{yeild} has often been expressed as a product of charge generation *n* and summation of the mobility μ,

$$I_{yeild} \propto n\sum \mu, \tag{3.4}$$

Hence, understanding the population requires separate understanding of the change of (i) mobility and (ii) initial carrier generation, as function of temperature (T).

Transient photoconductivity studies on poly (phenylenevinylene) (PPV) by Lee et al. have shown *n* to be temperature independent. On the other hand steady state photoconductivity studies have shown strong T dependence of PC yield. This apparent conflict was resolved by Moses et al. by taking the thickness of the film as an important factor.[70] In the steady state PC technique, the peak PC ($I_{ph,peak}$) is characterized by Arrhenius-type temperature- dependence. The $I_{ph,peak}$ is related to the temperature *T*, and the activation energy E_a by

$$I_{ph,peak} \propto \exp\left(\frac{-E_a}{kT}\right). \tag{3.5}$$

The activation energy can be estimated by an exponential fit to the plot of peak PC as a function of temperature. For thicker samples (>4000 nm) of MEH-PPV, the steady state PC was found to be strongly temperature dependent on *T*. For thin sample, the activation

energy for hopping (E_a) was around 30meV. The small E_a implied that for thin films, the PC yield has a weak dependence on temperature in agreement with the previous results from transient photoconductivity measurements. Since the thickness encountered in BHJ is < 120 nm, for BHJ too, one can expect the current yield to be weakly dependent on temperature.

The steady state temperature dependent PC studies on PCPDTBT:PCBM have also shown changes in the intensity of short circuit current with temperature.[54] Similarly, PC studies on MDMO-PPV:PCBM have also shown temperature dependent behavior.[71] In both the cases, the intensity of the PC increases with the temperature and the positive coefficient has been assigned to increase of mobility and increased thermal activation. The temperature dependence has also been associated with the presence of trap states for recombination of CT exciton.[54,72] Such trap states are considered as major loss mechanism affecting the overall photo-conversion efficiency of a solar cell. In cases of a weak temperature dependence of PC, it indicates absence of trap states.

We performed preliminary temperature dependent studies on PC from P3HT:PCBM 1:1 devices to understand the dynamics of charge carriers in the solar cell. The normalized absorption and the temperature dependent monochromatic PC of P3HT:PCBM (1:1) sample is shown in fig. 3.5(a). The spectral PC has been measured from 50 K-360 K, but for clarity all the spectra are not shown. The PC shown has been measured in the visible region only. The plots of monochromatic PC show an increase in the overall PC with increasing temperature. The spectral PC in fig. 3.5(a) can be analyzed in three region (i) intensity in ~2 eV (ii) intensity in the infrared region ~1.5 eV or 1.2 eV

and (iii) the onset in 1.2 eV region. In order to check for any changes in the onset (point (iii)) of the PC in the region, the normalized PC (UV-Vis and NIR region) at the two extreme temperatures; 50 K and 360 K, is shown in fig 3.5(b). The normalized PC's at the two temperatures completely overlap. In contrast, Harrison et al. had observed a redshift (and a sharper vibronics) in the singlet absorption in MEH-PPV samples. The redshift was attributed to increase in the rigidity, less twisting of chains, a higher conjugation length and lowering of the optical bandgap.[73] From the onset of PC in the P3HT:PCBM samples, it seems that bandgap of the CT state is not affected by the temperature.

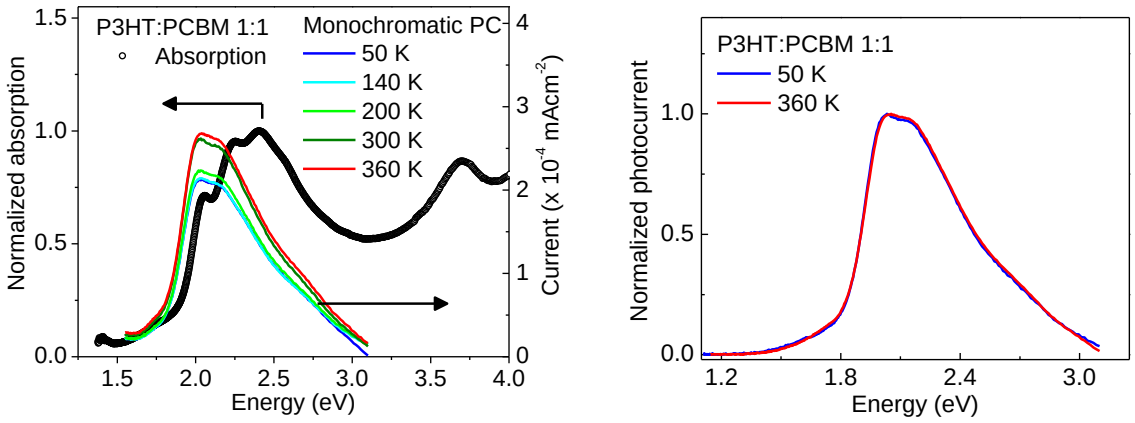

Figure 3.5(a) Normalized absorption and monochromatic PC as a function of temperature in the UV-Vis region. (b) Normalized PC at the two extreme temperature data points.

Next, consider the intensity of the peak PC at ~2 eV (fig. 3.5(a)). The peak PC increases with increasing temperature. The peak PC as a function of temperature is

plotted in fig. 3.6(a). A strong dependence of PC on temperature is observed in the 220K-360K region, while an almost constant value of peak PC is observed in 50 K-140 K (all points not shown). Since the change in PC is observed in the high temperature regime (220 K- 360 K), the activation energy can be estimated by a fitting Eq. 3.5 to the high temperature regime. From the exponential fit to the peak PC (red) in fig. 3.6(b), the activation energy is calculated to be approximately 40 meV. This value is consistent with the range of activation energy in organic material.[69,71,74,75] The small activation energy corresponds to an almost temperature-independent spectral PC in P3HT:PCBM devices and agrees well with the temperature independence of short circuit current observed (T>300 K) in Ref. 71. Note however that the activation energy and the temperature mentioned here are calculated from the peak PC: a position which corresponds to the absorption in P3HT. In this case, it cannot be considered as activation energy of CT states.

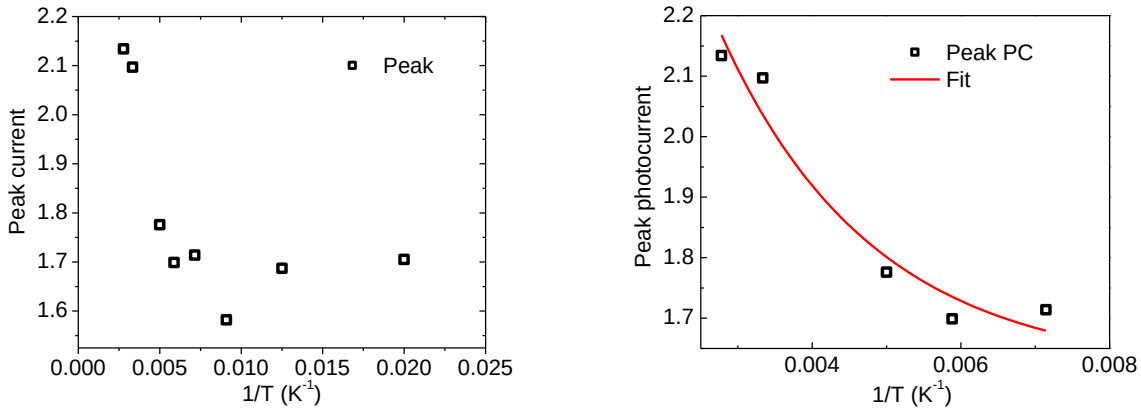

Figure 3.6(a) The peak photocurrent as a function of inverse of temperature. (b) The exponential fit (red) to the peak photocurrent vs inverse of temperature curve.

To evaluate the effect of temperature on the CT states, one should consider the PC in the CT state region only, i.e. the intensity of PC in the infrared region ~1.5 eV or 1.2 eV. [76] From fig. 3.5(a), it seems that the PC intensity in CT state region is far less affected by the temperature. It is possible that the diffusion of the CT state may not be thermally activat and hence the CT state detected may not be delocalized. For a further clarification, one may have biased dependent studies of the P3HT:PCBM blend. Another option is to utilize pristine donor-acceptor polymers for temperature/bias dependent studies as they have an "inbuilt" intramolecular CT state. The preliminary data of temperature dependent PC in donor-acceptor copolymers is presented in Chapter 7 under "Future Work".

4.

DIKETOPYRROLE-BASED COPOLYMERS AND STATISTICAL COPOLYMERS

In an effort to understand the role of inter CT states, a set of low bandgap diketopyrrolopyrrole (DPP)-based copolymers were chosen. The optical bandgap ranges from 1.4 eV to 1.7 eV and is tabulated in Table 4.1. The HOMO-LUMO level of the DPP-based copolymers is also shown in fig. 4.1. Note that the electronic bandgap is more than optical bandgap for each polymer. The DPP-based copolymers are further separated into copolymers and statistical copolymers. The copolymers involved in the present studies were two phenyl-based DPP copolymer; PDPP-BBT (sample1) and PDPP-BBT (sample2), and a thiophene based DPP copolymer (TDPP-BBT). The PDPP-BBT (sample2) is similar to PDPP-BBT (sample1) except for a slightly different side chain conformation. In comparing the two DPP materials, our discussion will mainly relate to PDPP-BBT (sample1) and TDPP-BBT (fig. 1.2(d) and (e)). The two statistical copolymers (Poly A and Poly B) are thiophene based, but vary in their DPP fraction. Poly A has lower DPP fraction compared to Poly B (fig. 1.2(f)).

Table 4.1 The optical bandgap of various DPP-based copolymers.

	Sample	Optical bandgap (eV)
DPP- based copolymers	PDPP-BBT (sample1)	1.73
	PDPP-BBT (sample2)	1.5
	TDPP-BBT (sample1)	1.43
DPP-based statistical copolymers	Poly A (lower DPP fraction)	1.6
	Poly B (higher DPP fraction)	1.5

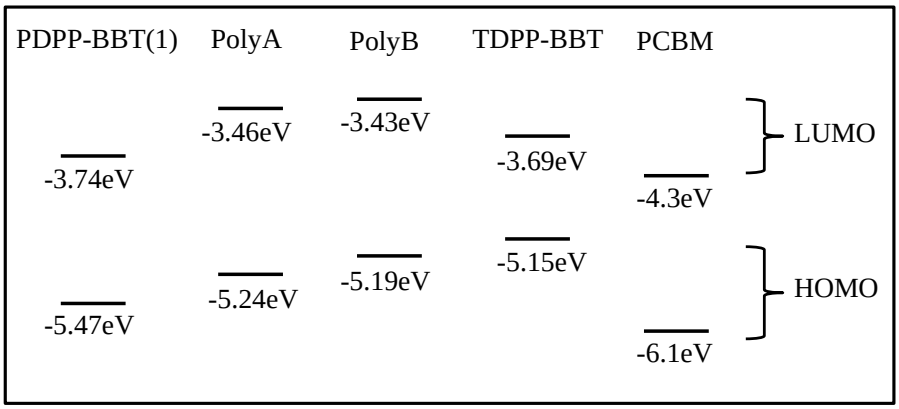

Figure 4.1 The HOMO/LUMO values of the DPP-based copolymers (PDPP-BBT and TDPP-BBT), DPP- based statistical copolymers (Poly A and Poly B) and PCBM, utilized in the present work.

4.1 Absorption

The normalized absorption spectra of the DPP based copolymers are shown in fig. 4.2(a). The absorption in TDPP-BBT is redshifted with respect to the PDPP-BBT samples indicating a smaller optical bandgap for TDPP-BBT compared to PDPP-BBT (sample1). The DPP copolymers show two peaks in the absorption spectrum: a higher energy peak in the 3 eV - 4 eV which corresponds to the π-π^* transition and the lower

energy peak (1.5 eV-2.5 eV) which has been attributed to an intramolecular CT (intra CT) state from the thiophene or phenyl donor to the core acceptor units. It is well established that the low energy absorption band in a donor-acceptor copolymer is the intra CT state.[77] The intra CT state is a state where the negative and the positive charges (such as the electrons and holes) are separated but located on the same donor polymer chain. The formation of intra CT states stabilizes the donor-acceptor complexes covalently bound along the polymer backbone.

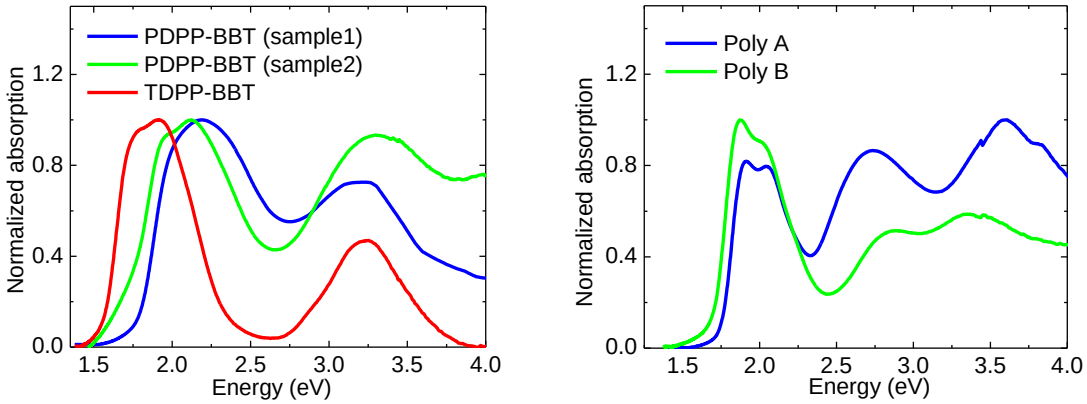

(a) (b)

Figure 4.2 Normalized absorption spectra of (a) DPP based copolymers (b) DPP based statistical copolymers.

The normalized absorption from spin coated thin films of the statistical copolymers: Poly A and Poly B, is shown in fig. 4.2(b). The region 1.5 eV- 2.5 eV corresponds to the intra CT state and the region 2.5 eV – 4.0 eV corresponds to the π-π* transition. The absorption in Poly B (higher DPP fraction) is slightly redshifted than the Poly A (lower

DPP fraction) indicating a lower optical bandgap in Poly B. A slightly lower optical bandgap of Poly B can be attributed to the narrow polydispersity, despite its lower molecular weight.[78] Also, note that in Poly B, the intensity of the intra CT state absorption is more than the absorption in the π-π* transition region.

It is very well known that the presence of an external acceptor results in charge transfer from the donor polymer to the acceptor, usually PCBM.[79] An already separated state such as an intra CT may have a direct impact on the charge transfer. Hence, it is worthwhile to probe the intramolecular states is the copolymers. Here we present the studies performed on the intra CT state on a set of thiophene based DPP copolymer; TDPP-BBT, Poly A and Poly B. We also estimate the binding energy (*BE*) of the intra CT state.

4.2 Electric Field Dependence - Probing Intramolecular Charge-Transfer States

The electric field dependence of the optical absorption was observed by Haarer et al. in anthracene-PMDA crystals.[80] The external electric field splits the CT state formed between the donor-acceptor crystal by about 10 cm^{-1}. Here, the CT refers to electronic states formed between two different monomers/polymers, which do not belong to the same crystal/chain. The CT state observed in the donor-acceptor crystal is the inter CT state, wherein the negative charge has been transferred to the acceptor while the positive charge stays on the donor. Such splitting may be difficult to observe in amorphous organic polymer semiconductors due to their broad absorption spectra. Nevertheless, it is possible to track the variation in the absorption as a function of the electric field by

application of an external bias. Various articles in the literature have shown that the bias dependent absorption spectrum may result in an exciton confinement at the interface. The variation in the absorption has been observed in inorganic semiconductor based quantum well and has been assigned due to quantum confined Stark effect.[81] A similar exciton confinement was also observed by tracking the changes in the peak position of absorption in multiple quantum well (MQW) structures of alternate layers of PTCDA (3,4,9,10 perylenetetracarboxylic dianhydride) and NTCDSA (3,4,7,8 naphthalenetetracarboxylic dianhydride) organic crystals.[82] The PTCDA/NTCDSA interface forms a type I heterojunction. As the layer thickness is reduced the PTCDA forms a two dimensional potential well confined between NTCDSA on either side. In the MQW structures the optical absorption was found to shift as the layer thickness was changed. The shifts were attributed to the changes in the exciton binding energy due to exciton confinement in the PTCDA crystal.

McGinnis et al. have probed porous Si using steady state absorption.[83] When the field was applied perpendicular to the growth direction, the absorption spectrum redshifted and broadened. The absorption coefficient was also found to increase with the bias. The application of bias in the direction perpendicular to the porous Si growth also showed changes in photoluminescence intensity. The observed results were explained on the basis of confinement of exciton within the nanostructured Si. In our case, the band offset at the copolymer-copolymer interface and copolymer-fullerene interface could confine the intra CT exciton. Since OPVs are essentially type II heterojunction, the DPP

copolymers provide a nice platform for observing changes to the absorption edge (of the intra CT peak), similar to quantum wells.

We extend the bias dependent study to estimate the binding energy of the intra CT exciton from changes in the absorption spectrum as a function of the electric field. In order to estimate the BE, if one assume that the potential energy to separate the bound charge-transfer pair is same as the coulomb energy, the binding energy (BE) is given by [84]

$$eE_{\max} r_{GP} = \frac{e^2}{4\pi\varepsilon\varepsilon_0 r_{GP}} = BE\,, \tag{4.1}$$

where, E_{max} is the saturation field given by

$$E_{\max} \approx \frac{|V_{\max}|}{L}, \tag{4.2}$$

$|V_{\max}|$ is the saturation potential, L is the film thickness, r_{GP} (Eq. 4.1) is the separation between point like charges in the geminate pair, ε_0 is the permittivity of free space, e is the electron charge, and ε is the dielectric of the medium which is ~ 3.5 for most conjugated polymers. The r_{GP} may be simplified in Eq. 4.1 as,

$$r_{GP} = \left(\frac{e^2}{4\pi\varepsilon\varepsilon_0 eE_{\max}}\right)^{1/2}, \tag{4.3}$$

The BE can be calculated by using the value of rGP and Emax in Eq. 4.1. For all the following electric field dependent studies, a BHJ device was fabricated using the method discussed in the section 2.5.2. The absorption was measured through the ITO/PEDOT:PSS/ Polymer/Ca/Al with ITO/PEDOT:PSS/Ca/Al as a reference.

4.2.1 Thiophene based DPP copolymer

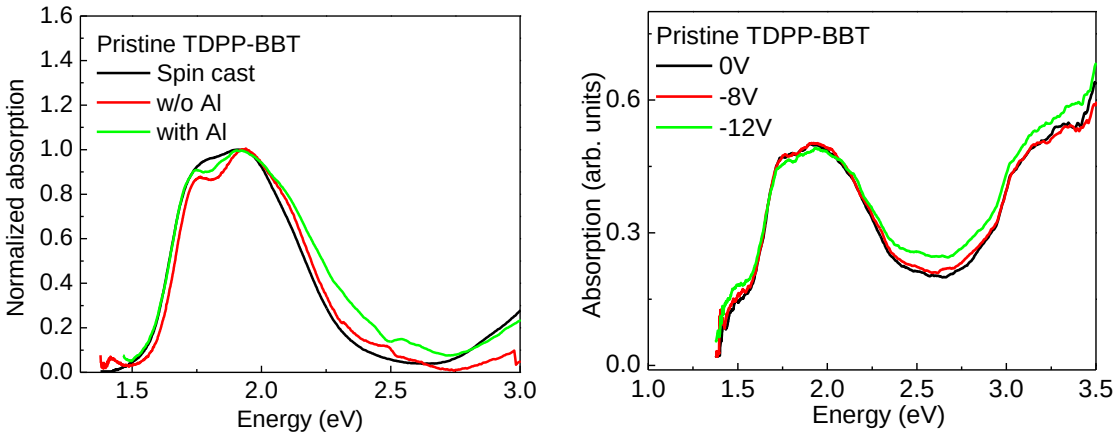

(a) (b)

Figure 4.3(a) The absorption of the pristine TDPP-BBT from a spin-cast film (black), from a device region ITO/PEDOT:PSS/TDPP-BBT/glass without Al (red) and from a device region ITO/PEDOT:PSS/TDPP-BBT/Ca/Al (green). (b) The bias dependent absorption in a pristine TDPP-BBT device in the region ITO/PEDOT:PSS/TDPP-BBT/Ca/Al.

We first checked the effect of the electrodes on the absorption of the TDPP-BBT sample. The absorption in pristine TDPP-BBT samples in the absence of any bias is shown in fig. 4.3(a). The absorption spectrum of a spin cast film on glass (black) and that of the spin cast film in a device with (green) and without Al (red) is identical. A weak broadening is observed and splitting or the vibronic of the intra CT is observed in the absorption from the device. The splitting of the intra CT may be due to the interaction of intra CT with the electrode at the polymer-electrode interface.

The electric field dependent absorption from a pristine TDPP-BBT as a function of the reverse bias is shown in the fig. 4.3(b). The application of the reverse bias did not show any changes in the pristine TDPP-BBT sample. We have also checked the changes in the absorption by application of a forward bias but no changes were observed. In current-voltage characteristics, the current saturates in the third quadrant. This corresponds to the saturation region where there is a depletion of mobile charge carriers. Hence, only the negative biased absorption data are of interest and have been presented here.

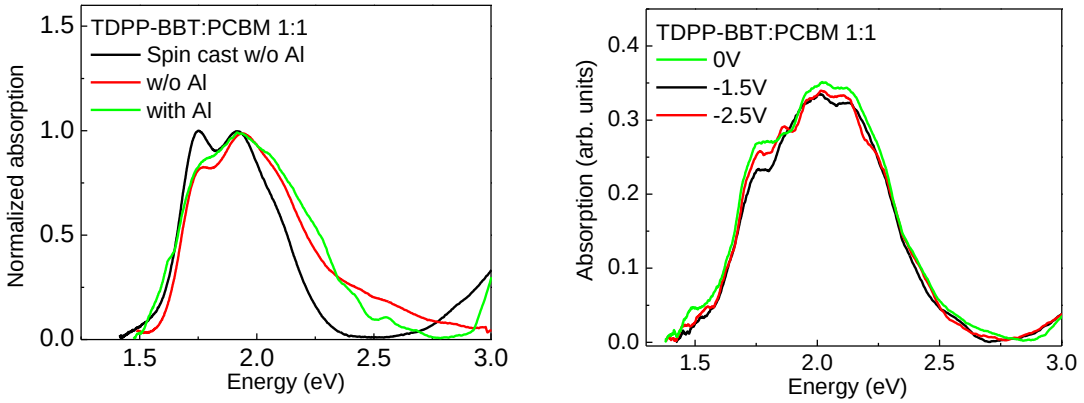

(a) (b)

Figure 4.4 The absorption of the TDPP-BBT:PCBM from a spin-cast film (black), from a device region ITO/PEDOT:PSS/TDPP-BBT/glass without Al (red) and from a device region ITO/PEDOT:PSS/TDPP-BBT/Ca/Al (green). (b) The reverse bias dependent absorption in a TDPP-BBT:PCBM device in the region ITO/PEDOT:PSS/TDPP-BBT/Ca/Al.

Figure 4.4(a) shows the normalized absorption in a TDPP-BBT:PCBM (1:1) sample. The onset of absorption is not significantly affected by the presence of the ITO and the Ca-Al electrodes. Figure 4.4(b) shows the effect of reverse biasing on the absorption in the same sample. There are no changes observed in the onset of the absorption as a function of bias indicating that no low energy states lower than the donor copolymer absorption edge were detected in the absorption studies. Also, the intensity of absorption does not change significantly with the bias. A weak increase in the shoulder at ~1.75 eV is observed which was not seen in bias dependent absorption in pristine TDPP-BBT (fig. 4.3(a)) sample. The changes at 1.75 eV may be bias induced effects due to the presence of PCBM in the blend.

4.2.2 Thiophene based DPP statistical copolymers

To understand the role of intra CT states in DPP-based copolymers, we have extended bias dependent absorption studies to DPP-based statistical copolymer, Poly A and Poly B. In Poly A and Poly B, the thiophene acts as bridge between the carbazole-benzothiadiazole (carbazole-BT) units. Poly A and Poly B vary in the DPP concentration, with Poly B having the higher DPP fraction. Figure 4.5 shows the absorption spectra from a pristine Poly A device with a back electrode. The absorption shows no changes as a function of the bias.

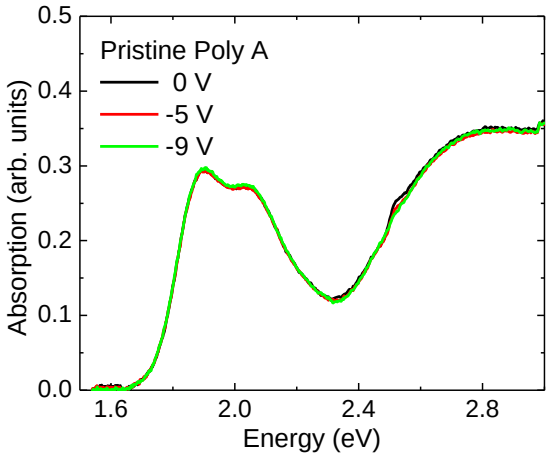

Figure 4.5 The absorption spectra from pristine Poly A device in the presence of an external bias 0 to - 9V.

The absorption spectra from a Poly A:PCBM device is shown in fig. 4.6(a). Unlike the pristine sample, where there is no change in the absorption spectrum even in the presence of a high reverse bias, the onset of the absorption in the blended sample redshifts with the application of a negative bias. Comparing figs. 4.5 and 4.6(a), it is clear that the presence of PCBM in the Poly A:PCBM blended film results in the observable changes with the application of an external bias. For Poly A:PCBM sample, the external bias affects the low lying energy states in the blend but not in the pristine sample.

The intensity of the 1.9 eV peak in the absorption spectrum increases as the reverse bias is increased and saturates at ~ -5V. Along with the changes in the intensity, the onset of the intra CT state (circled), redshifts with an increase in bias (reverse) voltage (fig. 4.6(a)). The “onset” is found by extending a straight line in the low energy region where the absorption curve is linear. Since the low energy shoulder (~ 1.6 eV) is attributed to

PCBM, to obtain the onset of the intra CT, we fit the linear region from ~ 20%-50% (which is roughly between 1.65 -1.77 eV) of the absorption maximum.

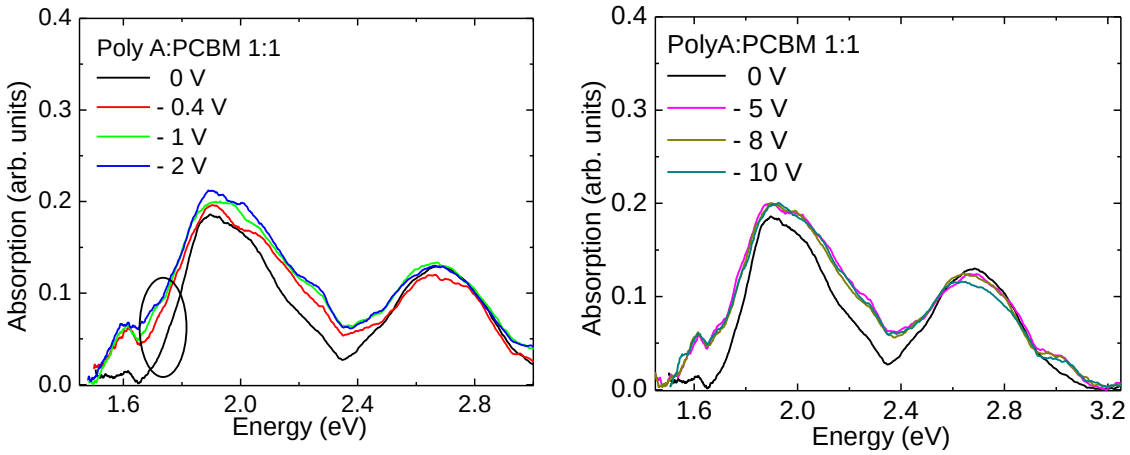

(a) (b)

Figure 4.6 (a) The absorption spectra from a Poly A:PCBM device in the presence of negative bias (0 to -2V). (b) The absorption spectra at higher bias voltages from -5 V to -10 V.

Extending this line to intercept the x-axis gives the onset. The onset as a function of absolute value of applied bias is plotted in fig. 4.7. For biased spectra (-0.4V to -2V), although the curves are close in the region 1.5 to 1.6 eV (fig. 4.6(a)), the x-axis intercept spans over approximately 200 meV. We point out that the onset of donor absorption (1.65 – 1.55 eV) is what changes as a function of the electric field. The low energy peak at 1.6 eV (which most likely arises due to the presence of PCBM) does not change as a function of the applied bias. Since it is well established that a suitable acceptor is helpful in dissociating a bound charge pair, presence of PCBM results in a redshift of the absorption

edge due to biasing. Figure 4.6(b) shows the absorption spectra for bias beyond -5 V. No changes in the intensity or the onset are observed beyond – 5V. We attribute the saturation of the absorption spectra to trapping of the exciton at the Poly A/PCBM interface. Our observations are similar to bias dependent changes in organic multiple quantum well (MQW) structures and porous Si. Since the changes are observed in the donor absorption region, the changes would correspond to the intra CT exciton of the donor copolymer. Hence, the saturation effect beyond -5 V allows an estimation of the intra CT exciton binding energy.

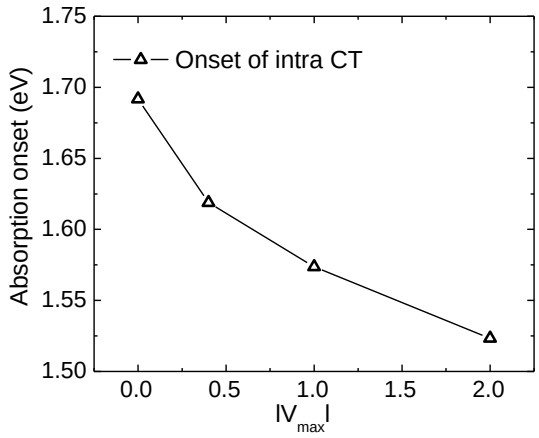

Figure 4.7 The absorption onset of the intra CT state as a function of the bias voltage.

Using $V_{\max}$ = 5 V, $L \approx 100$ nm, $r_{GP} \sim 2.86$ nm, the *BE* is estimated to be ~0.143 eV. The *BE* of the intra CT exciton lies within the 0.050–0.5 eV range found for other CT excitons.[84,85]

The biased dependent absorption in Poly B:PCBM is shown in fig. 4.8. In the Poly B:PCBM blended film, the absorption onset showed no change with an external bias. In

other words, it implies that the quantum confined Stark effect is not strong enough in this heterojunction. In Poly B:PCBM samples it is possible that an unstable CT state is formed, not detected in the steady state optical absorption spectroscopy.

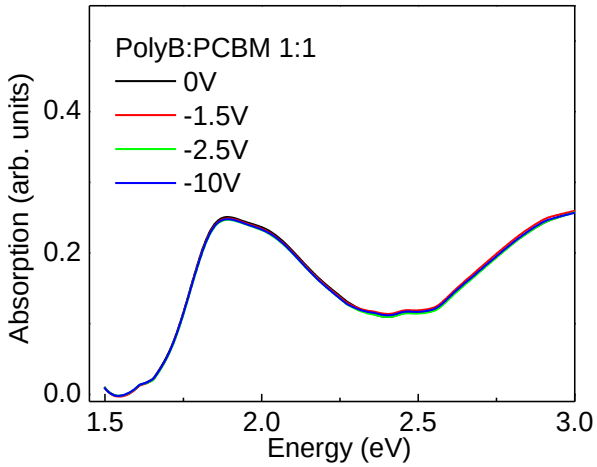

Figure 4.8 The absorption spectra from a Poly B:PCBM device in the presence of negative bias (0 to -10V).

To summarize, the external bias modified and eventually saturated the steady state absorption in the Poly A:PCBM samples, but not the TDPP-BBT:PCBM and Poly B:PCBM samples. The variation in absorption was detectable in Poly A:PCBM due the exciton confinement at the Poly A/PCBM interface. In the TDPP-BBT blend and Poly B blend it implies that (i) the exciton is strongly bound at the polymer:PCBM interface or (ii) the exciton is weakly bound (inter CT exciton) and already transferred to PCBM, rendering the CT exciton undetectable by steady state absorption spectroscopy.

In order to verify if (i) or (ii) is a plausible explanation, we utilize photocurrent modulation spectroscopy to identify the inter CT states in polymer-fullerene blends and

to understand the relevance of the intra CT state in the formation of inter CT state. Previously, the inter CT states were probed in a P3HT:PCBM BHJ using two photocurrent spectroscopic techniques (Section 3.2, fig. 3.2(b) and 3.3). In the two figures the responsivity (calculated from PC) of the P3HT:PCBM 1:1 device was plotted along with the normalized absorption from the P3HT:PCBM 1:1 blend. The responsivity from the P3HT:PCBM device showed a lower energy onset than the absorption onset. The low energy feature in the responsivity corresponds to the onset of the inter CT state in the P3HT:PCBM device. In DPP-based copolymers too, the inter CT states were probed in the copolymer:PCBM blends using two PC techniques. The spectral PC from the devices was also used to characterize the device responsivity and the EQE.

4.3 Photocurrent Spectroscopy - Probing Intermolecular Charge-Transfer States

4.3.1 PDPP-BBT: PCBM devices

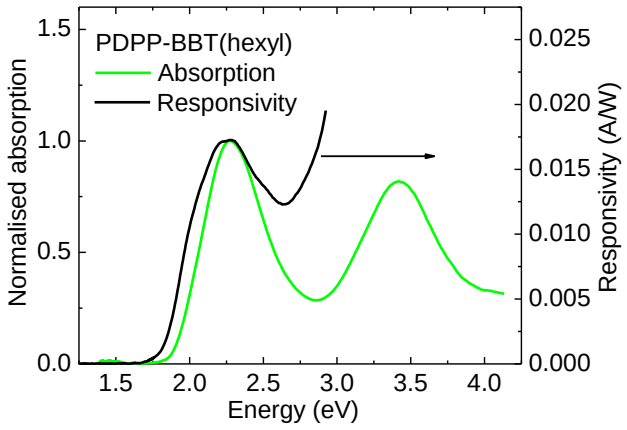

Figure 4.9 The normalized absorption (green) and the monochromatic PC responsivity of a pristine PDPP-BBT device.

The normalized absorption (green) of the pristine PDPP-BBT film is shown in fig. 4.9. The normalized absorption spectrum was calculated by normalizing the spectrum to the maximum intensity of the donor absorption. The responsivity (black) calculated from monochromatic PC of pristine PDPP-BBT (sample1) is shown in the same figure. The responsivity closely follows the absorption and the onsets are not vastly different. The maximum responsivity is 0.0172 A/W at ~2.3eV, which gives EQE to be ~ 4% at 2.3eV.

The normalized absorption (grey) and the responsivity (black) of PDPP-BBT (sample 1):PCBM 1:1 blend is shown in fig. 4.10(a). As seen in the figure, the onset of responsivity is lower than the onset of absorption i.e. the responsivity of the blended device showed an energy feature lower than the absorption. The low energy feature is the indication of a stable inter CT state in the blend. From the onset of inter CT, E_{CT} is calculated by a Marcus fit (Eq. 3.3) to the responsivity curve in the region well below the onset of absorption (< 1.6 eV). The reorganization was fixed at 0.25 eV as in for P3HT:PCBM device. For PDPP-BBT(sample 1): PCBM, the onset of E_{CT} from the monochromatic PC method is ~1.42 eV.

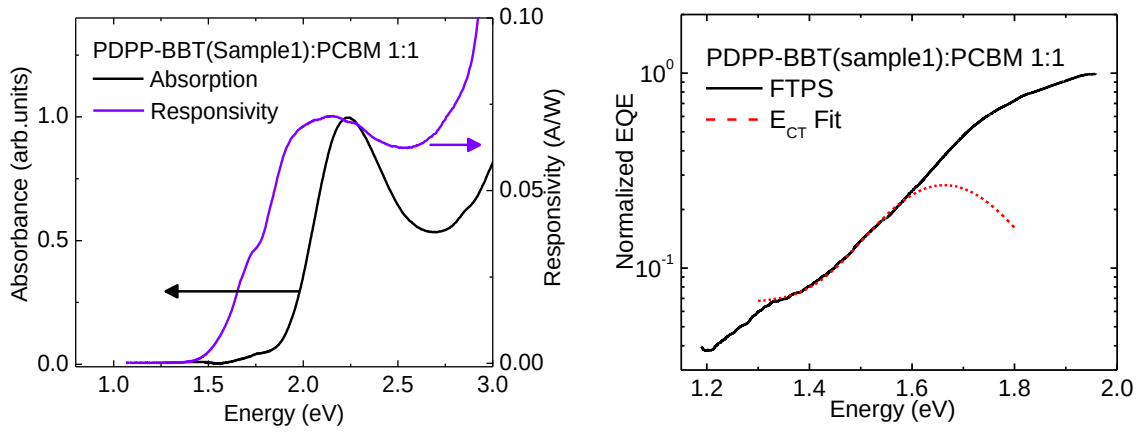

(a) (b)

Figure 4.10 Normalized absorption and responsivity (by monochromatic PC method) of PDPP-BBT(sample1):PCBM. (b) Normalized EQE (black) by FTPS method and the Marcus fit (dashed) to the normalized FTPS EQE in PDPP-BBT (sample1):PCBM is shown.

The FTPS spectrum from the PDPP-BBT (sample1):PCBM is normalized as discussed in Section 3.2 and is plotted as normalized EQE in fig. 4.10(b). The FTPS and the PC spectra are similar for the PDPP-BBT (sample1):PCBM device. Again, using Marcus's theory (Eq. 3.3), we deduce the onset of E_{CT}. Since the inter CT states observed from the EQE spectra extend below the absorption edge, the fit was applied from low energies to ~1.5 eV, depending on the best fit parameters. The dashed line in fig. 4.10(b) shows a fit to the FTPS spectrum for obtaining the energy of the inter CT state. The E_{CT} calculated from the fit to the FTPS PC is ~ 1.42eV.

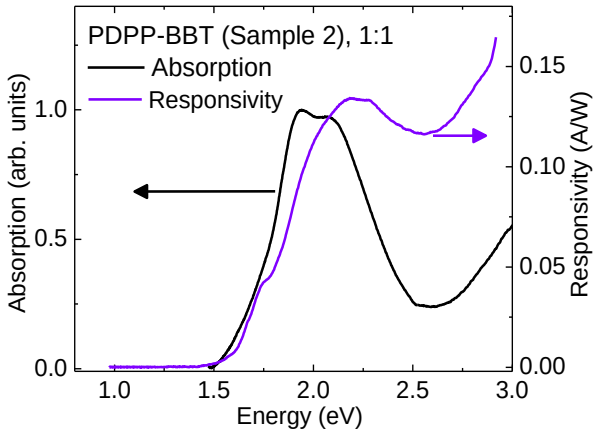

Figure 4.11 Normalized absorption and responsivity (by monochromatic PC method) of PDPP-BBT(sample1):PCBM (b) PDPP-BBT(sample2):PCBM.

The absorption spectrum and responsivity (monochromatic PC) of PDPP-BBT (sample2):PCBM is shown in fig. 4.11. Note that the PDPP-BBT (sample2) shows an absorption edge which is red-shifted compared to the absorption edge of PDPP-BBT (sample1) (see fig. 4.1). From fig. 4.11, the onset of the responsivity and the absorption is seen to overlap, indicating absence of any low energy feature in the blend. The PDPP-BBT (sample2):PCBM device shows no evidence of inter CT absorption. Comparing the responsivity of the blended samples in fig 4.10(a) and 4.11, we also observe an overall higher EQE in PDPP-BBT (sample2) compared to PDPP-BBT (sample1).

4.3.2 TDPP-BBT: PCBM devices

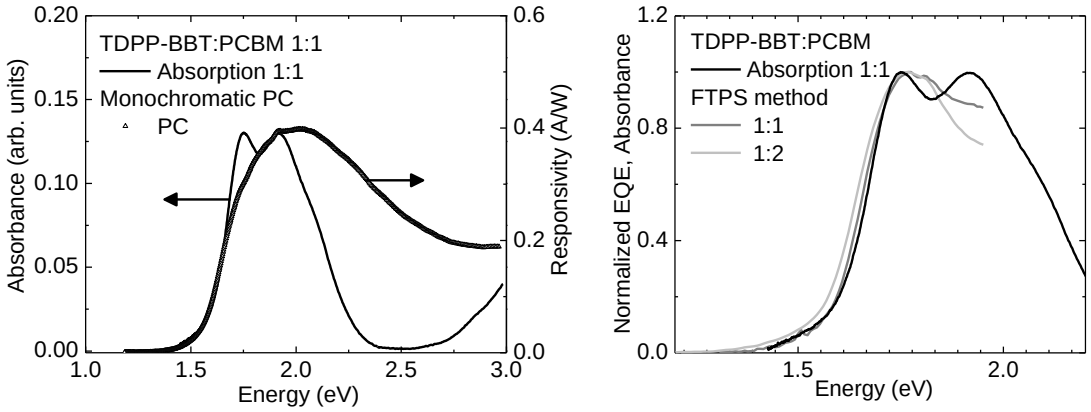

Figure 4.12 (a) The monochromatic PC responsivity and the absorption spectra from the 1:1 sample. (b) Normalized EQE measured by FTPS for TDPP-BBT:PCBM (1:1) and (1:2) devices; absorption spectrum of the 1:1 sample is plotted by the black line.

The absorption spectrum and the responsivity from the TDPP-BBT:PCBM (1:1) sample are shown in fig. 4.12(a). Similar to PDPP-BBT (sample2):PCBM, the FTPS and the PC spectra in TDPP-BBT:PCBM coincide with the absorption edge in TDPP-BBT:PCBM, signaling the absence of any inter CT states. We also increased the amount of PCBM concentration in TDPP-BBT:PCBM in order to detect the inter CT states in TDPP-BBT:PCBM devices. Figure 4.12(b) shows the FTPS EQE spectra in TDPP-BBT:PCBM (1:1) and TDPP-BBT:PCBM (1:2). For comparison, the normalized absorption spectrum from TDPP-BBT:PCBM (1:1) is also plotted in the fig. 4.12(b). No lower energy onset was detected i.e., no inter CT states were detected for a higher concentration of PCBM in TDPP-BBT:PCBM sample. All the results obtained above

have been summarized in Table 4.2. The table lists the E_{CT} values of PDPP-BBT(sample1):PCBM (1:1), PDPP-BBT(sample2):PCBM (1:1), and TDPP-BBT:PCBM (1:1) devices obtained by fits to both the FTPS and PC. The two photocurrent techniques give slightly different values, which may be attributed to the spectral resolution, with FTPS being a more sensitive technique. From column three and four in Table 4.2, we observe that the CT state is detected in the PDPP-BBT:PCBM sample where PDPP-BBT has the largest optical bandgap. For the PDPP-BBT(sample2) (which has a lower bandgap) blended device, no CT state was detected . Similarly, no CT states were detected for the lowest bandgap material (TDPP-BBT) blend either. Also, column five indicates a higher responsivity (and PCE) for blends where no CT states were detected.

Table 4.2 Energy of the inter CT states (E_{CT}) obtained by fits to the FTPS and PC spectra using the Marcus theory

Sample	E_{CT}(eV) FTPS	E_{CT}(eV) PC	Absorption onset (eV)	Responsivity at peak (A/W)	PCE (%)[a]
PDPP-BBT(sample1) :PCBM (1:1)[b]	1.42	1.49	1.70	~0.075	1.5
PDPP-BBT(sample2) :PCBM (1:1)	-	-	1.50	~0.13	-
TDPP-BBT:PCBM (1:1)	-	-	1.43	~0.4	2.8

[a] Ref. 86.

[b] Sample 1.

4.3.3 Poly A: PCBM devices

In order to evaluate the relationship between the presence/absence of inter CT states to the optical bandgap of the polymers, we have extended our studies to statistical copolymers where the bandgap can be tuned more easily. As with the P3HT and DPP-based copolymers discussed so far, we probe the inter CT states in two DPP based statistical copolymer:PCBM blends. The chemical structure of the DPP-based statistical copolymers is shown in fig. 1.2(f). Note that the statistical copolymers have thiophene as a bridge unit connecting the DPP core to the carbazole-benzothiadiazole (carbazole-BT) unit, but Poly B has more DPP fraction compared to Poly A. The normalized absorption spectrum (fig. 4.2(b)) indicates that Poly B has a slightly smaller bandgap than Poly A.

The normalized absorption spectra of Poly A:PCBM along with the monochromatic PC responsivity are plotted in fig. 4.13(a). The PC spectrum shows a low energy onset compared to the absorption spectrum in Poly A:PCBM which is an indication of the presence of inter CT states in this sample. For comparison, the responsivities of pristine Poly A and its blend with PCBM (1:1) are plotted in fig. 4.13(c). The graph indicates (i) a redshift in the onset of PC by addition of PCBM compared to the pristine, and (ii) a significant increase in the responsivity with the addition of an acceptor. The redshift in the PC clearly points towards the formation of a stable inter CT state. From the responsivity curve, the EQE for Poly A:PCBM is approximately 1.5% at 1.8 eV. For further confirmation of the CT states, we measured the FTPS PC from Poly A:PCBM. The FTPS PC is normalized using the method discussed in Section 3.2 and is plotted as normalized EQE on a semi-logarithmic scale as shown in fig. 4.13(b). The FTPS

spectrum of Poly A:PCBM clearly shows a weak absorption feature lower in energy compared to the regular absorption spectrum. This low energy feature signals the presence of a inter CT state, similar to the PC spectrum (fig. 4.13(a)), in the Poly A:PCBM blended sample. The low energy contribution to both the PCs was fitted using Eq. 3.3. The onset of the CT state from a fit to monochromatic PC is ~1.45 eV and from a fit to the FTPS PC is ~1.36 eV.

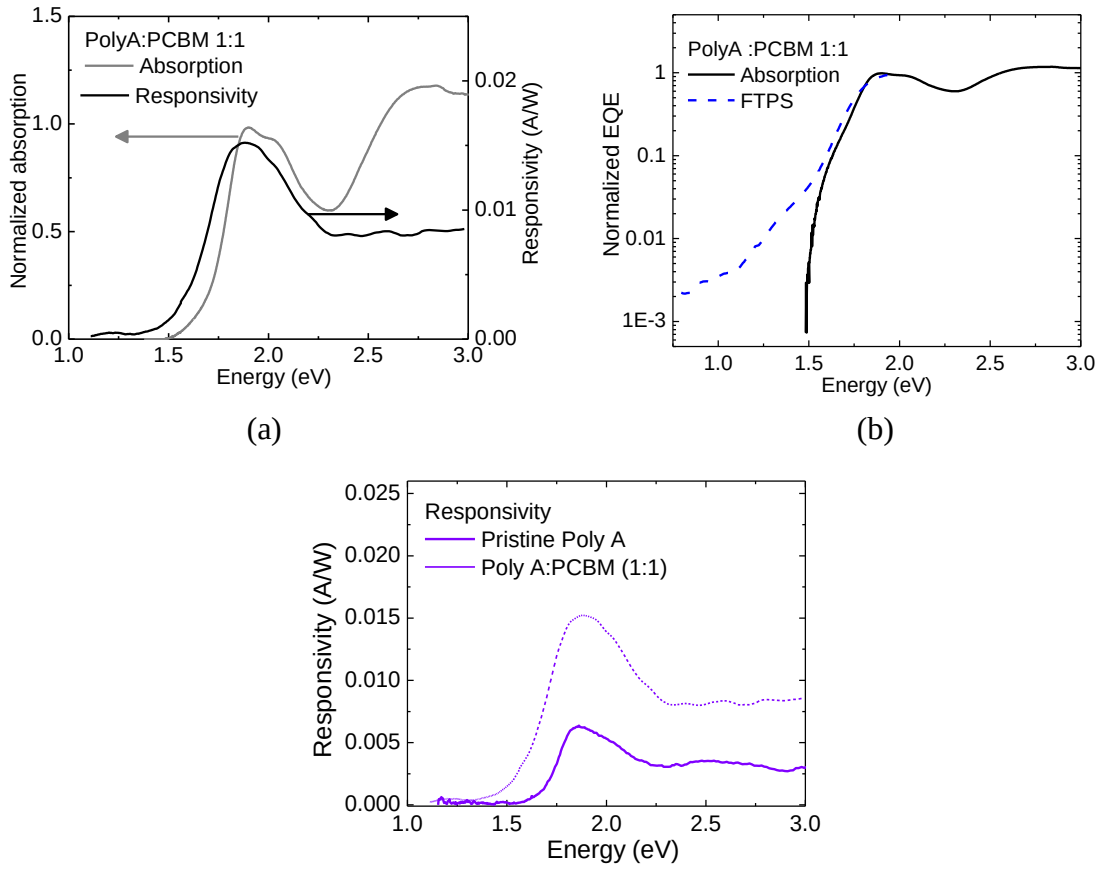

Figure 4.13 Normalized absorption and responsivity of Poly A:PCBM by (a) monochromatic PC (blue), and (b) FTPS (blue dashed). (c) The responsivity of pristine Poly A (solid blue) and Poly A: PCBM (dashed blue).

4.3.4 Poly B:PCBM devices

The normalized absorption and responsivity in Poly B:PCBM (1:1) is shown in fig. 4.14. The onsets of the absorption and responsivity almost overlap, from which we conclude the absence of any low energy CT state in Poly B:PCBM (using photocurrent

spectroscopy). The responsivities of pristine Poly B and its blend with PCBM (1:1) are plotted in fig. 4.14(b). To compare their onsets, the responsivity of the pristine Poly B sample is multiplied by a factor of 22. In contrast to the Poly A, the onset of the responsivity of Poly B: PCBM overlaps with that of the pristine Poly B, signaling the absence of inter CT states. Additionally, the responsivity of Poly B: PCBM is almost an order of magnitude more than pristine Poly B. In terms of the EQE, Poly B:PCBM shows ~ 31% at 1.8 eV. Compared to Poly A:PCBM (~ 1.5% at 1.8 eV), the EQE of Poly B:PCBM is an order of magnitude more. Note that Poly B:PCBM sample had showed no change in the absorption in the presence of an external bias (fig. 4.8), pointing in the direction of weakly-bound charge pairs. It is highly likely that the electric field does not introduce significant changes in the onset or the intensity of the absorption because of the weakly-bound exciton. The unstable CT state at the interface may actually result in a complete transfer of charge from Poly B to PCBM, which can further explain the higher responsivity in this sample compared to Poly A:PCBM.

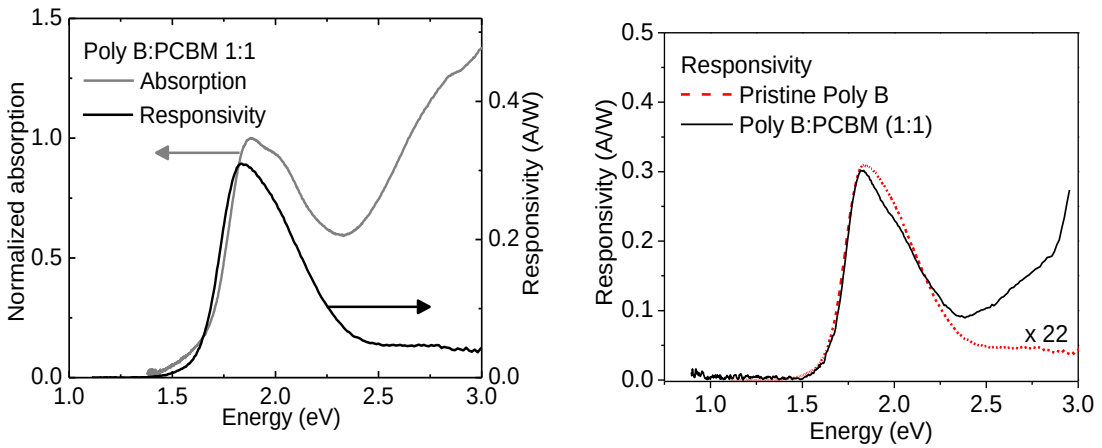

(a) (b)

Figure 4.14 Normalized absorption and responsivity of (a) Poly B:PCBM (b) The responsivity of Poly B and Poly B :PCBM. The responsivity of the pristine is multiplied by a factor of 22.

We explain the stabilization of the inter CT states in our experiment on the basis of the difference in the bandgap energies of the donor polymer and the PCBM acceptor. In a prior work by Hall et al., it was observed that a smaller difference in the band gap energies (or the singlet state energies) between MEH-PPV and CN-PPV results in stabilizing the inter CT state.[51] This work consisted of PL studies and theoretical calculations were done on three PPV-related materials. The HOMO and the LUMO levels of all three polymers calculated theoretically in Ref. 51 is shown in fig. 4.15(a). Note that a cyno-substituted PPV (CN-PPV) is the acceptor polymer, while MEH-PPV and DMOS-PPV act as donor polymers. The difference between the HOMO (H) and LUMO (L) level of DMOS-PPV and CN-PPV (0.55 -0.17 eV) is 0.38 eV. The difference

is specified in fig. 4.15(a) as intra. In DMOS-PPV/CN-PPV, the energy of the inter CT state would be,

$$E_{CT} = E(\text{Intra state of DMOS-PPV}) - 0.55.$$

But the excess energy to convert an intra chain exciton to inter chain exciton is close to the exciton binding energy in PPV 0.35 eV.[52] Hence,

$$E_{CT} = E(\text{Intra state of DMOS-PPV}) - 0.55 + 0.35$$

$$= E(\text{Intra state of DMOS-PPV}) - 0.20. \quad (4.4)$$

In fig. 4.15(b), the E_{CT} is denoted by "inter" and is 0.2 eV below the intra state of DMOS-PPV. Note that the energy of inter CT state was calculated theoretically. DMOS-PPV/CN-PPV had not shown any inter CT states experimentally. In MEH-PPV/CN-PPV, the difference between the intra state of MEH-PPV and CN-PPV (0.63 - 0.44 eV) is 0.19 eV. The E_{CT} can be calculated as,

$$E_{CT} = E(\text{Intra state of MEH-PPV}) - 0.63 + 0.35$$

$$= E(\text{Intra state of MEH-PPV}) - 0.28. \quad (4.5)$$

In fig. 4.15(b), the E_{CT} for MEH-PPV/CN-PPV denoted by "inter" is 0.28 eV below the intra state of MEH-PPV. The inter state in MEH-PPV/CN-PPV is stabilized below the lowest intra state (intra CN-PPV). This stabilization has been attributed to the small bandgap difference in MEH-PPV and CN-PPV.

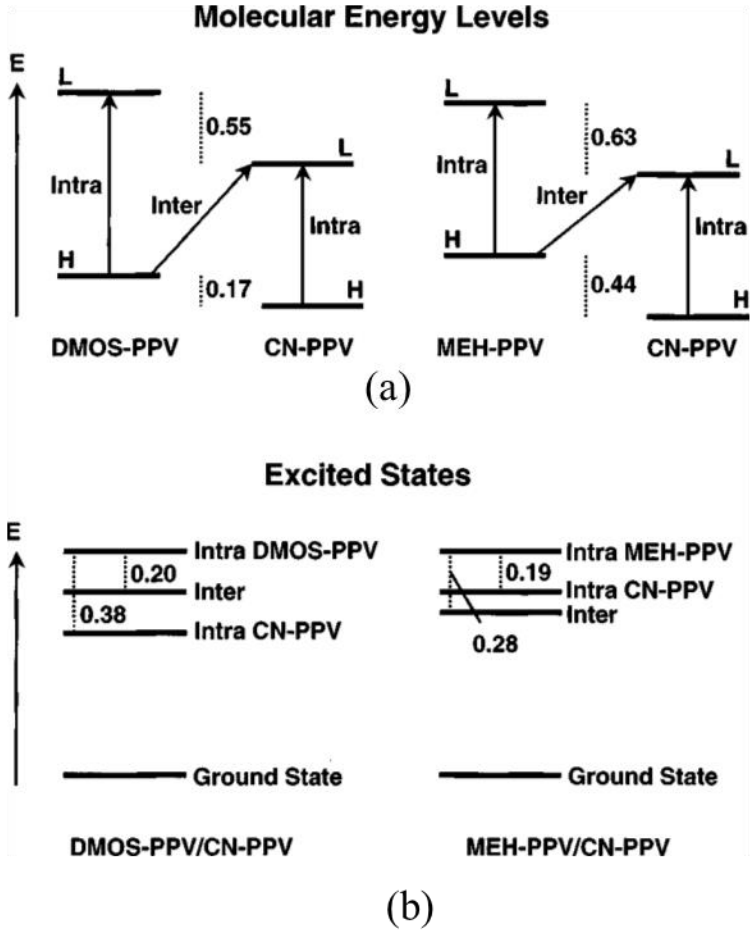

Figure 4.15 (a) The HOMO and the LUMO levels of various PPV-related chains. (b) The position of the lowest interchain and the intrachain excited state in CN-PPV/DMOS-PPV and CN-PPV/MEH-PPV.[Ref. 51]

On the basis of bandgap dependent charge transfer in the PPV-related chains, we evaluate the relation between the bandgap of DPP-based copolymers and the inter CT state detected by PC techniques. It is then instructive to consider the singlet state energy (S_1) difference between the donor polymer and the acceptor, as shown in fig. 4.16. Although a different batch, the DPP copolymers used in this work were similar to the ones used in Ref. 86 where the HOMO/LUMO values of the copolymers were reported. The relevant HOMO/LUMO values for PCBM are 6.1 eV and 4.3 eV, respectively. The S_1 energies are determined from the onset of the absorption spectra for the pristine systems. The inter CT states detected in two DPP-based copolymer-PCBM blends (PDPP-BBT (sample1) and Poly A) is shown schematically in fig. 4.15. No inter CT state is detected in PDPP-BBT(sample2), Poly B and TDPP-BBT -fullerene blends. The difference between the S_1 energies of DPP copolymer and PCBM is denoted by double headed arrows. Compared to PDPP-BBT(sample 1)-PCBM (0.07eV) and Poly A-PCBM (0.2eV), the S_1 energy difference between Poly B-PCBM (0.3 eV), and TDPP-BBT – PCBM (0.37 eV) is higher. Similar to the MEH-PPV/CN-PPV (Ref. 50), inter CT state is observed (stabilized) when S_1 energy (intra state) difference is small (< 0.2 eV, here). For S_1 energy $\geq$ 0.3 eV, no inter CT state is detected. We point out that the inter CT states are not observed even in PDPP-BBT (sample 2), which has a similar band gap to TDPP-BBT.

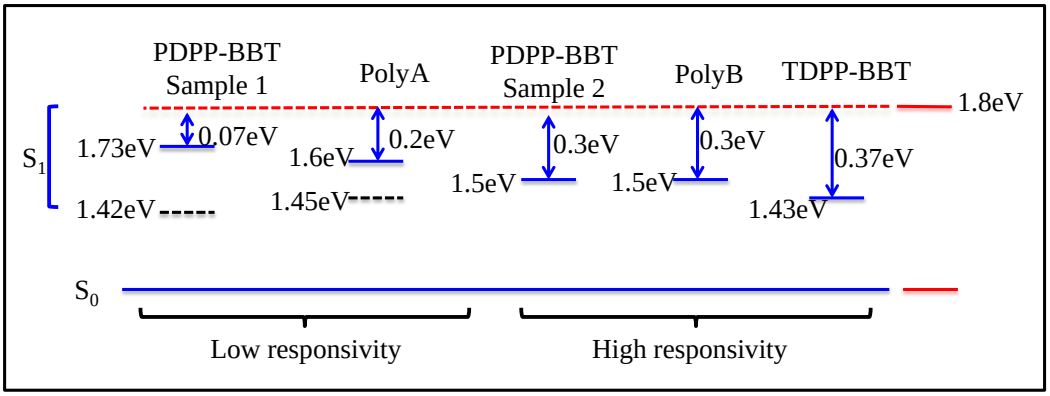

Figure 4.16 The singlet state (S_1) energies of the DPP based polymer and PCBM are shown. The difference between the S_1 (solid lines) energies of the donor polymers with respect to PCBM, and the relative position of the inter CT state (dashed line) are schematically shown.

For comparison, let us reconsider the results of inter CT state from the monochromatic PC method from the P3HT:PCBM 1:1 device (Section 3.2). Recall that the optical band gap of P3HT is ~1.9 eV. The difference between the bandgap of P3HT and PCBM is 0.1 eV. The E_{CT} state by the monochromatic PC was found to be ~ 1.21 eV. Similar to some of the DPP-based copolymer systems, a small bandgap difference between P3HT-PCBM, results in a stable detectable inter CT states.

In the DPP based polymer:fullerene blends, a larger difference in the S_1 energies between the donor polymer and PCBM acceptor may result in the formation of an (i) inter CT state that coincides with the S_1 of the donor polymer or (ii) unstable inter CT states. Due to the faster dissociation, the inter CT state would undetectable by FTPS/PC techniques. If (i) was true, the inter CT state is formed but coincides with donor absorption then there is a possibility of a back transfer of the already separated charge.

The back transfer of charges often leads to recombination and should result in a decrease of the photocurrent as seen in emission studies.[87] However, for the DPP based copolymers we observe that the photocurrent and the responsivity (Table 4.2 and fig. 4.16) are higher in devices for which no inter CT states are observed. A possible explanation then is that the inter CT state is not stabilized or disassociates very fast (compared to the time scales of our experiment) in the blends where the low energy state is not detected by photocurrent spectroscopy.

Most likely the differences in the chemical structure of the DPP copolymers do not play a role. The PDPP-BBT samples (1 and 2), which have the same backbone structure, show differences in the formation of inter CT state. Sample 1 which has a lower S_1 energy difference between PCBM clearly shows the formation of inter CT state at 1.42 eV. On the other hand PDPP-BBT(sample2):PCBM does not show any inter CT states. The PDPP-BBT(sample2):PCBM has a responsivity that is almost twice than PDPP-BBT (sample1):PCBM (see Table 4.2). We see the same trend in the DPP statistical copolymers – Poly B shows a higher responsivity compared to Poly A. Furthermore, the absence of the inter CT state in the DPP:PCBM blends is related to a higher photocurrent (responsivity).

Two factors may play a role here-the difference in the S_1 energies and the relative positioning of the singlet states of the donor and acceptor. Looking at other donor-acceptor systems where inter CT states have been observed or calculated in the literature, the S_1 energy difference between the donor and acceptor is usually small [51] or in some cases where the difference is large, the S_1 of the donor is higher compared to PCBM.[48-

50,57] The PC spectroscopy data indicate that for DPP based devices, a larger difference in the S_1 energies of the donor and the acceptor obliterates formation of a stable inter CT states, eventually resulting in a higher responsivity.

In summary, whether the presence of low-lying midgap CT states results in enhanced/diminished photovoltaic efficiency in polymer-based BHJs most likely depends on the choice of the donor polymer. Undoubtedly, the morphology of the blended film, phase separation, excitonic diffusion lengths, and spectral overlap between donor emission and acceptor absorption are major players impacting the overall PCE of organic solar cells compared to only the nature of the inter CT states.[88]

5.

DENSITY FUNCTIONAL THEORY AND TIME DEPENDENT DENSITY FUNCTIONAL THEORY

Theoretical insights are often required to understand the basis of experimental observation. With reference to the optical data presented here, it is important to understand the origin of transitions occurring within the organic monomer or polymer unit. The density functional theory (DFT) and time-dependent (TD) DFT have been implemented to calculate electronic structure and identify the origin of optical transitions within a chromophore of the conjugated systems. Our main focus of this work was on the statistical copolymers: Poly A and Poly B. The purpose of DFT calculation is to optimize and calculate the electronic ground state of the Poly A and Poly B monomer. After optimization, the probability of transition was calculated using TDDFT, which also gives the oscillator strength of the various transitions.

5.1 Introduction

5.1.1 Density functional theory

The stationary state of any N electron system can be defined in terms of N-electron wave functions. The information about any N-electron (interacting) system can be obtained by solving the Schrodinger equation given by

$$\hat{H} = -\frac{\hbar^2}{2m}\sum_i \nabla_i^{\,2} + \frac{1}{2}\sum_{i\neq j}\frac{e^2}{|r_i - r_j|} - \sum_i \sum_I \frac{Z_I e^2}{|r_i - R_I|} + \frac{\hbar^2}{2}\sum_I \frac{\nabla_I^{\,2}}{M_I} + \frac{1}{2}\sum_{I\neq J}\frac{Z_J Z_I e^2}{|R_J - R_I|}, \quad (5.1)$$

where, m is the electron mass, M is the nuclear mass, and Z_I the nuclear mass of *I*th nuclei. The first three terms in the Eq. 5.1 are the kinetic energy operator of electrons, the Coulomb potential energy operator between two electrons, and the Coulomb potential energy operator between the electron and the nucleus. The fourth and the fifth term are the kinetic energy and the Coulomb potential energy between the nuclei, respectively. The above equation can be simplified under Born-Oppenheimer (BO) approximation. According to BO approximation the electronic and nuclear dynamics can be separated by taking into account the fact that nuclei are massive, and hence, their coordinates do not change significantly with time. In which case, the kinetic energy of the nuclei is neglected and the fifth term in Eq. 5.1 is just a constant (const.). The Hamiltonian $\hat{H}$ in Eq. 5.1 simplifies as

$$\hat{H} = -\frac{\hbar^2}{2m}\sum_i \nabla_i^{\,2} + \frac{1}{2}\sum_{i\neq j}\frac{e^2}{|r_i - r_j|} + \sum_I \sum_i \frac{Z_I e^2}{|r_i - R_I|} + const. \tag{5.2}$$

i.e. $$\hat{H} = \hat{T} + \hat{V}_{ee} + \hat{V}_{Ne}. \tag{5.3}$$

The solution of the Hamiltonian is the electron wavefunction Ψ_e, energy E_e. The total energy of the N-electron system can then be written as

$$E_{tot} = E_e + E_{nuc}, \tag{5.4}$$

where, E_{nuc} is the nucleus-nucleus repulsion energy constant. For large values of N, it is difficult to solve the Hamiltonian exactly given by Eq. 5.2. However, there are methods available to solve the issue of calculating ground-state energy of N electron system.

One of the methods is a variational method such as the Hartree-Fock (HF) method. It expresses the total wavefunction Φ in terms of Slater determinant of orbitals, $\varphi_i(\vec{r_j})$

$$\Phi(\vec{x}_1,...,\vec{x}_N) = \frac{1}{\sqrt{N!}} \begin{vmatrix} \varphi_1(\vec{r_1}) & \varphi_2(\vec{r_1}) & ... & \varphi_N(\vec{r_1}) \\ \varphi_1(\vec{r_2}) & \varphi_2(\vec{r_2}) & ... & \varphi_N(\vec{r_2}) \\ \vdots & \vdots & \vdots & \vdots \\ \varphi_N(\vec{r_1}) & ... & ... & \varphi_N(\vec{r_N}) \end{vmatrix}. \quad (5.5)$$

Each orbital satisfies the Hamiltonian, $\hat{H}_i \varphi_i(\vec{r_j}) = E_i \varphi_i(\vec{r_j})$. The total HF energy can be written as

$E_{HF} = \sum_i E_i +$ Coulomb energy due to electrostatic repulsion between electrons

+exchange energy. (5.6)

The exchange energy originates due to antisymmetric nature of wavefunction. It can be interpreted by saying that the two electrons flip position during interaction. Although, the use of Slater determinant greatly simplifies solving Schrodinger equation, it does not take into account the correlation energy E_C due to non-classical Coulomb interaction between the electrons. The correct total energy can be given by

$$E_{correct} = E_{HF} + E_C. \quad (5.7)$$

Another method to calculate the electronic structure is based on DFT. In 1964 Hohenberg and Kohn proposed, that the electron probability density should be enough to deduce the electronic properties of the system. The single-particle density of the ground state of N interacting electrons at position *r* can be written as

$$n_0(\vec{r}) = N \sum_\sigma \int d\vec{x}_2 ... \int d\vec{x}_N \left| \psi_0(\vec{r}, \sigma, \vec{x}_2, ... \vec{x}_N) \right|^2. \quad (5.8)$$

Here ψ_0 is the ground-state wavefunction of the system at position ***r***, and spin σ. According to the Hohenberg-Kohn theorem for N interacting electron systems, the particle density is enough to derive properties of the system. They also proved that the ground state density is unique and corresponds uniquely to an external potential. In other words, choosing an appropriate external potential would result in a unique ground state. The total energy functional can therefore be written as [89]

$$E_{tot}[n] = T[n] + W[n] + V_0[n], \tag{5.9}$$

where, $\hat{V}_0$ is the external potential (such as from nuclei) associated with the density $n(\vec{r})$ and $\psi[n]$ is the ground state wavefunction which produces the density $n(\vec{r})$.

Kohn-Sham formalism took into account the Hohenberg-Kohn theorem and showed that even a noninteracting electron system must be able to produce a unique ground state density. Given any N interacting electron system, one starts with a ground state density of a N-non interacting system. The density is plugged into the Kohn-Sham equation (Eq. 5.12) and is solved for estimating the unique effective potential. This potential is plugged back into the Kohn-Sham equation to recalculate the density. The iterative process leads to a unique density and eventually to the ground state energy. To calculate the ground state energy of the actual interacting system the final energy functional must take into account the exchange and correlation energy. The total energy of N interacting particles can be written as,

$$E_{tot}[n] = T_{ni}[n] + E_C[n] + E_{xc}[n] + V_0[n], \tag{5.10}$$

where $T_{ni}[n]$ is the non-interacting kinetic energy-, $E_C[n]$ the Coulomb energy-, and $E_{xc}[n]$ the exchange-correlation (xc) energy functional. Finding the ground state of a molecular structure always involves choosing an appropriate xc functional. In this thesis the ground state of Poly A and Poly B monomers has been calculated using different functionals: B3LYP, CAM-B3LYP and M06HF.

5.1.2 Time-dependent density functional theory

Time-dependent density functional theory (TDDFT) is a universal approach for dynamical many-body problems, but requires approximations to account for dynamical exchange-correlation (xc) effects.[89,90] The vast majority of applications of TDDFT are to calculate excitation energies of medium-size and large molecules, with overall accuracies comparable to traditional *ab initio* wave function methods, but much better computational efficiencies.[91,92]

The basic idea behind TDDFT has been formulated as follows. Consider a system of *N* interacting particles. But this time, let the system move in a time-dependent external scalar potential $v(\vec{r},t)$. The system evolves under time and can be expressed by the time-dependent Schrödinger equation,

$$\hat{H}(t)\Psi(\overrightarrow{x_1},..\overrightarrow{x_N},t) = i\frac{\partial}{\partial t}\Psi(\overrightarrow{x_1},..\overrightarrow{x_N},t). \qquad (5.11)$$

The time-dependent Schrodinger equation correlates the external potential to the time dependent wavefunction. Once $\Psi(t)$ has been calculated, it is possible to generate $n(\vec{r},t)$. The one-to-one correspondence between time-dependent potentials and density was

shown by Runge and Gross.[90] This correlation between time dependent potential and density is similar to DFT, except for the time factor. They showed that a unique potential is associated with the dynamics of the system ($n(\vec{r},t)$) and vice versa. The TDDFT is based on the one-to-one correspondence of time-dependent densities and potentials. To begin with, the static Kohn-Sham equations are used to derive *N* ground state orbitals:

$$(-\frac{\hbar^2}{2m}\frac{\nabla^2}{2}+V_{ext}(\vec{r},t)+V_H(\vec{r})+V_{XC}(\vec{r}))\phi_j^0(\vec{r})=\varepsilon_j\phi_j^0(\vec{r}). \qquad (5.12)$$

Self-consistent solutions of ground state Kohn-Sham equations give the *N* static orbitals. These are taken as initial orbitals and are propagated in time:

$$\phi_j^0(\vec{r})=\phi_j(\vec{r},t_0), \quad j=1,\ldots N. \qquad (5.13)$$

This gives the initial density $n_0(\vec{r})=n_0(\vec{r},t_0)$. An initial guess of the time-dependent density functional $n(\vec{r},t)$ is made. By substituting the density, new set of orbitals and the density dependent potential are obtained. Again, self-consistent solution of the orbitals is calculated using

$$(-\frac{\hbar^2}{2m}\frac{\nabla^2}{2}+V_{ext}(\vec{r},t)+V_H(\vec{r},t)+V_{XC}(\vec{r},t))\phi_j(\vec{r},t)=i\frac{\partial}{\partial t}\phi_j(\vec{r},t). \qquad (5.14)$$

In practice, application of TDDFT requires overcoming challenges such as making approximation for the time-dependent xc-functionals and calculating observables (e.g. excitation energy) from time-dependent density.[93]

The Gaussian code does not treat the full time propagation of Eq. 5.14, but instead considers the external time-dependent potential as a weak perturbation. By considering a *linear response regime*, the system does not deviate too much from its initial state. Thus,

one does not need to solve Eq. 5.14 and calculate the new wavefunctions. Instead, one starts with a frequency-dependent response density equation. This equation also includes the Hartree-xc kernel defined as the variation of the xc potential with respect to the density. The frequency at which the density response is finite and self-sustained corresponds to the eigenmode (excitation energy). The eigenmodes are calculated by solving the coupled linear homogenous equations (Casida equations) of the form,[94]

$$\begin{pmatrix} \mathbf{A} & \mathbf{K} \\ \mathbf{K} & \mathbf{A} \end{pmatrix} \begin{pmatrix} \mathbf{X} \\ \mathbf{Y} \end{pmatrix} = \Omega \begin{pmatrix} \mathbf{0} & -\mathbf{1} \\ \mathbf{1} & \mathbf{0} \end{pmatrix} \begin{pmatrix} \mathbf{X} \\ \mathbf{Y} \end{pmatrix}. \tag{5.15}$$

Here, the matrix elements of **K** correspond to the overlap or coupling of the occupied and the unoccupied Kohn-Sham orbitals. The matrix elements of **A** comprises of frequency of transition between the occupied and unoccupied Kohn-Sham orbitals and the elements of the coupling matrix **K**. **X** and **Y** are the excitation and de-excitation matrix. The excitation energies (Ω) are obtained in principle exactly (but depend on the chosen approximation for xc-functional).

Using TDDFT, we calculate first few excitation energies in the monomer units of DPP-based statistical copolymers.

5.1.3 Coulomb attenuated modified -B3LYP

B3LYP is a hybrid exchange-correlation functional which combines the Becke exchange with LYP functional (Becke, three-parameter, Lee-Yang-Parr). This functional combines the Hartree-Fock exchange with other DFT approximations. The three parameters correspond to the coefficient of the linear combination of the functional approximations. Currently, B3LYP is by far the most successful hybrid functional

utilized for theoretical calculations. Unfortunately, this functional does not give satisfactory results when there are long-range interactions involved, such as the CT interactions.

A full Hartree-Fock (HF) asymptotic behavior of the exchange energy is required for CT excitations.[95] A particularly attractive new class of xc functional are the so-called range-separated hybrid functionals.[96-98] This functional includes the long-range factor by taking into account Hartree-Fock exchange and short-range terms by employing local density approximations. The electron-electron interaction can be written as short-range DFT and long-range Hartree-Fock by separating the Coulomb interaction as,[95]

$$\frac{1}{r_{12}} = \frac{1-erf(\mu r_{12})}{r_{12}} + \frac{erf(\mu r_{12})}{r_{12}}. \qquad (5.16)$$

Here, μ is the range separation parameter. By introducing parameters α and β, Yanai et al. rewrote Eq. 5.16 as,[97]

$$\frac{1}{r_{12}} = \frac{1-[\alpha+\beta erf(\mu r_{12})]}{r_{12}} + \frac{\alpha+\beta erf(\mu r_{12})}{r_{12}}, \qquad (5.17)$$

where, α (β) defines the contribution of HF to short-range (long-range) and must satisfy $0 \le \alpha+\beta \le 1, 0 \le \alpha \le 1, 0 \le \beta \le 1$. At α=0.2, β=0, Eq. 5.17 reduces to B3LYP i.e. a simple ($1.0 r_{12}^{-1}$). For α=0, β=1, Eq. 5.16 reduces to Eq. 5.16 i.e. a long-range correlation (LC). On the other hand, α=0.19, β=0.4, gives the Coulomb Attenuated Modified-B3LYP (CAM-B3LYP) functional.[97] The success of this function is found in correctly predicting CT state in zincbacteriochlorin (ZnBC)–bacteriochlorin (BC) complex: a model system for studying energy transfer in photosynthesis.[99]

5.1.4 Minnesota functionals

The Minnesota functionals (e.g. M06HF) are set of hybrid functionals developed by Dr. D. Truhlar and group at the University of Minnesota. In Ref.95 Zhao et al. proposed mixing full HF-exchange with DFT to account for the long-range interactions. M06HF combines local xc with non-local exchange. The local xc is obtained from the generalized gradient approximations (GGA), where the functional $E_{XC}[n]$ depends on the spin of electron and density gradient at the point of calculation.

5.2 Results and Discussion

The electronic orbitals and excitation energies of all DPP-based copolymers was computed using the Gaussian 09 package.[100] Single monomer units of the DPP polymer were constructed using Gaussview 5.0, optimised using B3LYP, CAM-B3LYP and M06HF functional and 3-21G* or 6-21G* set provided in Gaussian 09 package. CAM-B3LYP hybrid functional and polarized 6-31G* basis set were used to optimize and calculate the absorptivity in statistical copolymer units.[28] The basis sets are the functions combined linearly: such as atomic orbital-like basis functions combined to give MOs. The 6-31G basis set follows the *split-valence* notation given by *X-YZ*G. Since the valence electrons are the most important ones in the formation of MOs, the valence orbitals are constructed by combination of multiple basis function. 6-31G(d) or 6-31G* corresponds to 6 core Gaussian orbitals, while the valence orbitals are split into combination of 3 primitive and 1 primitive Gaussian function. The "*" represents the addition of d- and f-type orbitals.

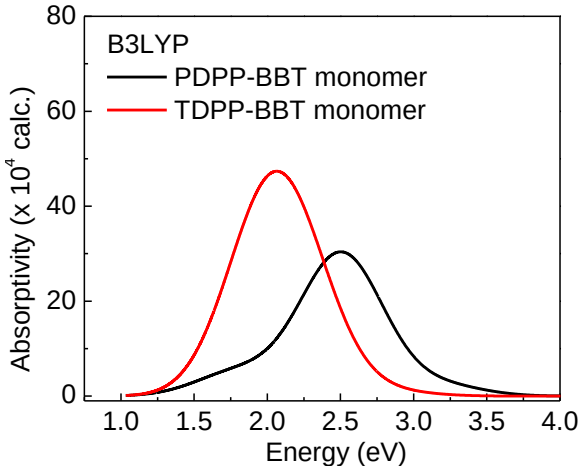

Figure 5.1 The absorptivity of PDPP-BBT and TDPP-BBT calculated using B3LYP/3-21G* in Ref. 99.

The single monomer units of PDPP-BBT and TDPP-BBT were optimized using B3LYP hybrid functional and 3-21G* basis set. Later, TDDFT was utilized to calculate the absorptivity of the monomer units. The results from TDDFT are reproduced here. Figure 5.1 shows the calculated absorptivity in PDPP-BBT (black) and TDPP-BBT (red) monomer unit. The onset of absorption in TDPP-BBT unit is lower than that of PDPP-BBT, as observed experimentally (fig. 4.2(a)). A stark difference seen between fig. 5.1 and fig. 4.2(a) is the presence of single broad feature spanning 1- 3.5 eV. Different functional with higher Hartree-Fock contribution were also utilized to optimize the monomer structure and to get a better correlation between the calculated and experimental absorptivity. The results of which are published in Ref. 101.

5.2.1 CAM-B3LYP as applied to Poly A and Poly B monomer

B3LYP/polarized 6-31G* was first applied to single monomer units of statistical Poly A and Poly B. Although, the structures could be optimized (not shown), TDDFT of the optimized structure resulted in excitation energies with very low oscillator strength. Since statistical monomer units were longer than PDPP-BBT and TDPP-BBT monomer units, a long-range interaction was considered necessary for better prediction of molecular orbitals (MOs).

Poly A was constructed with one carbazole-DPP unit and three carbazole-BT units, while Poly B was constructed with one carbazole-DPP unit and one carbazole-BT unit. Note that the molecular weight of Poly A is more than Poly B, so it is appropriate for Poly A to be longer than Poly B. To optimize Poly A, the dihedral angles along the chain were fixed. The frozen coordinates would also correlate with the fact that the experimental data collected in this work is from a solid state film and not from a solution. The nitrogen, sulphur, and oxygen are denoted by blue, yellow, and red, respectively. To reduce the computational time, the side chains were replaced by a hydrogen atom. Figure 5.2 shows the optimized Poly A monomer. The carbazole, thiophene, core DPP, and the carbazole-BT units have been specified for future reference. Figure 5.3 shows the HOMO, LUMO, the next lower (HOMO-1) and the higher (LUMO+1) MOs for an optimized Poly A monomer obtained from ground state DFT calculations. Both the HOMO and the LUMO are distributed over the thiophene-DPP unit. The HOMO-1 resides mainly on the carbazole-DPP unit while the LUMO+1 reside on the carbazole-BT chain units.

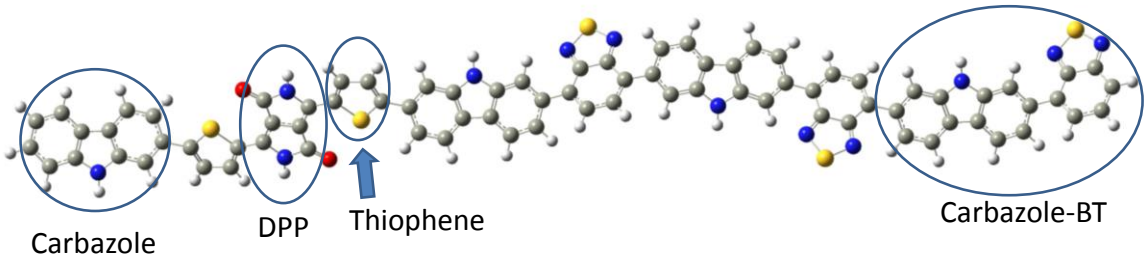

Figure 5.2 The optimized structure of Poly A indicating various units.

The DFT calculations of a slightly different monomer: three carbazole-BT units attached to the carbazole side of carbazole-DPP unit were also performed. For this structure frozen dihedral angles did not optimize the monomer. The structure was optimized without fixing dihedral angles. The MOs of the optimized structure are shown in fig. 5.4. The HOMO and the LUMO orbitals still reside on the DPP units, resulting in the large overlap in the spatial extent of the HOMO and LUMO orbitals. The HOMO-1 and the LUMO+1 orbital are also similar to HOMO-1 and LUMO+1 of Poly A shown in fig. 5.3. Thus, the presence of the carbazole-BT units on the carbazole-BT side does not introduce any significant difference in the ground state MO of the monomers.

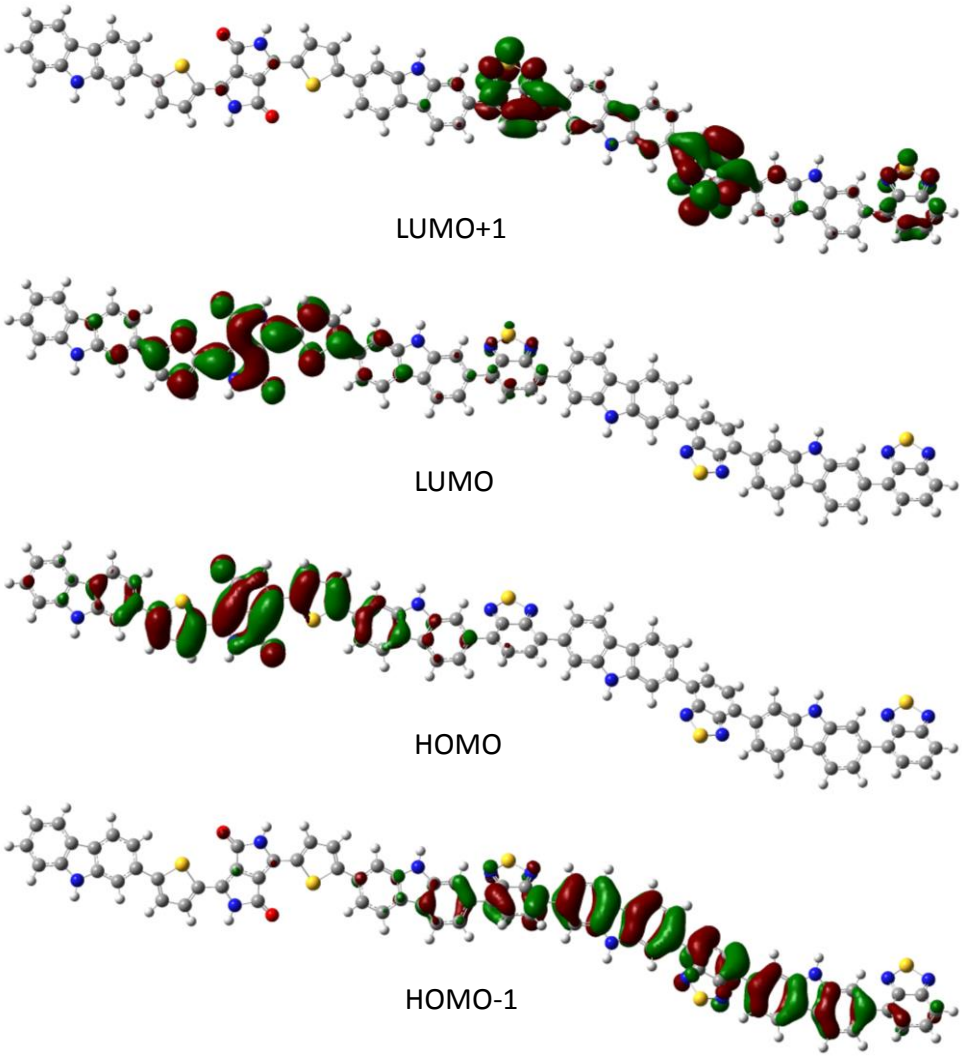

Figure 5.3 The HOMO, LUMO and the next lower, higher MOs of Poly A monomer calculated using CAM-B3LYP/6-31G(d). The red and green represent the phase of the MO.

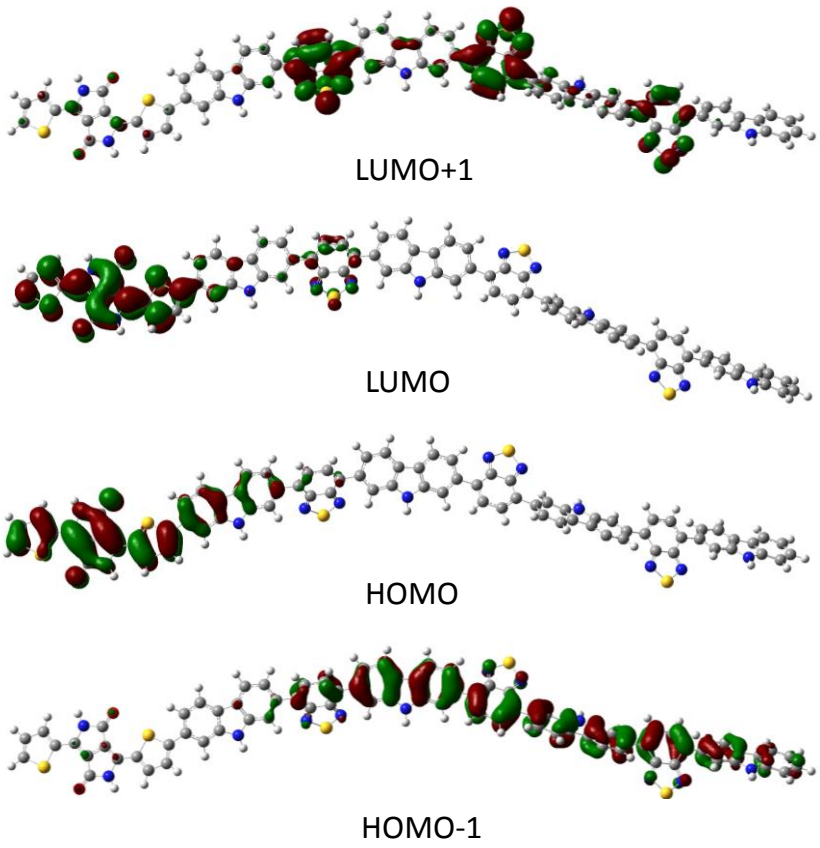

Figure 5.4 The HOMO, LUMO, next lower and higher MO levels in Poly A monomer with three carbazole-BT units attached to the carbazole-BT side calculated using CAM-B3LYP/polarized 6-31G(d). The red and green represent the phase of the MO.

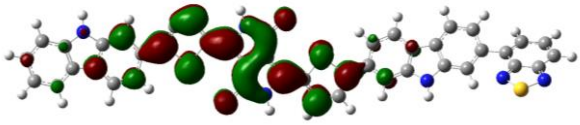

LUMO+1

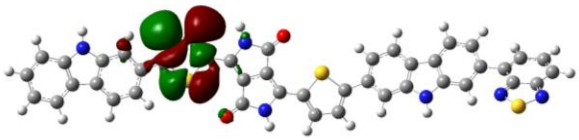

LUMO

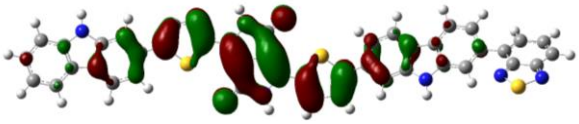

HOMO

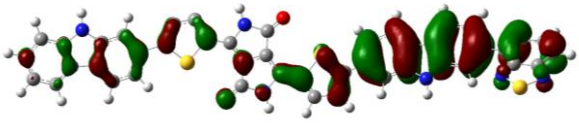

HOMO-1

Figure 5.5 The HOMO, LUMO, next lower and next higher MOs of Poly B monomer calculated using CAM-B3LYP/polarized 6-31G(d) basis set. The red and green represent the phase of the MO.

Poly B was constructed by attaching carbazole-thiophene-DPP-thiophene unit to the carbazole-BT unit. The results of DFT calculation on Poly B monomer is shown in fig. 5.5. The MOs for Poly B are different than Poly A. The HOMO is spread over the DPP core and partially over the thiophene-carbazole unit. It is more delocalized than the HOMO of Poly A. The LUMO shows hardly any charge density on the DPP core. However, the LUMO+1 orbital resides mainly on the DPP core. The HOMO-1 is

delocalized over the carbazole similar to the HOMO-1 of Poly A (fig. 5.3). Although the MOs may not reflect the optical response of the many-body system that arises from a superposition of single-particle excitations, there are clear differences in the spatial location of the electron and hole wavefunction in the two molecules.

To understand the contribution of the orbitals in excitations, we performed TDDFT calculations on the optimized monomer structure of Poly A and Poly B. The calculated absorptivity of Poly A (black) and Poly B (red) monomer is shown in fig. 5.6. The onset of calculated absorptivity in Poly B monomer is lower than in Poly A monomer. The calculations correctly predict the bandgap of Poly B to be lower than that of Poly A as observed experimentally (see fig. 4.2(b)).

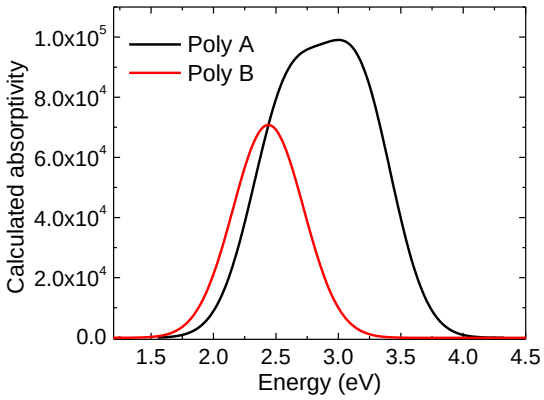

Figure 5.6 The calculated absorptivity of Poly A and Poly B monomer using CAM-B3LYP and polarized 6-31G(d).

To understand the origin of excitations, we consider the first excitation (lowest singlet) in the result of TDDFT calculation. The contribution of each transition is calculated by using,

$$Contribution = (2C^2) \times 100\%, \quad (5.18)$$

where, C is the coefficient of transition. The factor "2" accounts for the spin. For Poly A, the lowest excitation is from the HOMO to LUMO orbital only with a 100% contribution. The DFT calculations in fig. 5.3 also show a maximum overlap, indicating absence of any charge separation within the monomer and a lower intra CT character. In Poly B, the lowest excited state has major transitions from the HOMO to LUMO and HOMO-1 to LUMO. It is observed that ~75% of the absorptivity results from a HOMO to LUMO-type transition whereas 25% is from HOMO-1 to LUMO. The contribution of mixed orbitals to the lowest excitation in Poly B is an indication of a stronger intra CT state of the pristine monomer. A stronger intra CT implies a larger charge separation within Poly A than in Poly B. Thus, the charges dissociate more efficiently at the Poly B/electrode interface than at the Poly A/electrode interface. The dissociation of intra CT eventually results in a higher PC in pristine Poly B than in pristine Poly A device. The responsivity of pristine Poly A and Poly B is almost three times that of Poly B (fig. 5.7).

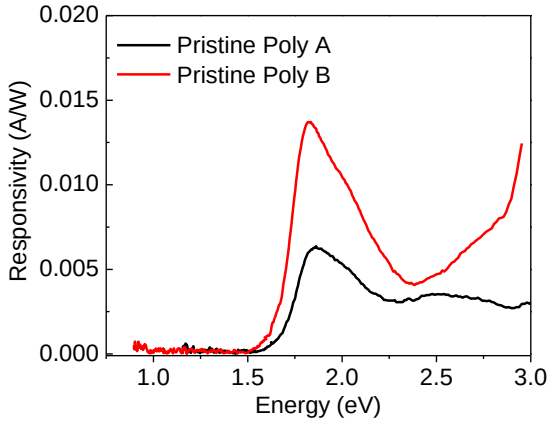

Figure 5.7 The responsivity in pristine Poly A and Poly B devices using monochromatic PC method.

Some discrepancies seen in the calculated absorptivity are (i) higher absorptivity in Poly A compared to the absorptivity in Poly B, and (ii) a single broad feature spanning ~ 1.5 – 3.25 eV for Poly A and ~ 2 - 4 eV for Poly B. The discrepancies between the calculated (fig. 5.6) and experimental (fig. 4.1(b)) spectra are mostly due to the usage of monomers for the calculations whilst the experimental data are from polymer films.

Although, TDDFT calculation using CAM-B3LYP provide some insight into primary excitations, it seems that there is a need for more appropriate xc-functional. In the next section, we present the DFT and TDDFT results from a different hybrid functional: M06HF.

5.2.2 M06HF as applied to Poly A and Poly B monomer

The MOs of optimized structure of Poly A monomer is shown in fig. 5.8. Comparing fig 5.3 and 5.8, we observe the spatial extent of orbitals to be same by CAM-B3LYP or M06HF functional. The HOMO and LUMO are situated on the DPP-thiophene region. The HOMO-1 (LUMO+1) orbitals in Poly A by CAM-B3LYP is identical to HOMO-1 (LUMO+1) orbitals.

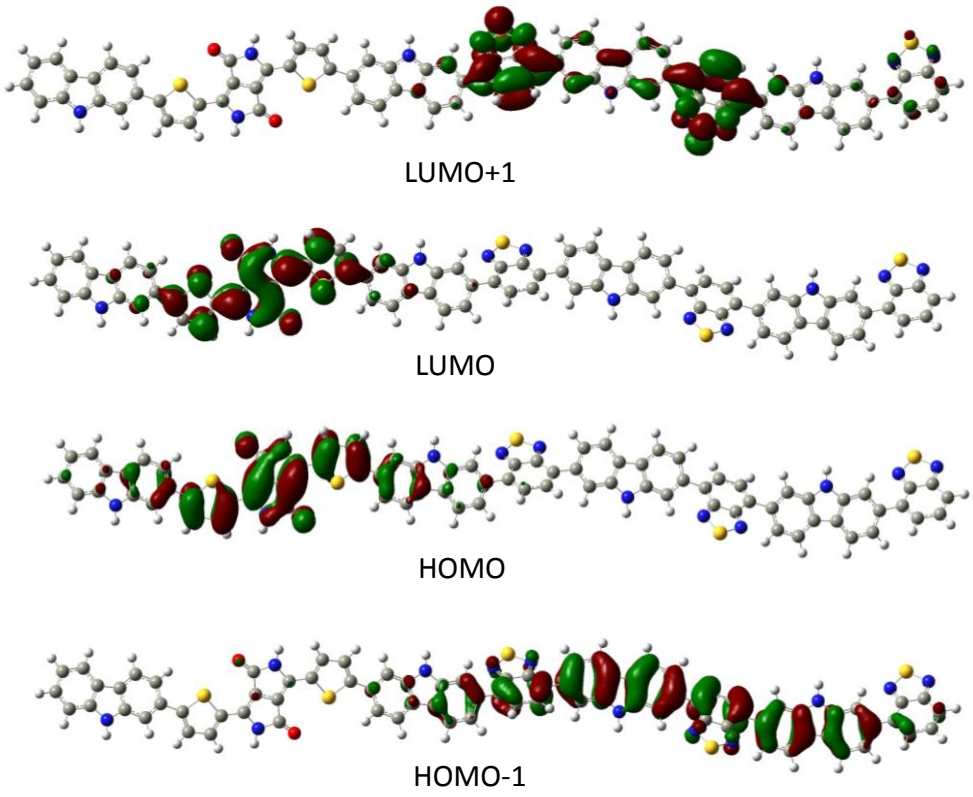

Figure 5.8 The HOMO, LUMO and the next higher MOs of Poly A monomer calculated using M06HF functional and polarized 6-31G(d) basis set.

The Poly B monomer was also optimized using M06HF functional and 6-31G(d) basis set. The computed orbitals are shown in fig. 5.9. The HOMO and HOMO-1 level from M06HF is same as those calculated from CAM-B3LYP (fig. 5.5). In contrast, while the LUMO (from M06HF) is spread over thiophene-DPP unit, the LUMO (CAM-B3LYP) was localized on thiophene unit only. Similarly, the spatial extent of LUMO+1 in Poly B from the two functional is different.

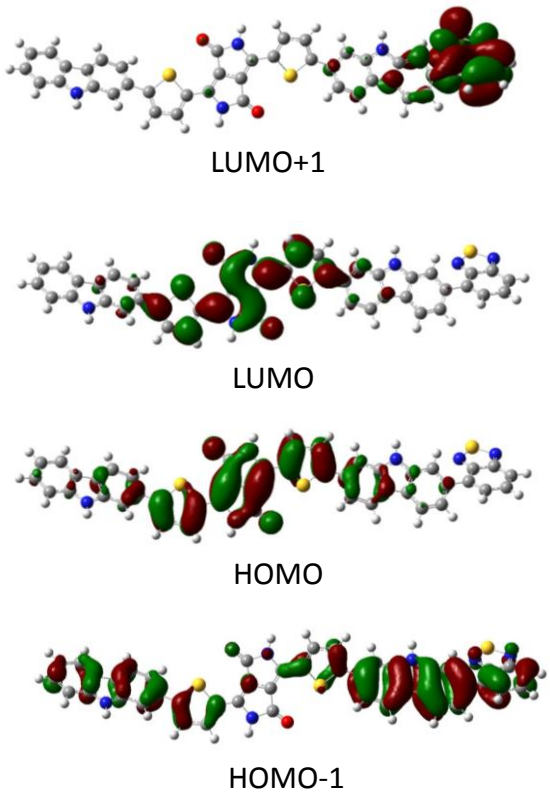

Figure 5.9 The HOMO, LUMO, next higher and lower MOs of Poly B monomer calculated using M06HF functional and polarized 6-31G(d) basis set.

The absorptivity of the optimized Poly A and Poly B monomer was calculated using time-dependent M06HF and polarized 6-31G*. The calculated absorptivity of Poly A monomer and the normalized absorption of Poly A thin film are plotted in fig. 5.10(a). Although, distinct bands are visible in calculated absorptivity, TDDFT overestimates the spectrum. The overestimation (~ 1 eV) is the result of higher HF contribution in the DFT calculation.[102] In Poly A monomer, the low energy peak (~ 3eV) is less intense that the peak at ~4 eV. From the coefficients of first excitation, HOMO to LUMO transition contributes ~85%. Rest of the transitions occur from levels deeper than HOMO to levels

higher than LUMO (e.g. HOMO-8 to LUMO contributes 3%). The calculated absorptivity of Poly B monomer and the normalized absorption of Poly B thin film are plotted in fig. 5.10(b). Again, the calculated absorptivity overestimates the onset of absorption. In Poly B monomer, the low energy peak (~ 3eV) is more intense that the peak at ~4.25 eV. From the coefficients of first excitation, HOMO to LUMO transition contributes ~87% and HOMO-4 to LUMO transition contributes 4 %. Other transitions, from levels lower than HOMO to higher than LUMO have not been discussed here. From fig. 5.10(a) and (b), we do observe a stronger low energy signal at 3 eV in Poly B, suggesting stronger role to intra CT state in Poly B monomer than in Poly A monomer.

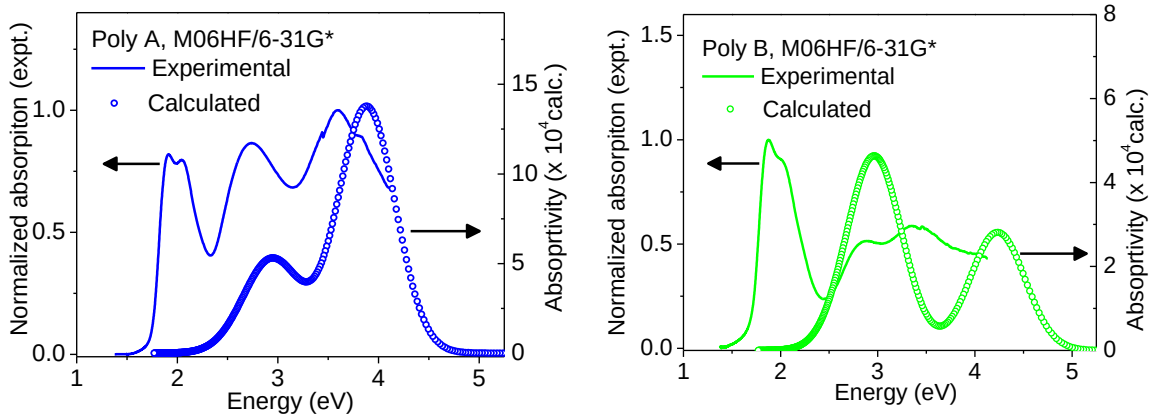

Figure 5.10 (a) The calculated absorptivity in Poly A monomer (solid blue) and measured normalized absorption (circle blue) (b) The calculated absorptivity in Poly B monomer (solid green) and measured normalized absorption (circle green).

To summarize, static and dynamical calculation employing CAM-B3LYP and M06HF functional, help elucidate the spatial extent of electron orbitals in DPP-based statistical copolymer units. The contribution of mixed orbitals to the lowest excitations proves the presence of intra CT nature to the lowest excitations. A higher contribution of mixed orbital transitions in Poly B (than in Poly A) supports the presence of a stronger intra CT nature in Poly B corroborating our experimentally observed absorption spectra (fig. 4.2(b)).

6.

EXCITONIC STATES IN LADDER-TYPE POLYMER

The ladder-type polymer is another homopolymer (apart from P3HT) chosen to identify the role of other excitonic states in OPVs. Previous work by Arif et al. in our lab on triplet vs non-triplet enhanced polymer had shown significant different photovoltaic behavior.[103] The methyl(Me)- and phenyl(Ph)-LPPP polymer (chemical structure in fig. 1.2(b)) was the model system for a non-triplet and triplet-enhanced polymer, respectively. The two systems allowed a study of the involvement of triplet exciton in OPVs. It was further inferred that in PhLPPP, triplet excitonic states play an important role in enhancing OPV efficiency.

We begin this chapter with PC spectroscopic studies of MeLPPP:PCBM and PhLPPP:PCBM devices to identify the CT excitons and compare responsivity of the two devices. We observe that although CT states are detected in both the blends, the responsivity of PhLPPP:PCBM is significantly higher than MeLPPP:PCBM. The higher responsivity in PhLPPP:PCBM is attributed to the presence of triplet excitons in PhLPPP even at room temperature. To further clarify the role of triplet exciton in OPV, we estimate the diffusion length of triplet excitons in PhLPPP polymer at room temperature using PIA spectroscopy. Our PIA studies show a significantly larger (three orders of magnitude) diffusion length of triplet excitons compared to the singlet excitons.

6.1 Ladder-Type Polymer Based Devices

6.1.1 Photocurrent spectroscopy

To explore the relationship between the CT states and the photovoltaic response in homopolymers, the photocurrent spectroscopic studies were performed on MeLPPP and PhLPPP. The LPPP based polymers were chosen as the donor polymers since the S_1 energy of LPPP polymers is higher than the S_1 energy of PCBM (acceptor). The chemical structure of the two LPPP based polymer is shown in fig. 1.2 (b). Note: the molecular weight of MeLPPP and PhLPPP is almost same ~14700g/mol. The absorption of a thin spin cast film of MeLPPP and PhLPPP is shown in fig. 6.1(a). The optical band gap of both the LPPP polymers is 2.6 eV. In spite of the two absorption spectra being identical, the previous studies on BHJ devices fabricated in our lab showed that the PhLPPP:PCBM had a higher PCE compared to MeLPPP:PCBM.[103] To identify the source of the higher PCE in PhLPPP blends, we performed monochromatic PC spectroscopy on MeLPPP and PhLPPP blends.

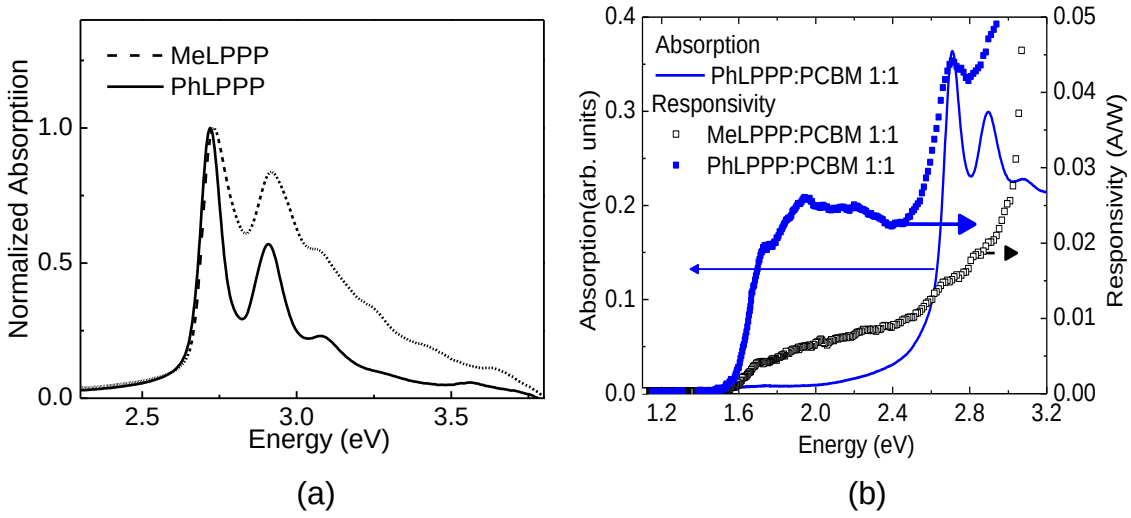

Figure 6.1 (a) The absorption spectra of pristine PhLPPP and pristine MeLPPP. (b)The absorption spectrum of PhLPPP:PCBM 1:1 sample and the responsivities of 1:1 devices.

The monochromatic PC response of the PhLPPP:PCBM (filled squares) and MeLPPP:PCBM (open squares) devices are shown in fig. 6.1(b). The absorption of PhLPPP:PCBM 1:1 sample is also included in the same figure (solid line). The onset of PC in both the LPPP-PCBM samples is lower than the onset of absorption in the blended film, similar to low energy feature observed in P3HT:PCBM (fig. 3.2). The low energy feature in LPPP-PCBM samples indicates the onset of CT states. A Marcus Fit (Eq. 3.3) to the onset of PC in LPPP polymers-PCBM can give an estimate of E_{CT} and is shown in fig. 6.2(a) and (b). The E_{CT} was estimated to be around 1.57 eV and 1.64 eV for MeLPPP:PCBM and PhLPPP:PCBM, respectively. In fig. 6.1 (b), the responsivity of PhLPPP:PCBM device in the range 1.6 eV-2.4 eV is found to be higher compared to the MeLPPP based device, similar to the higher PCE of PhLPPP based devices (fig. 6.2(c)) in Ref. 103.

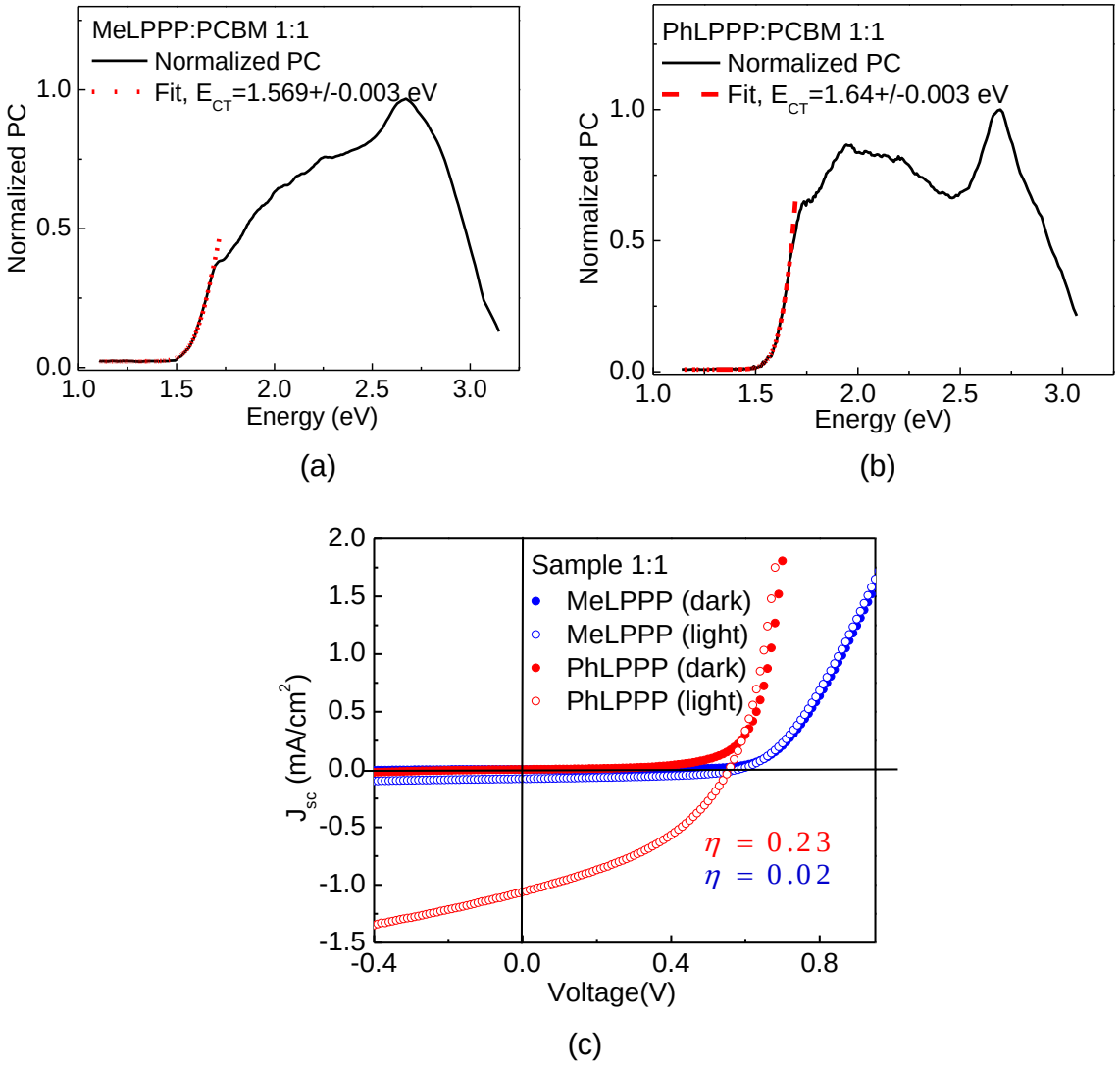

Figure 6.2 Marcus fit to the onset of normalized monochromatic PC in (a) MeLPPP:PCBM (1:1), and (b) PhLPPP:PCBM (1:1). (c) The J-V characteristics in MeLPPP:PCBM and PhLPPP:PCBM reproduced from Ref. 103.

The results from the PC spectroscopy techniques for the LPPP homopolymers are summarized in fig. 6.3. The first singlet excited state for MeLPPP, and PhLPPP is shown

by the blue solid line. The S_1 state of P3HT has also been shown for comparison. The S_1 state of PCBM is provided on the right. In contrast to the DPP-based polymers, the S_1 states of homopolymers lies above the S_1 state of PCBM (acceptor). For each polymer:PCBM blend, the onset of the CT states is shown by the dashed black lines. The double headed arrows represent the difference between the singlet energy of polymer and PCBM. Comparing the MeLPPP and PhLPPP, we see that the CT state is observed in both the LPPP polymers and the difference in the singlet energies of polymer-PCBM is the same (0.7 eV). In spite of the similarities in the S_1 levels and optical feature, the PCE is higher for a PhLPPP sample which was attributed to higher concentration of triplet excitons in PhLPPP even at RT. [103] Other articles in the literature also support the contribution of triplet exciton in OPVs.[104]

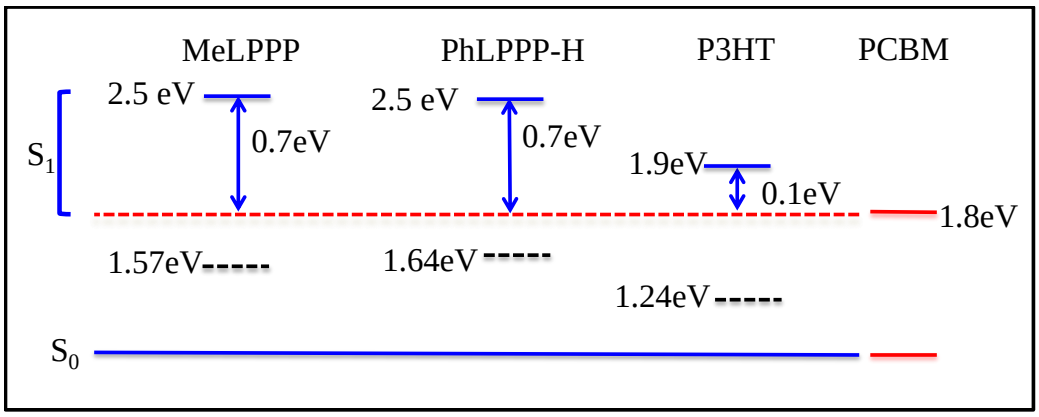

Figure 6.3 The singlet state (S_1) energies of the homopolymer (solid blue) and PCBM (red solid) are shown. The difference between the S_1 (solid lines) energies of the donor polymers with respect to PCBM is denoted by double headed arrow. The relative position of the CT state (dashed black line) is schematically shown.

To elucidate the role of triplet states in the overall efficiency of the device, we have analyzed the diffusion length of triplet excitons using optical modulation spectroscopy.

6.2 Photoinduced Absorption (PIA) – Probing Triplet Excitonic States

Most of the bulk heterojunction OPVs, including those discussed so far in chapter 3 and 4 depend on generation of singlet excitons, their diffusion and dissociation at a polymer/electrode or polymer/acceptor interface. However, the nanometer range diffusion length and short lifetime of singlet excitons may limit their migration to interfaces resulting in fewer CT states and their dissociation, lowering the overall responsivity of device. In order to understand the role of triplet excitons, one of our goal was to measure the diffusion length of triplets in a BHJ architecture. In the literature, a wide range of values for the diffusivity of triplet excitons is found. The diffusivity of triplet excitons in organic semiconductor thin films of PhLPPP was found to be $20 \pm 1 \times 10^{-6}\ cm^2 s^{-1}$,[105] while for a polycrystalline film of a platinum(II) porphyrine complex, PtOEP, the diffusivity was $4 \times 10^{-6}\ cm^2 s^{-1}$ and $6.2 \times 10^{-8}\ cm^2 s^{-1}$ for the monomer and dimer triplets, respectively.[106] Furthermore, the diffusivity in organic crystals such as anthracene is $2 \times 10^{-4}\ cm^2 s^{-1}$.[107] Additionally, the reported lifetimes of triplet excitons in organic materials span a wide range from a few microseconds to a few milliseconds. [106,108] This translates into a large range for exciton diffusion lengths from a few nanometers to a few micrometers. A better knowledge of triplet dynamics would be helpful in enhancing solar cell device efficiency. However, experiments on the dynamics of triplets are lacking primarily due to the difficulties associated with direct

optical studies of triplet states, since, singlet-triplet transitions are forbidden. For instance, the time-resolved spectroscopic techniques of thickness-dependent quenching of excitons [109-113], which have been quite successful in determining exciton diffusion length and diffusivity of singlet excitons, are not available for triplet excitons. Only recently, the use of organometallic polymers and improvements in spectroscopic techniques have made it possible to explore fundamental properties of triplet excitons.[114] Nevertheless, the values obtained for some of these properties have been inconsistent due to the differences in techniques, sample preparations, and methods of analysis.

Since triplet states are populated due to ISC in Pd-incorporated LPPP based polymer even at room temperature, we estimate the diffusion length of the triplets in two PhLPPP polymers – a high molecular weight PhLPPP (PhLPPP-H) and low molecular weight PhLPPP (PhLPPP-L) utilizing photoinduced absorption (PIA) spectroscopy. The molecular weight and the conjugation length of PhLPPP-L and PhLPPP-H are tabulated in Table 6.1.

Table 6.1 The molecular weight (M_n) and conjugation length (l_p) of PhLPPP-L and PhLPPP-H.

	Molecular weight (g/mol)	Conjugation length l_p (nm)
PhLPPP-L	3800	4
PhLPPP-H	14700	14

Our method is based on the quenching of the triplet-triplet (T-T) absorption by acceptor molecules, where the intensity of the T-T absorption depends on the concentration of the acceptor molecules. The method is more generally applicable since it relies only on ISC and not on the phosphorescence. We further show that a phenomenological quasi-one-dimensional (1D) random walk with absorbing wall models the diffusion process well and could be used to deduce the diffusion length from the random walk model and the triplet exciton lifetime.

6.2.1 Estimating diffusion length from triplet-triplet quenching

Schematics of the energy levels and one of the mechanisms of triplet state population is shown in fig. 6.4(a). The photoexcitation of polymer (say by pump beam) results in a transition from S_0 to S_1 energy. The S_1 state can decay to lowest triplet state, T_1, via an intersystem crossing (ISC). This is facilitated by the presence of Pd atoms in the backbone. Eventually, the absorption of probe beam results in the T_1-T_N absorption which is detected using modulation setup as discussed in section 2.2. The T-T absorption spectra collected from PhLPPP-H and PhLPPP-L is shown in fig. 6.4(b). The spectral feature of low- and high- molecular weight PhLPPP is different. The absorption in PhLPPP-H is narrower than PhLPPP-L due to the delocalization of the triplet states in PhLPPP-H polymer compared to PhLPPP-L.[114] Most likely the width of the T-T absorption here arises from a distribution of conjugated lengths due to configurational degrees of freedom which leads to a distribution of π-electron transfer integrals between C-C bonds. Also, the peak position in the two samples is different: the peak appears at

~1.29eV and ~1.32eV for PhLPPP-H and PhLPPP-L, respectively. The weak redshift in PhLPPP-H can be explained on the basis of chain length in polymer. The T-T absorption energy is known to be inversely proportional to the number of monomers in the polymer chain.[114] Thus, higher number of conjugated segments in PhLPPP-H results in a redshift of the T-T absorption peak in PhLPPP-H with respect to the T-T absorption in PhLPPP-L. If the concentration of the Pd atoms is assumed to be the same in PhLPPP-H and PhLPPP-L, there will be less number of Pd atoms available per conjugated segment in PhLPPP-H than in PhLPPP-L. The lower concentration of the Pd atoms will lower the ISC rate and the T-T absorption signal in PhLPPP-H compared to PhLPPP-L.

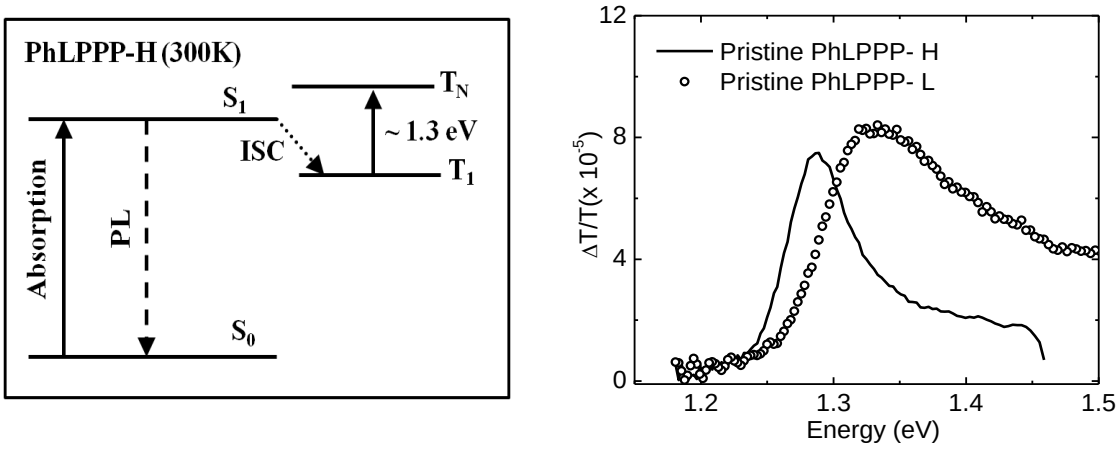

Figure 6.4 (a) The S_1 energy, ISC and the T-T absorption in PhLPPP-H at RT. (b) The T-T absorption in the PhLPPP-H and the PhLPPP-L at RT.

We measure the diffusion length of the triplet excitons in PhLPPP by measuring the quenching of the T-T absorption in PhLPPP. The T-T absorption quenching was

measured by varying the PhLPPP-H:PCBM concentration. PhLPPP:PCBM blends were prepared in various molecular ratios, from 50:1 to 10000:1 by dissolving the components in dichlorobenzene. Equal volumes of various blends were carefully drop cast onto glass substrates, so that the final dried sample areas were same for all blends as determined by visual inspection. No phase segregation was observed for low concentrations of PCBM. Figure 6.5(a) shows the quenching of the T-T absorption for PhLPPP-H as the PhLPPP:PCBM molar ratio decreases. A similar behavior is seen for PhLPPP-L (fig. 6.5(b)).

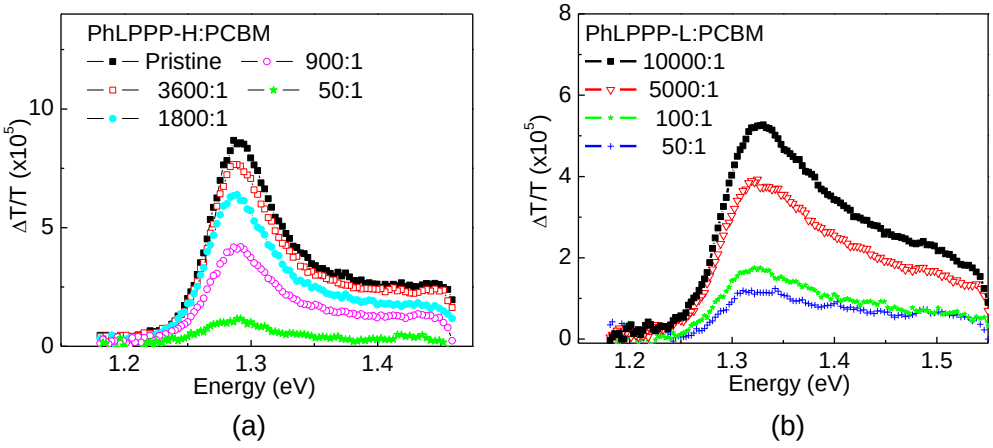

Figure 6.5 (a) Quenching of the PIA signal from PhLPPP-H for selected values of PhLPPP-H:PCBM ratio at 300 K. (b) Quenching of the PIA signal from PhLPPP-H for selected values of PhLPPP-H:PCBM ratio at 300 K.

The observed quenching can be explained by considering a model shown in fig. 6.6(a). In a small volume, PCBM molecules (blue sphere) are scattered along with PhLPPP polymer (red). The triplet excitons of PhLPPP migrate along the polymer chain and hop from one chain to another until they encounter a PCBM molecule. Since the

average distances between PCBM molecules are much larger than singlet exciton diffusion lengths,[115] we attribute the quenching of the PIA signal to the loss of triplet energy to the PCBM molecules situated along the polymer chain.

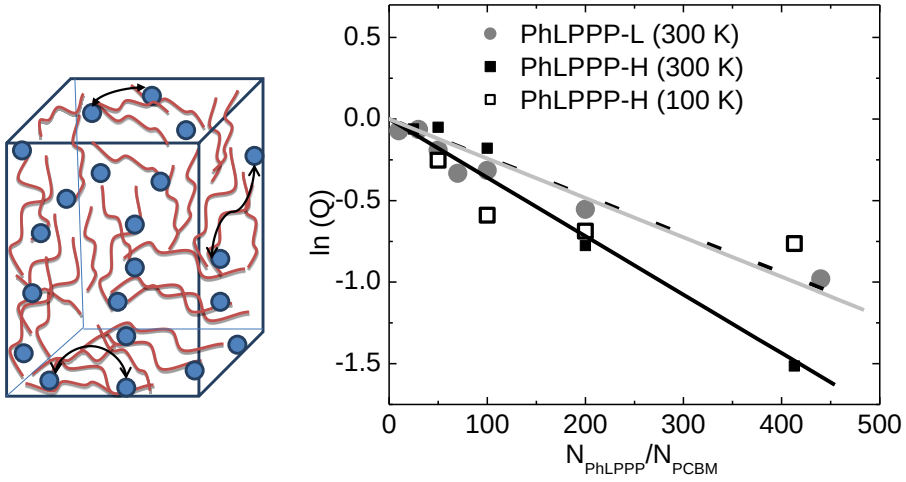

Figure 6.6 (a) Illustration of a quasi-1D model of exciton diffusion through the polymer chains in 3D space. Here *a* is the average distance between PCBM molecules (circles), along the path of diffusion (b) Logarithm of the quenching factor *Q* versus PhLPPP:PCBM molar ratio for PhLPPP-L (filled circles) and PhLPPP-H (filled squares) at 300 K. The open squares are the quenching data of PhLPPP-H at 100 K. The lines are linear fits to the data.

Although PCBM molecules are distributed in a three-dimensional (3D) space, to begin with, we assume the migration of exciton from the location of generation to the PCBM from chain to chain to be a quasi-one-dimensional path. Later, in “Discussion”, we will show that this assumption is appropriate. Moving forward with a 1D model, we

develop model/equations to correlate the observed quenching with the average separation of the PCBM molecules (*a*). This separation is calculated along a sequence of polymer chains in as the product of the molar ratio (*R*), and the length of a single polymer chain. Assuming that the average length of a one dimensional conjugated π system in PhLPPP is l_p, and there are N_{PhLPPP} molecules per N_{PCBM} molecules, then the average distance between the PCBM molecules that the exciton may diffuse is given by,

$$a = \frac{N_{PhLPPP}}{N_{PCBM}} l_P \equiv R l_P . \tag{6.1}$$

Further, for a unimolecular quenching we expect the T-T absorption peak, as determined by −ΔT/T, to depend exponentially on a, or equivalently on R, as follows

$$\frac{\Delta T}{T} = (\frac{\Delta T}{T})_0 \left[1 - e^{-Rl_p/L}\right], \tag{6.2}$$

where, $(\frac{\Delta T}{T})_0$ is the PIA signal for the pristine sample as $R \to \infty$, and *L* is the diffusion length. We find it more convenient for the discussion to introduce a quenching factor Q by the following relation:

$$Q \equiv 1 - \frac{\Delta T/T}{(\Delta T/T)_0} . \tag{6.3}$$

We point out even though the chopper frequency (13 Hz) was used to detect the PIA signals, the amplitudes of the T-T peak change proportionately for the blended and the pristine sample upon changing the chopper frequency. This implies that the amplitude change in $\Delta T/T$ is proportional to change in $(\Delta T/T)_0$. Hence, *Q* is independent of the chopper frequency since it depends on the ratio of the T-T signal of the blend to that of

the pristine sample. Equation (6.3) can be reorganized so that a plot of the signal versus R is expected to be a linear function, as shown in Fig. 6.5(c), whose slope is related to the diffusion length (L) by

$$\ln(Q) = -Rl_p / L \,. \tag{6.4}$$

By plotting ln(Q) vs. molar ratio we can calculate the diffusion length as,

$$L = l_p / Slope \ . \tag{6.5}$$

In fig. 6.6(b), the quenching data for PhLPPP-L:PCBM and PhLPPP-H:PCBM at 300K as well as PhLPPP-H:PCBM at 100K is plotted as filled circles, filled square, and open squares, respectively. The *ln(Q)* is fitted using Eq. 6.4. The fit to PhLPPP-L:PCBM (grey line), PhLPPP-H:PCBM (solid line) and PhLPPP-H:PCBM (dashed line) is also shown. The slope for PhLPPP-L and PhLPPP-H is −0.0024±0.0002 and −0.0036±0.0002, respectively. Using the value of l_p : 4 nm and 14 nm for PhLPPP-L and PhLPPP-H, respectively, and Eq. 6.5, the diffusion length for triplet excitons in PhLPPP-L and PhLPPP-H is calculated as 1.7±0.2 μm and 3.9±0.3 μm, respectively. From the quenching of the PIA data at 100 K for PhLPPP-H, the slope is calculated to be -0.0023±0.0002. Using l_p =14 nm and Eq. 6.5, the diffusion length was estimated as 6.0±0.6 μm.

6.2.2 Triplet lifetimes and diffusivity in phenyl based ladder-type polymers

We further determine the diffusivity of triplet excitons using the following relation,

$$D = L^2 / \tau \,, \tag{6.6}$$

where τ is the triplet lifetime. To determine the lifetime of the triplet exciton, we note that in our PIA experiments, the excitation of the molecules from the ground state, S_0, to the

singlet excited state, S_1, is achieved by a periodic modulation of the exciting laser beam at the chopper frequency. In pristine samples or samples with low concentrations of PCBM (such as those involved in present studies), the triplet lifetime is dominated by a monomolecular decay of the triplets to the ground state. It can be shown that the triplet population (T_1) generated by ISC from S_1 to T_1 with the chopper frequency (f) as [116]

$$|T_1| = \frac{C}{\sqrt{1+(2\pi f\tau)^2}}, \tag{6.7}$$

where C is a constant.[117,118] Since the PIA signal is proportional to the triplet population,

$$\frac{\Delta T}{T} \propto \frac{1}{\sqrt{1+(2\pi f\tau)^2}}. \tag{6.8}$$

By tracking the PIA signal as a function of frequency of the chopper, we can calculate the lifetime τ of triplet in a particular sample. We fix the monochromator at peak value of triplet signal and since we are interested in the amplitude of the periodic signal, we use the *R* channel of the lock-in amplifier and vary chopper frequency. The *R* channel is used because we are interested only in the amplitude of the periodic signal and its phase (see section 2.2) The PIA signal from PhLPPP-L (filled circle) and PhLPPP-H (filled square) as a function of frequency is shown in fig. 6.7(a). The fit (Eq. (6.8)) to the resulting curve is shown with solid line. The triplet lifetime is ~16.5 ms and 10.5ms for PhLPPP-L and PhLPPP-H, respectively. In general, the lifetime of the triplet excitons depend both on the chain length of PhLPPP and the PCBM concentration.

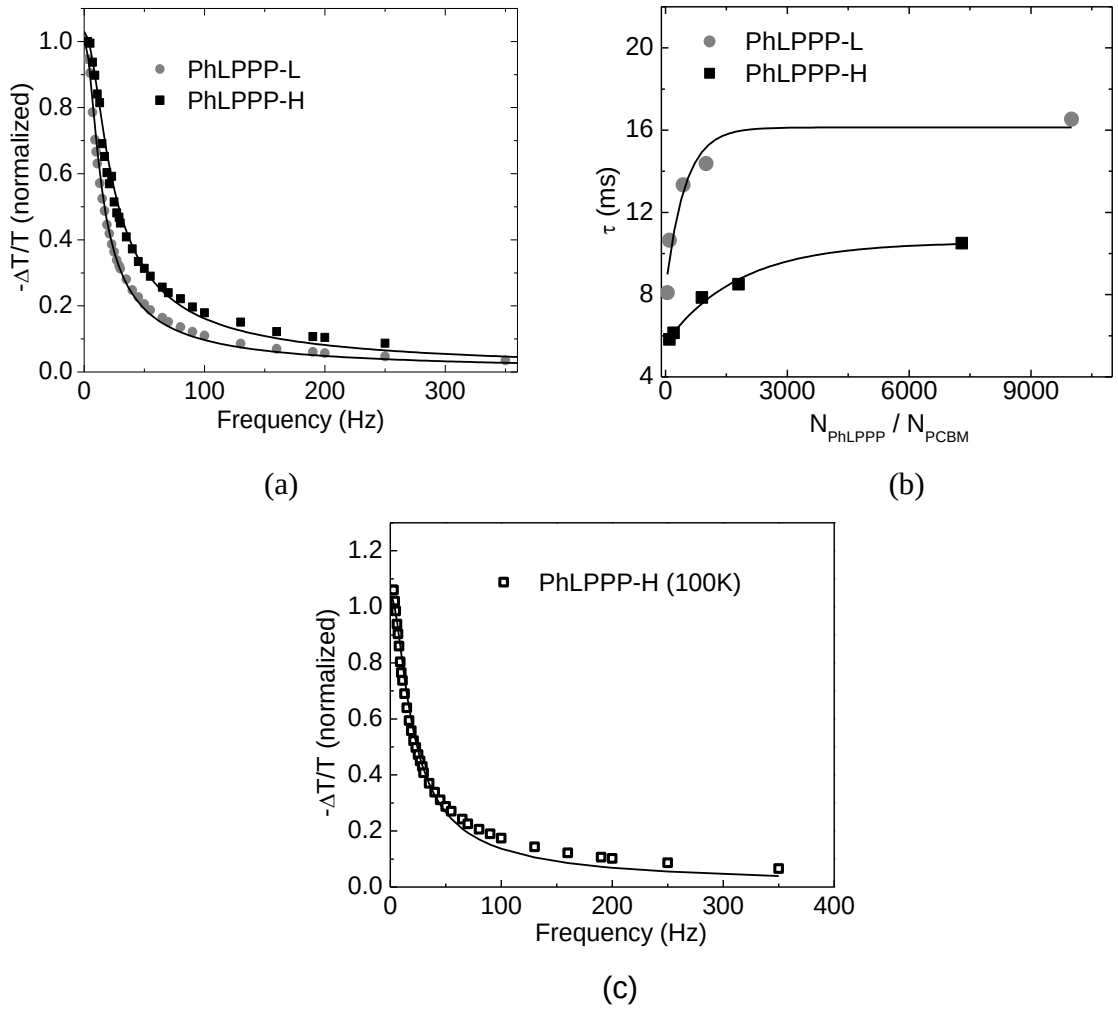

Figure 6.7 (a) The peak PIA signals for T-T transition in PhLPPP-L and PhLPPP-H as a function of the chopper frequency at 300 K. The data are fitted to Eq. (6.8) to obtain triplet lifetime's τ. (b) The variation in τ with PhLPPP:PCBM ratio, which reaches 17 ms and 11 ms asymptotically, the lifetimes for pristine PhLPPP-L and PhLPPP-H samples, respectively.(c) The peak PIA signals for T-T transition in PhLPPP-L and PhLPPP-H as a function of the chopper frequency at 100 K. The data are fitted to Eq. (6.8) to obtain triplet lifetime's τ.

Figure 6.7(b) shows the variation in τ as a function of the PCBM concentration. The asymptotic values ((N_{PhLPPP}/N_{PCBM}) $\rightarrow\infty$) correspond to the lifetimes of the pristine samples, which are found to be (17.0±0.5) ms and (11.0±0.3) ms for PhLPPP-L and PhLPPP-H, respectively. Note that the triplet lifetime in PhLPPP-L (short chain) is longer than PhLPPP-H (long chain). This trend is consistent with the observations in oligo (phenylene vinylene)s, where shorter oligomers have longer triplet lifetimes compared to the longer oligomers.[119] The standard deviations in the lifetime of triplet exciton are obtained by fitting the experimental data in fig. 6.7 to Eq. (6.8). The lifetime, τ, was also measured for PhLPPP-H at 100 K (fig. 6.7(c)), and was found to be (12.0±0.2) ms. At low temperature, the lifetime increases by a small amount.

The various parameters calculated for PhLPPP-L and PhLPPP-H using the PIA spectroscopy is tabulated in Table 6.2. The diffusion lengths at 300 K calculated by the quasi-1D diffusion model and are specified as **L** (PIA at 300K). The lifetimes calculated from PIA data at 300 K are specified as $\boldsymbol{\tau}$ (PIA at 300K). Using $\boldsymbol{\tau}$ (PIA at 300K), the diffusivity calculated by Reufer et al.. in Ref. 105, and Eq. 6.6, the diffusion length is ~ 4.5 µm. Thus, the diffusion length calculated using quasi-1D diffusion model and that calculated using the lifetime is few micrometers. Our diffusion lengths differ from the values of Pt(II) porphyrine complexes in Ref. 106, which may be attributed to the large difference in triplet lifetimes in the two systems: while triplets in PhLPPP have lifetimes of the order of tens of millisecond, the reported triplet lifetimes in PtOEP have values in the microseconds.

Table 6.2 Various PhLPPP excitation triplet properties at temperature of 300K, 100 K or < 200 K. The diffusion length, lifetime, and diffusivity are specified by **L**, **τ**, and **D**, respectively.

	PhLPPP-L	**PhLPPP-H**
L (PIA at 300K)	1.7±0.2 μm	3.9±0.3 μm
τ (PIA at 300K)	17.0±0.5 ms	11.0±0.3 ms
D (PIA at 300K)	$(1.7\pm0.2)\times10^{-6}$ cm^2s^{-1}	$(1.4\pm0.1)\times10^{-5}$ cm^2s^{-1}
D (PIA at 100K)	--	$(3.0\pm0.2)\times10^{-5}$ cm^2s^{-1}
D [a](< 200K)	--	$\sim2\times10^{-5}$ cm^2s^{-1}

[a]Ref. 105

The triplet diffusivities calculated from the diffusion lengths and lifetimes of the pristine samples at 300 K using Eq. (6.6) is specified as **D** (PIA at 300 K). Using PIA spectroscopy, the diffusivities of the triplet excitons in PhLPPP-L and PhLPPP-H are found to be $(1.7\pm0.2)\times10^{-6}$ cm^2s^{-1} and $(1.4\pm0.1)\times10^{-5}$ cm^2s^{-1}, respectively at 300 K, which is consistent with the expectation that excitons would be more readily diffusible in a longer chain molecule than a shorter one, and hence, would have a larger diffusivity. In our experiments, the diffusivity of PhLPPP-H at 100 K (**D** (PIA at 100 K)) was calculated as $(3.0\pm0.2)\times10^{-5}$ cm^2s^{-1}. Reufer *et al.*. observed a temperature independent diffusion for triplet excitons below 200 K in a high molecular weight PhLPPP sample using phosphorescence decay experiments, with the average value of diffusivity ~ $(2.0\pm0.1)\times10^{-5}cm^2s^{-1}$.[105] The value of diffusivity obtained for PhLPPP-H by our studies at 100 K, **D** (PIA at 100K), compares well with the values given in Ref. 105 (**D** [a](< 200K)). The

difference is attributable to the difference in the molecular weights of the sample used in the two studies. The correct order of the diffusivities further supports the quasi-1D model used in this work to obtain the diffusion length.

So far, we have used quasi-1D diffusion model to derive an equation to correlate the quenching data Q with the PhLPPP-PCBM molar ratio R. From the model and PIA spectroscopy, we calculated the diffusion length, lifetime and diffusivity of PhLPPP samples.

In the next section, we will apply random-walk model to derive equation to correlate the quenching data *Q* with the distance between the PCBM monomer *a*. We will recalculate the diffusivities of the high and low molecular weight PhLPPP using the random-walk model.

6.2.3 Random-walk diffusion of excitons

6.2.3.1 Model

Our experimental data are further modeled by a one dimensional random walk since the average distance that an exciton travels on a polymer chain is typically longer than it covers in hopping between chains, unlike in a molecular crystal.[120,121] We consider the diffusion of the triplet excitons to occur as random hops of step size *d* and the hopping time τ_0, which depend on the overlap of molecular orbitals between the two sites involved. Further, we assume that the molecules are sufficiently close together for the intermolecular hopping distances and times to be not significantly different from *d* and τ_0. In order to capture the exciton dynamics, we require that the exciton hopping

time be much less than the exciton lifetime, i.e., $\tau_0 << \tau$, and monomer-monomer distance be less than the distance a between two PCBM molecules, i.e., d<<a.

6.2.3.2 Estimating diffusion length using a random-walk model

Casting the problem at hand as a random-walk problem with an absorbing wall,[122] at the average PCBM distance from the front of the sample as shown in the inset of fig. 6.8, we arrive at the following for the fraction of the exciton generated at x=0 that arrive at x=a during time t and t+dt as,

$$q(a, D_{th}t) = \left(\frac{a}{2\sqrt{\pi D_{th}}} \right) e^{-a^2/4D_{th}t} dt \,, \tag{6.9}$$

where D_{th} is the diffusion constant in the theoretical model. Therefore, if the steady-state population of triplets in the absence of PCBM is P_0, then the population in the presence of PCBM is

$$P = P_0 \left[1 - \int_0^{\tau} q(a,t) dt \right], \tag{6.10}$$

Since the T-T absorption is proportional to the steady state population of triplets, the PIA signal decreases with increasing PCBM concentration according to Eq. (6.9). Clearly, the decrease in T-T absorption is not linear in the concentration of PCBM as would be expected if there were no exciton migration contribution.[123]

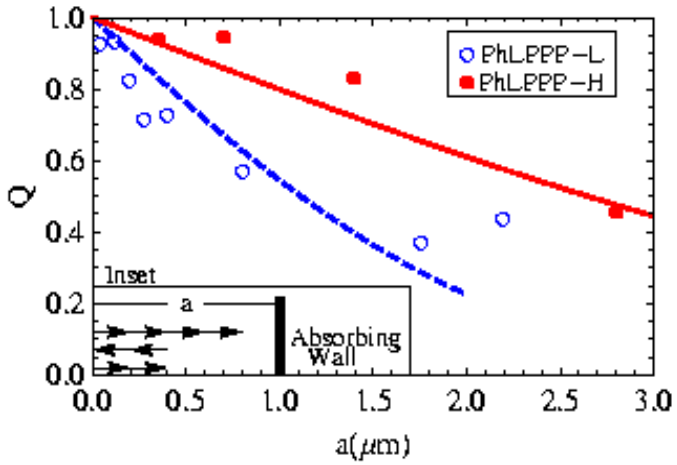

Figure 6.8 Quenching of the T-T transition modeled by a random-walk with an absorbing wall. The open circles and filled squares are the experimental data for the normalized quenching of the T-T transition at 300K in PhLPPP-L and PhLPPP-H, respectively. The dashed and solid lines are the Q_{th} (D_{th},a). The inset shows the schematic of the random-walk model.

The PIA signal of a PhLPPP:PCBM mixture normalized with the PIA signal of the pristine PhLPPP can be written in terms of the theoretical quenching factor Q_{th} which is a function of a and D_{th},

$$Q_{th}(D_{th},a) = 1 - \frac{P}{P_0} = \int_0^{\tau} q(a,D_{th},t)dt \,, \qquad (6.11)$$

where the subscript 0 refers to the pristine PhLPPP sample. To deduce the triplet diffusivity based on Eqs. (6.9)–(6.11), we fit the quenching of PIA data by the theoretical quenching Q_{th} given in Eq. (6.11) as shown in fig. 6.8. The best fit of the data was obtained for $D_{th}=8\times10^{-7}$ cm^2s^{-1} and $D_{th}=8\times10^{-6}$ cm^2s^{-1} for PhLPPP-L and PhLPPP-H,

respectively. The diffusivities calculated using quasi-1D diffusion model i.e. **D** (PIA at 300 K) (Table 6.2) and 1D random-walk model is tabulated in Table 6.3. The theoretical diffusivities are comparable to the experimental values, which lends support to the random-walk diffusion model proposed here for the diffusion of triplet excitons in ladder-type polymers. Also, the diffusivities obtained here for the two samples of PhLPPP are in agreement with the diffusivities of triplet excitons in other systems.[106]

Table 6.3 The diffusivity calculated from quasi-1D diffusion model in section 6.2.2, D (PIA at 300K) and theoretical diffusivity calculated using 1D random-walk model ,D_{th}, .

	PhLPPP-L	**PhLPPP-H**
D (PIA at 300K)	$(1.7\pm0.2)\times10^{-6}$ cm^2s^{-1}	$(1.4\pm0.1)\times10^{-5}$ cm^2s^{-1}
$\mathbf{D_{th}}$ (Random-walk)	8.0×10^{-7} cm^2s^{-1}	8.0×10^{-6} cm^2s^{-1}

6.2.3.3 Discussion

The diffusivity of triplet excitons in PhLPPP, determined by our experiment ranges between 10^{-5}–10^{-6} cm^2s^{-1}. This is close to the diffusivity of triplet excitons reported in a variety of conjugated systems in the literature.[106,124] The approximate micrometer range diffusion length stems from long lifetimes of the triplet excitons in the system under investigation. We have determined the diffusion length/diffusivity of triplet excitons by two methods: directly from the amount of quenching of the T-T absorption in PIA experiment as a function of PCBM concentration, and the other by solving the

problem as a random-walk model using some experimental input. In both cases, the separation of PCBM molecules (a) is evaluated using a quasi-1D diffusion path. Since the experiments are from blended film samples, there is some amount of nonuniformity and additionally, there may be variations as to which area of the film was illuminated. Despite these variations we point out that our value for D (at 100 K) $\sim 3\times 10^{-5}$ cm^2s^{-1} in PhLPPP-H is very close to the value (2×10^{-5} cm^2s^{-1}) measured in Ref. 105 by an alternate method without the use of any acceptor molecules. The agreement between the values of diffusivity of triplet excitons found by two different methods further lends support to the method presented here.

Further, the effective dimension for the diffusion of excitons can be ascertained if we assume that the total volume of the sample may be written as either $N_{PCBM}a^n$ or $N_{PhLPPP}b^n$, where a is the separation between PCBM molecules, b the distance between centers of the PhLPPP polymer chains, and n the spatial dimension. The spatial dimension, n=1 corresponds to a strictly 1D motion. The separation b would be proportional to the π-conjugation length l_p of a PhLPPP polymer chain, i.e., $b=cl_p$, where the proportionality constant c=1 for a tightly packed polymer matrix and c>1 for a sparsely packed system. Assuming a tightly packed structure in the present system, we note that the separation between PCBM molecules may be given as $a=R^{1/n}l_p$, where R stands for the molar ratio N_{PhLPPP}:N_{PCBM} as mentioned above. Using this expression for a in Eq. (6.2) in place of $a=Rl_p$, the value of n could be deduced from the quenching data given in fig. 6.5(b). We find that $n\approx 1$ for PhLPPP-H and $n\approx 1.3$ for PhLPPP-L. These values of spatial dimensions in which the excitons migrate are very near 1, and show that the one-dimensional model

is appropriate for the analysis in the present system. Furthermore, for the low molecular weight sample, since n is not strictly 1, our procedure overestimates the diffusion length. Clearly, diffusion in molecular samples, where the diffusion is more likely three dimensional, one would need a three-dimensional random-walk model to analyze the results. Note that, in the formula for a, the factor c multiplies l_p, which essentially extends the distance an exciton travels between PCBM molecules. Therefore, if the system is not tightly packed, i.e., when $c>1$, then the same level of quenching would result in a larger value of the diffusion length, assuming dissipation of energy during hops is unaffected by an increase in the hopping distance. Furthermore, although the theoretical one-dimensional model is strictly applicable to systems with large π-conjugation lengths compared to the hopping distance between molecules, the experimental procedure given here should be more generally applicable as long as we express the inter-PCBM distance a in terms of n and deduce n from experiment as outlined here. Even with an uncertainty in the value of c, the determination of the triplet exciton diffusion length could be achieved by the PIA quenching method which would be accurate within the margin of uncertainty of the factor by which distance between PhLPPP molecules differs from the π-conjugation length of the molecule.

In our studies, we have also assumed that PCBM molecules are very effective in quenching the triplet excitons, which is based on the observation that in a 1:1 molar ratio of PhLPPP:PCBM the PIA signal is completely quenched. Note that, if the efficiency of quenching by PCBM molecules were not 100%, then it would require multiple encounters with PCBM molecules for the energy in the exciton to dissipate. Thus, a lower

efficiency of quenching would yield even larger value of the diffusion length. Since our results from quenching experiments agree well with those of Reufer et al.. [105] using phosphorescence, we believe that the assumption of high quenching efficiency by PCBM molecules is justified in the final analysis.

6.3 Summary

In summary, we present a simple experimental technique in conjunction with a random-walk model for determining triplet exciton diffusion lengths in organic semiconductors. This relies on the quenching of the T-T absorption in the presence of acceptor molecules. Since this method is based on the T-T absorption rather than phosphorescence, it may be applied to even non triplet enhanced conjugated polymers, with a caveat that the experiments may have to be performed at lower temperatures as the T-T absorption signal in general may be weak at RT. The use of a Pd-incorporated ladder-type polymer in this work facilitated the PIA measurements at RT. The triplet diffusion lengths determined in the ladder-type polymer, PhLPPP, depend on the length of the π-conjugated system and are in the 1–4 μm range at 300 K. The long diffusion lengths of the triplet excitons compared to singlet excitons, which are typically in the nanometer range, open up a new realm of application of triplet-enhanced conjugated polymers in energy harvesting optoelectronics.

7.

SUMMARY AND FUTURE DIRECTION

In this thesis, we presented photocurrent and optical spectroscopic studies on amorphous organic semiconductors with a keen focus of their applications in OPVs. The cost effective fabrication technique, flexibility of devices and possibility of large-area printing, makes organic semiconductors a highly researched topic for commercial application. The research work presented here, adds to further understanding of various excitonic states of organic semiconductors for their application in OPVs.

The work presented here can be split into two parts: first, to the study of CT excitons, and second, to the studies of triplet excitons. Both the CT and triplet excitons are known to contribute to photocurrent generation and impact the efficiency of an organic solar cell.

To probe CT states, we choose low-bandgap DPP-based copolymers, including two DPP-based statistical copolymers (PDPP-BBT, TDPP-BBT, Poly A (low DPP fraction) and Poly B (high DPP fraction)). The variations of donor-acceptor unit fraction in these copolymers offer a means of gradual tuning of the optical bandgap. The solid state absorption spectra of all the copolymers showed the presence of two bands. The low energy band was attributed to the intra CT exciton. The intra CT states in TDPP-BBT, Poly A, Poly B and its fullerene blends were analyzed using bias dependent absorption studies. The pristine TDPP-BBT sample, Poly B as well as their blends showed no changes in the absorption on applying external bias (0 to -10V). Although the pristine Poly A sample did not show any bias-dependent shifts/changes, Poly A:fullerene blend

showed a redshift in the absorption spectrum with increasing negative bias. This was found to be an indication of quantum confinement at the Poly A/fullerene interface and gave an estimate of the *BE* (~0.143 eV) of the intra CT exciton in Poly A.

To gain theoretical insights into the origin of the intra CT states, we performed DFT and TDDFT on the monomers of DPP-based statistical copolymers. The DFT (and TDDFT) calculations were performed using the Gaussian 09 package. The DFT calculations provided us with the information of the spatial extent of MOs in a monomer unit. Further, we implemented TDDFT to calculate the absorptivity and the origin of intra CT state in the absorptivity. The TDDFT calculations correctly predicted the bandgap of Poly B monomer than in the Poly A monomer. The strength of the state-to-state excitations was correlated with the higher intra CT character of the lowest singlet state.

In addition to the intra CT states, the inter CT states formed at the donor copolymer/fullerene interface were also probed using photocurrent modulation techniques. Two photocurrent techniques: monochromatic PC and the FTPS, were assembled to identify the inter CT states in DPP-based copolymer:fullerene blends in OPVs. The PC measured from two of the devices: PDPP-BBT:fullerene and Poly A:fullerene, showed a low energy PC onset compared to the onset of absorption in the corresponding blends. This was the indication of a stabilized inter CT state. No such low-energy onset (inter CT state) was detected in other copolymer:fullerene blends. It was inferred that the inter CT state was stabilized (and observed) when the singlet bandgap energy difference between the DPP polymer and fullerene was small ($\leq$ 0.3 eV). When the bandgap difference between the DPP copolymer and fullerene was large ($\geq$ 0.3 eV),

the PC (monochromatic PC and FTPS PC) from the blended films showed no low energy edge. The implication of this result is that (i) the inter CT state coincided with the absorption edge or (ii) the inter CT state was not stabilized at all. If option (i) were true, there would be a possibility of back charge transfer and lowering of device performance. However, devices in which no inter CT states were stabilized had a higher overall responsivity. This suggests that the inter CT state in such devices dissociates faster than the time scale of our PC experiments. The absence of the inter CT states therefore helped in a higher responsivity/EQE. An immediate implication of this result is to look for a combination of donor (e.g. P3HT) and acceptor material (other than fullerene), such that the bandgap difference between the donor and acceptor is less than 0.3 eV. If a small bandgap difference between P3HT and some other acceptor leads to an unstabilized inter CT states, it is conceivable that higher efficiency P3HT-based solar cell solar cells may exits.

To probe triplet states, we had chosen ladder-type homopolymer (PhLPPP). PhLPPP has a trace concentration (~150-200 ppm) of Pd atom which enhances the ISC for decay of the singlet excitons to triplet excitons. This allows us to probe T-T absorption even at room temperature. We setup an optical modulation spectroscopy (pump-probe) technique and utilize PIA spectroscopy to identify the T-T absorption in PhLPPP. To understand the dynamics of the triplet exciton detected, we estimate the diffusion length/diffusivities of the triplet exciton by tracking the T-T quenching as a function of the PhLPP:PCBM molar ratio (quasi-1D diffusion model) and the distance between PCBM chromophore (1D random-walk model). The diffusion lengths and diffusivities of

triplet exciton are calculated to be almost three orders of magnitude more than the singlet excitons. We also measured the lifetime of triplet exciton by tracking the PIA signal as a function of the chopper frequency. The triplet lifetimes are found to be of the order of millisecond. Considering the higher diffusivities and diffusion length of triplets, one should look for device geometries which would not be limited by the necessity of having only nanoscale phase segregation for singlet exciton diffusion.

The above studies were also extended for PhLPPP under high pressure by K. Paudel et al. in our group.[125] The electroluminescence (EL) spectra for the PhLPPP was found to span the UV-Vis and the NIR region (1.7-2.7 eV). It also showed a very strong feature at ~2.1 eV which coincided with the phosphorescence studies at high pressure. Since phosphorescence corresponds to emission from triplet to the singlet ground state, it implies that the presence of triplet states enhances the EL (and phosphorescence). The enhanced emission at low energy finds its application in low-energy phosphorescent light-emitting diode. Note that the broad EL spectrum corresponds to a white-light emitting diode.

The above mentioned PC spectroscopic studies were mostly performed at room temperature. In Chapter 5, temperature dependent PC studies on P3HT:PCBM were performed to elucidate the dynamics of the inter CT state. Similar studies were done on Poly A:PCBM and Poly B:PCBM devices, the result of which are presented in figure 7.1. Figure 7.1 (a) (and (b)) show the semi-logarithmic plots of the normalized monochromatic PC measured in Poly A:PCBM (and Poly B:PCBM) devices at three different temperatures: 200 K, RT, and 390 K. In contrast to the temperature-independent

behavior of the onset of PC in P3HT:PCBM graph (fig. 3.5 (b)), a significant change in the onset of PC is seen in Poly A:PCBM devices. Note that Poly A:PCBM samples had shown a stabilized inter CT state (section 4.3.3). In Poly B:PCBM sample (fig. 7.1(b)), the temperature seems to have almost no effect on the onset of the PC. This signature is similar to the one observed in P3HT:PCBM (fig. 3.5 (b)). By performing an in-depth temperature dependent study of these samples (below 290 K) one should check for an Arrhenius type dependence in Poly A:PCBM and Poly B:PCBM devices. The activation energy value from the Arrhenius-type plots may give an indication of diffusion properties of the excitonic states.

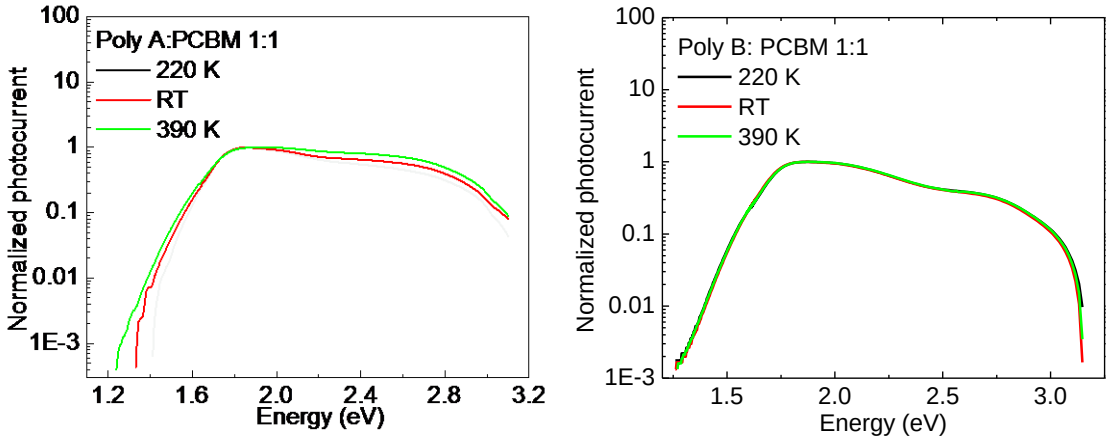

Figure 7.1 The normalized photocurrent as a function of temperature in (a) Poly A:PCBM (b) Poly B:PCBM devices.

Similar studies can also be extended to identify the effect of temperature on the intra CT in DPP-based copolymer or statistical copolymers. Note that the bias dependent studies on Poly A, Poly B and their fullerene blends had shown different behavior

(section 4.2). No bias dependent changes were seen in Poly A, Poly B and Poly B:PCBM, but an intra exciton confinement was seen at the Poly A/PCBM surface. The temperature dependent studies of intra CT nature might shed light on the diffusion properties of intra CT states in the DPP-based and other donor-acceptor copolymers. Additionally, time-resolved spectroscopy could also be used to resolve the decay process of the intra excitonic state. The time-dependent studies, in presence PCBM, will further help in addressing the issue of how the lifetime of intra CT exciton affects the formation of inter CT exciton.

REFERENCES

1. G. Inzelt, Conducting Polymers: A new era in electrochemistry (Spencer, 2008), Chapter 1: Introduction, p.1-3.

2. C. K. Chiang, C. R. Fincher, Jr., Y. W. Park, A. J. Heeger, H. Shirakawa, E. J. Louis, S. C. Gau, and A. G. MacDiarmid, "Electrical Conductivity in Doped Polyacetylene", Phys. Rev. Lett., **37**, 1098-1101 (1977)

3. A. Pochettino, Acad. Lincei Rend., **15**, 355 (1906).

4. M. Volmer, Ann. Physik, **40**, 775 (1913).

5. M. Pope and C. E. Swenberg, Electronic Process in organic crystals and polymers (Oxford University Press, 1999).

6. M. Chandrasekhar, S. Guha, and W. Graupner, "Squeezing organic conjugated molecules – What does one learn?", Adv. Mater., **13**(8), 613-618 (2001).

7. U. Scherf, "Ladder-type materials", J. Mater. Chem., **9**, 1853-1864 (1999).

8. T. A. Skotheim, R. L. Elsenbaumer and J. R. Reynolds, Handbook of conducting polymers (Marcel Dekker, Inc., New York, 1998), 2nd ed., Chap III, p.363.

9. National Renewable Energy Laboratory, http://rredc.nrel.gov/solar/spectra/am1.5/S.

10. E. Bundgard, F. C.Kerbs, "Low band gap polymer for organic photovoltaics", Solar Energy Materials & Solar Cells, **91**, 954-985 (2007).

11. M. Pope and C. E. Swenberg, Electronic Process in organic crystals and polymers (Oxford University Press, 1999).

12. M. Svensson, F. Zhang, S. C. Veenstra, W. J .H. Verhees, J. C. Hummelen, J. M. Kroon, O. Inganäs, and M. R. Andersson, "High-performance polymer solar cells of an alternating polyflourene copolymer and a fullerene derivative", Adv. Mater., **12**, 988-991 (2003).

13. N. Blouin, A. Michaud, and M. Leclerc, "A low-bandgap poly(2,7-carbazole) derivative for use in high performance solar cell", Adv. Mater., **19**, 2295-2300 (2007).

14. H. M. P. Wong, P. Weng, A. Abrusci, M. Svensson, M. R. Andersson, and N. C. Greenham, "Donor and Acceptor Behavior in a Polyfluorene for Photovoltaics", J. Phys. Chem., **111**, 5244-5249 (2007).

15. W. Mammo, S. Admassie, A. Gadis, F. Zhang, O. Inganäs, and M.R. Andersson, "New low band gap alternating polyfluorene copolymer-based photovoltaic cells", Solar Energy Materials & Solar Cells, **91**, 1010-1018 (2007).

16. S. H. Park, A. Roy, S. Beaupre, S. Cho, N. Coates, J. S. Moon, D. Moses, M. Leclerc, K. Lee, and A. J. Heeger, "Bulk heterojunction solar cells with internal quantum efficiency approaching 100%", Nature Photonics, **3**, 297-303 (2009).

17. Y. Zhu, A. R. Rabindranath, T. Beyerlein, B. Tieke, "Highly Luminescent 1,4-Diketo-3,6-diphenylpyrrolo[3,4-c]pyrrole-(DPP-) Based Conjugated Polymers Prepared Upon Suzuki Coupling", Macromolecules, **40**, 6981-6989 (2007).

18. J. C.Bijleveld, A. P. Zoombelt, S. J. G. Mathijssen, M. M.Wienk, M. Turbiez, D. M. de Leeuw, R. A. J. Janssen, "Poly(diketopyrrolopyrrole-terthiophene) for Ambipolar Logic and Photovoltaics", J. Am. Chem. Soc., **1131**, 16616-16617 (2009).

19. M. -F. Falzon, A. P. Zoombelt, M. M. Wienk and R. A. J. Janssen, "Diketopyrrolopyrrole-based acceptor polymers for photovoltaic application", Phys. Chem. Chem. Phys., **13**, 8931–8939 (2011).

20. D. Adil, C. Kanimozhi, N. B. Ukah, K. Paudel, S. Patil, and S. Guha, "Surface-enhanced raman spectroscopic studies of metal semiconductor interfaces in organic field-effect transistors", ACS Appl. Mater. Interfaces, **3**, 1463-1471 (2011).

21. C. Kanimozhi, N. Y-Gross, K. W. Chou, A. Amassian, T. D. Anthopoulos, and S. Patil, "Diketopyrrolopyrrole−diketopyrrolopyrrole-based conjugated copolymer for high-mobility organic field-effect transistors" J. Am. Chem. Soc., **134**, 16532-16535 (2012)

22. A. P. Zoombelt, S. G. J. Mathijssen, M. G. R. Turbiez, M. M. Wienk, and R. A. J. Janssen, "Small band gap polymers based on diketopyrrolopyrrole", J. Mater. Chem., **20**, 2240-2246 (2010).

23. W. Li, K. H. Hendriks, W. S. C. Roelofs, Y. Kim, M. M. Wienk, and R. A. J. Janssen, "Efficient small bandgap polymer solar cells with high fill factor for 300 nm thick films", Adv. Mater., **25**, 3182–3186 (2013).

24. Y. Qiao, Y. Guo, C. Yu, F. Zhang, W. Xu, Y. Liu, and D. Zhu, "Diketopyrrolopyrrole-containing quinoidal small molecules for high-performance, air-stable, and solution-processable n-channel organic field-effect transistors", J. Am. Chem. Soc., **134**, 4084−4087 (2012).

25. J. Hollinger, J. Sun, D. Gao, D. Karl, and D. S. Seferos, "Statistical Conjugated Polymers Comprising optoelectronically distinct units", Macromol. Rapid Commun., **34**, 437-441 (2013).

26. H. N. Cho, J. K. Kim, D. Y. Kim, N. W. Song, D. Kim and C.Y. Kim, "Statistical Copolymers for Blue-Light-Emitting Diodes", Macromolecules, **32**, 1476-1481 (1999).

27. P. -T. Wu, G. Ren, and S. A. Jenekhe, "Crystalline Random Conjugated Copolymers with Multiple Side Chains: Tunable Intermolecular Interactions and Enhanced Charge Transport and Photovoltaic Properties", Macromolecule, **43**, 3306-3313 (2010).

28. D. Moghe, G. K. Dutta, S. Patil, and S. Guha, "Photocurrent spectroscopic studies of diketopyrrolopyrrole-based statistical copolymers", Phys. Chem. Chem. Phys., **16**, 4291-4298 (2014).

29. J. C. Hummelen, B. W. Knight, F. LePeq, and F. Wudl, J. Yao and C. L. Wilkins, "Preparation and Characterization of Fulleroid and Methanofullerene Derivatives", J. Org. Chem., **60**, 532-538 (1995).

30. V. D. Mihailetchi, J. K. J. van Duren, P. W. M. Blom, J. C. Hummelen, R. A. J. Janssen, J. M. Kroon, M. T. Rispens, W. J. H. Verhess, and M. M. Wienk, "Electron transport in methanofullerene", Adv. Funct. Mater, **13**(1), 43-46 (2003).

31. W. Ma, C. Yang, X. Gong, K. Lee, and A. J. Heeger, "Thermally stable, efficient polymer solar cell with nanoscale control of the interpenetrating network morphology", Adv. Funct. Mater., **15**, 1617-1622 (2005).

32. X. Yang, J. Loos, S. C. Veenstra, W J. H. Verhees, M. M. Wienk, J. M. Kroon, M. A. J. Michels, and R. A. J. Janssen, "Nanoscale morphology of high-performance polymer solar cells", Nano Lett., **5**(4), 573-589 (2005).

33. B. Walker, A. B. Tamayo, X. D. Dang, P. Zalar, J. H. Seo, A. Garcia, M. Tantiwiwat, T. Q. Nguyen, "Nanoscale Phase separation and high photovoltaic efficiency in solution-processed, small-molecule bulk heterojunction solar cells, Adv. Funct. Mater., **19**, 3063-3069 (2009).

34. W. Kylberg, P. Sonar, J. Heier, J.-N. Tisserant, C. Muller, F. Nuesch, Z. –K. Chen, A. Dodabalapur, S. Yoon and R. Hany, "Synthesis, thin-film morphology, and comparative study of bulk and bilayer heterojunction organic photovoltaic devices using soluble diketopyrrolopyrrole molecules", Energy Environ. Sci., **4**, 3617-3624 (2011).

35. M. Cardona, Modulation spectroscopy (Academic Press, New York and London, 1969).

36. M. Vanecek and A. Poruba, "Fourier-transform photocurrent spectroscopy of microcrystalline silicon for solar cells", Appl. Phys. Lett., **80**, 719-721 (2002).

37. K. Vandewal, L. Goris, I. Haeldermans, M. Nesladek, K. Haenen, P. Wagner, and J. V. Manca, "Fourier-transform photocurrent spectroscopy for a fast and highly sensitive spectral characterization of organic and hybrid solar cell", Thin Solid Films, **516**, 7135 (2008).

38. L. Goris, A. Poruba, L. Hod'akova, M. Vanecek, K. Haenen, M. Nesladek, P. Wagner, D. Vanderzande, L. De Schepper, and J. V. Manca, "Observation of the subgap optical absorption in polymer-fullerene blend solar cells", Appl. Phys. Lett., **88**, 0521131- 0521133 (2006).

39. K. Vandewal, A. Gadisa, W. D. Oosterbaan, S. Bertho, F. Banishoeib, I. V. Severen, L. Lutsen, T. J. Cleij, D. Vanderzande, and J. V. Manca, "The relation between open-circuit voltage and the onset of photocurrent generation by charge-transfer absorption in polymer: fullerene bulk heterojunction solar cell", Adv. Funct. Mater., **18**, 2064-2070 (2008).

40. G. Li, R. Zhu, and Y. Yang, "Polymer solar cells", Nature Photonics, **6**, 153-161 (2012).

41. A. J. Heeger, "25th anniversary article: Bulk heterojunction solar cells: Understanding the mechanism of operation", Adv. Mater, **26**, 10-28 (2014)

42. M. C.-Quiles, T. Ferenczi, T. Agostinelli, P. G. Etchegoin, Y. Kim, T. D. Anthopoulos, P. N. Stavrinou, D. D. C. Bradley, and J. Nelson, "Morphology evolution via self-organization and lateral and vertical diffusion in polymer:fullerene solar cell blends", Nature Mater., **7**, 158-164 (2008).

43. W. Ma, C. Yang, X. Gong, K. Lee, and A.J. Heeger, "Thermally efficient polymer solar cells with nanoscale control of the interpenetrating network morphology", Adv. Funct. Mater., **15**, 1617-1622 (2005).

44. S. Günes, H. Neugebauer, and N. S. Sariciftci, "Conjugated polymer-based organic solar cells", Chem. Rev., **107**, 1324-1338 (2007).

45. J. M. Lupton, A. Pogantsch, T. Piok, E. J. W. List, S. Patil, and U. Scherf, "Intrinsic room-temperature electrophosphorescence from a π-conjugated polymer", Phys. Rev. Lett., **89**, 1674011-1674014 (2002).

46. M. T. Dang, L. Hirsch, and G. Wantz, "P3HT:PCBM, best seller in polymer photovoltaic research", Adv. Mater., **23**, 3597-3602 (2011).

47. C. Deibel, T. Strobel, and V. Dyakonov, "Role of the charge-transfer state in organic donor-acceptor solar cell", Adv. Mater., **22**, 4097-4111 (2010).

48. J. J. Benson-Smith, L. Goris, K. Vandewal, K. Haenen, J. V. Manca, D. Vanderzande, D. D. C. Bradley, and J. Nelson, "Formation of a ground-state charge-transfer complex in polyfluorene/[6,6]-phenyl-C61 butyric acid methyl ester (PCBM) blend films and its role in the function of polymer/PCBM solar cells", Adv. Funct. Mater., **17**, 451-457 (2007).

49. T. Drori, C.-X. Sheng, A. Ndobe, S. Singh, and Z. V. Vardeny, Optical studies of the charge transfer complex in polythiophene/fullerene blends for organic photovoltaic applications", Phys. Rev. Lett., **101**, 0374011-0374014 (2008).

50. T. Drori, J. Holt, and Z. V. Vardeny, "Below-Gap excitation of π-Conjugated polymer-fullerene blends: Implications for bulk organic heterojunction solar cells", Phys. Rev. B, **82**, 0752071-0752078 (2010).

51. J. J. M. Halls, J. Cornil, D. A. dos Santos, R. Silbey, D.-H. Hwang, A. B. Holmes, J. L. Bre´das, and R. H. Friend, "Charge- and energy-transfer processes at polymer/polymer interfaces: A joint experimental and theoretical study", Phys. Rev. B, **60**, 5721-5727 (1999).

52. J. Mizuguchi, "Correlation between crystal and electronic structures in diketopyrrolopyrrole pigments as viewed from exciton coupling effects", J. Phys. Chem. A, **104**, 1817-1821 (2000)

53. P. J. Brown, D. S. Thomas, A. Kohler, S. Wilson, J. -S. Kim, C. M. Ramsdale, H. Sirringhaus, and R. Friend, "Effect of interchain interaction on the absorption and emission of poly(3-hexylthiophene)", Phys. Rev. B, **67**, 0642031-06420316 (2003).

54. D. Muhlbacher, M. Scharber, M. Morana, Z. Zhu, D. Walker, R. Gaudiana, and C. Brabec, "High photovoltaic performance of a low-bandgap polymer", Adv. Mater., **18**, 2884-2889 (2006).

55. D. Veldman, S. C. J. Meskers, and R. J. Janssen, "The energy of charge-transfer states in electron donor-acceptor blends: Insights into the energy losses in organic solar cells", Adv. Funct. Mater., **19**, 1939-1948 (2009).

56.V. Shrotriya, J. Ouyang, R. J. Tseng, G. Li, Y. Yang, "Absorption spectra modification in poly(3-hexylthiophene):methanofullerene blend thin films", Chem. Phys. Lett., **411,** 138–143 (2005).

57. K. Vandewal, W. D. Oosterbaan, S. Bertho, V. Vrindts, A. Gadisa, L. Lutsen, D. Vanderzande, and J. V. Manca, "Varying polymer crystallinity in nanofiber poly(3-alkylthiophen): PCBM solar cells: Influence on charge-transfer state energy and open-circuit voltage", Appl. Phys. Lett., **95**, 1233031-1233033 (2009).

58. M. A. Loi, S. Toffanin, M. Muccini, M. Forster, U. Scherf, and M. Scharber, "Charge transfer excitons in bulk heterojunction of a polyfluorene copolymer and a fullerene derivative", Adv. Funct. Mater., **17**, 2111-2116 (2007).

59. F. C. Jamieson, T. Agostinelli, H. Azimi, J. Nelson, and J. R. Durrant, "Field-Independent Charge Photogeneration in PCPDTBT/PC70BM Solar Cells", J. Phys. Chem. Lett., **1**, 3306–3310 (2010).

60. C. Piligeo and M. A. Loi, J. Mater., "Charge transfer state in highly efficient polymer–fullerene bulk heterojunction solar cells", Chem., **22**, 4141-4150 (2012).

61. J. Lee, K. Vandewal, S. R. Yost, M. E. Bahlke, L. Goris, M. A. Baldo, J. V. Manca, and T. V. Voorhis, "Charge transfer state versus hot exciton dissociation in polymer-fullerene blended solar cells", J. Am. Chem. Soc., **132,** 11878–11880 (2010).

62. D. Veldman, Ö. Ipek, S. C. J. Meskers, J. Sweelssen, M. M. Koetse, S. C. Veenstra, J. M. Kron, S. S. van Bavel, J. Loos, and R. A. J. Janssen, "Compositional and Electric Field Dependence of the Dissociation of Charge Transfer excitons in alternating polyfluorene copolymer/fullerene blends", J. Am. Chem. Soc., **130**, 7721-7735 (2008).

63. S. De, T. Pascher, M. Maiti, K. G. Jespersen, T. Kesti, F. Zhang, O. Inganäsand, A. Yartsev, V. Sundström, "Geminate charge recombination in alternating polyfluorene copolymer/fullerene blends", J. Am. Chem. Soc., **129**, 8466-8472 (2007).

64. P. K. Watkins, A. B. Walker, and G. L. B. Verschoor, "Dynamical Monte Carlo modelling of organic solar cells: The dependence of internal quantum efficiency on morphology", Nano Lett., **5**, 1814-1818 (2005).

65. C. Groves, R. A. Marsh, and N. C. Greenham, "Monte Carlo modeling of geminate recombination in polymer-polymer photovoltaic devices", J. Chem. Phys., **129**, 114903-1149037 (2008).

66. A. A. Bakulin, A. Rao, V. G. Pavelyev, P. H. M. van Loosdrecht, M. S. Pshenichnikov, D. Niedzialek, J. Cornil, D. Beljonne, and R. H. Friend, "The role of driving energy and delocalized states for charge separation in organic semiconductors", Science, **335**, 1340-1344 (2012).

67. S. Yamamoto, H. Ohkita, H. Benten, and S. Ito, "Role of interfacial charge transfer state in charge generation and recombination in low-bandgap polymer solar cell", J. Phys. Chem. C, **116**, 14804−14810 (2012).

68. D. Moghe, P. Yu, C. Kanimozhi, S. Patil, S. Guha, "Charge transfer complex states in diketopyrrolopyrrole polymers and fullerene blends: Implications for organic solar cell efficiency", Appl. Phys. Lett., **99**, 2333071- 2333073 (2011).

69. D. Moses, J. Wang, G. Yu, and A. J. Heeger, "Temperature-independent photoconductivity in thin films of semiconducting polymers: Photocarrier sweep-out prior to deep trapping", Phys. Rev. Lett., **80**, 2685-2688 (1998).

70. E. Katz, D. Faiman, S. M. Tuladhar, J. M. Kroon, M. M. Weink, T. Fromherz, F. Padinger, C. J. Brabec, N. S. Sariciftsi, "Temperature dependence for the photovoltaic device parameters of polymer-fullerene solar cells under operating conditions", J. Appl. Phys., **90**, 5343-5350 (2001).

71. I. Riedel, and V. Dyakonov, "Influence of electronic transport properties of polymer-fulleren blends on the performance of bulk heterojunction photovoltaic devices", Phys. Stat. Sol. (a), **201**(6), 1332-1341 (2004).

72. D. Jarzab, F. Cordella, J. Gao, M. Schaber, H. –J. Egelhaaf, and M. A. Loi, "Low-temperature behavior of charge transfer excitons in narrow-bandgap polymer-based bulk heterojunction", Adv. Energy Mater., **1**, 604-609 (2011).

73. M. G. Harrison, J. Gruner, G. C. W. Spencer, "Analysis of the photocurrent action spectra of MEH-PPV polymer photodiodes", Phys. Rev. B, **55**(12), 7831-7849 (1997).

74. I. Riedal, J. Parisi, V. Dyakonov, L. Lutsen, D. Vanderzande, and J. C. Hummelen, "Effect of temperature and illumination on the electrical characteristics of polymer-fullerene bulk-heterojunction solar cells", Adv. Funct. Mater., **14**, 38-44 (2004).

75. M. Gailberger and H. Bassler, “dc and transient photoconductivity of poly(2-phenyl-1, 4-phenylenevinylene)”, Phys. Rev. B, **44**(16), 8643-8651 (1991).

76. W. J. Grzegorczyk, T. J. Savenije, T. E. Dykstra, J. Piris, J. M. Schins, and L. D. A. Siebbeles, “Temperature-independent charge carrier photogeneration in P3HT-PCBM blends with different morphology”, J. Phys. Chem. C, **114**, 5182–5186 (2010).

77. P. M. Beaujuge, C. M. Amb, and J. R. Reynolds, “Spectral engineering in π-conjugated polymers with intramolecular donor-acceptor interactions”, Acc. Chem. Res., **43**, 1396-1407 (2010).

78. A. Menon, H. Dong, Z. I. Niazimbetova, L. J. Rothberg, and M. E. Galvin, “Polydispersity effects on conjugated polymer light-emitting diodes”, Chem. Mater., **14**, 3668-3675 (2002).

79. Y. T. Chang, S. L. Hsu, G. Y. Chen, M. H. Su, T. A. Singh, E. W. G. Diau, and K. H. Wei, “Intramolecular donor-acceptor regioregular poly(3-hexylthiophene)s presenting octylphenanthrenyl-imidazole moieties exhibit enhanced charge transfer for heterojunction solar cell applications”, Adv. Funct. Mater., **18**, 2356-2365 (2008).

80. D. Haarer, M. R. Philpott, and H. Morawitz, “Field induced charge-transfer exciton transitions”, J. Chem. Phys., **63**(12), 5238-5245 (1975).

81. D. A. B. Miller, D. S. Chemla, T. C. Damen, A. C. Gossard, W. Wiegmann, T. H. Wood, and C. A. Burrus, “Electric field dependence of optical absorption near the band gap of quantum-well structures”, Phys. Rev. B, **32**, 1043-1060 (1985).

82. F. F. So and S. R. Forrest, “Evidence of exciton confinement in crystalline organic multiple quantum wells”, Phys. Rev. Lett, **66**, 2649-2652 (1991).

83. S. P. McGinnis, B. Das, and M. Dobrowolska, “The effect of electric field on the photoluminescence and absorption spectra of porous silicon”, Thin Solid Films, **365**, 1-4 (2000).

84. C. Schwarz, H. Bässler, I. Bauer, J.-M. Koenen, E. Preis, U. Scherf, and A. Köhler, “Does conjugation help exciton dissociation? A study on poly(p-phenylenes)s in planar heterojunctions with C60 and TNF”, Adv. Mater., **24**, 922-925 (2012).

85. Z. Sun and S. Stafström, “Dynamics of exciton dissociation in donor-acceptor polymer heterojunctions”, J. Chem. Phys., **138**, 1649051- 1649058 (2013).

86. C. Kanimozhi, P. Balraju, G.D. Sharma, and S. Patil, "Synthesis of diketopyrrolopyrrole containing copolymers: A study of their optical and photovoltaic properties", J. Phys. Chem. B, **114**, 3095-3105 (2010).

87. K. Vandewal, Z. Ma , J. Bergqvist , Z. Tang , E. Wang , P. Henriksson , K. Tvingstedt , M. R. Andersson , Fengling Zhang , and Olle Inganäs, "Quantification of quantum efficiency and energy losses in low bandgap polymer:fullerene solar cells with high open-circuit voltage", Adv. Funct. Mater., **22**, 3480–3490 (2012).

88. Y. W. Soon, T. M. Clarke, W. Zhang, T. Agostinelli, J. Kirkpatrick, C. D. Smith, I. McCulloch, J. Nelson, and J. R. Durrant, "Energy versus electron transfer in organic solar cells: a comparison of the photophysics of two indenofluorene: fullerene blend films", Chem. Sci., **2**,1111-1120 (2011).

89. C. A. Ullrich, "Time-Dependent Density-Functional Theory: Concepts and Applications" (Oxford University Press, 2012).

90. E. Runge and E. K. U. Gross, "Density-functional theory for time-dependent systems", Phys. Rev. Lett., **52**, 997-1000 (1984).

91. S. Grimme, "Calculations of the electronic spectra of large molecules" in Reviews of Computational Chemistry, ed. K. B. Lipkowitz, R. Larter, and T.R. Cundari, Wiley-VCH, Hoboken, New Jersey, 2004, vol. 20, pp. 153.

92. P. Elliott, K. Burke, and F. Furche, "Excited states from time-dependent density functional theory", In Reviews in Computational Chemistry, ed. by K. B. Lipkowitz and T. R. Cundari, Wiley, Hoboken 2009, Vol. 26, pp. 91-165.

93. C. Ullrich and Z.-H. Yang, "A brief compendium of time-dependent density functional theory", Braz. J. Phys., **44,** 154-188 (2014).

94. M.E. Casida, In Recent advances in density functional theory, ed. by D. P. Chong, In Recent advances in computational chemistry, World Scientific, Singapore, 1995 Vol 1, pp 155-192.

95. Y. Zhao and D. G. Truhlar, "Density functional for spectroscopy: No long-range self-interaction error, good performance for Rydberg and charge-transfer states, and better performance on average than B3LYP for ground states", J. Phys. Chem., A**, 110**, 13126-13130 (2006).

96. H. Iikura, T. Tsuneda, T. Yanai, and K. Hirao, "A long-range correction scheme for generalized-gradient-approximation exchange functionals" J. Chem. Phys., **115**, 3540-3544 (2001).

97. T. Yanai, D. P. Tew, and N. C. Handy, "A new hybrid exchange–correlation functional using the Coulomb-attenuating method (CAM-B3LYP)", Chem. Phys. Lett., **393**, 51-57 (2004).

98. L. Pandey, C. Doiron, J. S. Sears, and J.-L. Brédas, "Lowest excited states and optical absorption spectra of donor–acceptor copolymers for organic photovoltaics: a new picture emerging from tuned long-range corrected density functionals", Phys. Chem. Chem. Phys., **14**, 14243-14248 (2012).

99. R. Kobayashi, R. D. Amos, "The application of CAM-B3LYP to the charge-transfer band problem of the zincbacteriochlorin–bacteriochlorin complex", Chem. Phys. Lett., **420**, 106–109 (2006).

100. GAUSSIAN09, Gaussian, Inc., Pittsburgh, PA, 2009.

101. D. Adil, Ph.D. Thesis, "Light scattering studies of organic field effect transistors", University of Missouri (2013).

102. X. Liu, X. Zhang, Y. Hou, F. Teng, Z. Lou, "Theoretical investigation on properties of the ground and lowest excited states of a red emitter with donor-p-acceptor structure", Chem. Phys., **381**, 100–104 (2011).

103. M. Arif. K. Yang, L. Li, P. Yu, S. Guha, S. Gangopadhyay, M. Forster, and U. Scherf, "Harvesting triplet excitons for application in polymer solar cell", Appl. Phys. Lett., **94**, 0633071-063373 (2009).

104. W. A. Luhman and R. J. Holmes, "Enhanced exciton diffusion in an organic photovoltaic cell by energy transfer using a phosphorescent sensitizer", Appl. Phys. Lett., **94**, 1533041-1533043 (2009).

105. M. Reufer, P. G. Lagoudakis, M. J. Walter, J. M. Lupton, J. Feldmann, and U. Scherf, "Evidence for temperature-independent triplet diffusion in a ladder-type conjugated polymer", Phys. Rev. B, **74**, 2412011-2412014 (2006).

106. R. R. Lunt, N. C. Giebink, A. A. Belak, J. B. Benziger, and S. R. Forrest, "Exciton diffusion lengths of organic semiconductor thin films measured by spectrally resolved photoluminescence quenching", J. Appl. Phys., **105**, 0537111-0537117 (2009).

107. V. Ern, P. Avakian, and R. E. Merrifield, “Diffusion of triplet exciton in anthracene crystal”, Phys. Rev., **148**, 862-867 (1966).

108. A. J. Cadby, P. A. Lane, H. Mellor, S. J. Martin, M. Grell, C. Giebeler, D. D. C. Bradley, M. Wohlgenannt, C. An, and Z. V. Vardeny, “Film morphology and photophysics of polyfluorene”, Phys. Rev., **62**, 15604-15609 (2000).

109. B. A. Gregg, J. Sprague, and M. W. Peterson, “Long-range singlet energy transfer in perylene bis(phenethylimide) films”, J. Phys. Chem. B, **101**, 5362-5369 (1997).

110. P. W. Blom, V. D. Mihailetchi, L. J. Koster, and D. E. Markov, “Device physics of polymer:fullerene bulk heterojunction solar cell”, Adv. Mater., **19**, 1551-1556 (2007).

111. S. R. Scully and M. D. McGehee, “Effects of optical interference and energy transfer on exciton diffusion length measurements in organic semiconductor”, J. Appl. Phys., **100**, 0349071-0349075 (2006).

112. M. Theander, A. Yartsev, D. Zigmantas, V. Sundström, W. Mammo, M. R. Andersson, and O. Inganäs, “Photoluminescence quenching at a polythiophene/C60 heterojunction”, Phys. Rev. B, **61**, 12957-12963 (2000).

113. V. Bulović, P. E. Burrows, S. R. Forrest, J. A. Cronin, and M. E. Thompson, “Study of localized and extended excitons in 3,4,9,10-perylenetetracarboxylic dianhydride (PTCDA) I. Spectroscopic properties of thin films and solutions”, Chem. Phys., **210**, 1-12 (1996).

114. A. Köhler and H. Bässler, “Triplet states in organic semiconductor”, Mater. Sci. Eng. R., **66**, 71-109 (2009).

115. K. Masuda, Y. Ikeda, M. Ogawa, H. Benten, H. Ohkita, and S. Ito, “Exciton generation and diffusion in multilayered organic solar cells designed by layer-by-layer assembly of poly(p-phenylenevinylene)”, ACS Appl. Mater. Interfaces, **2**, 236-245 (2010).

116. G. Dellepiane, C. Cuniberti, D. Comoretto, G.F. Musso, G. Figari, A. Piaggi, A. Borghesi, “Long-lived photoexcited states in symmetrical polydicarbzolyldiacetylene”, Phys. Rev. B, **48,** 7850-7856 (1993)

117. C. Botta, S. Luzzati, R. Tubino, D. D. C. Bradley, and R. H. Friend, “Photoinduced absorption of polymer solution”, Phys. Rev. B, **48**(20), 14809-14817 (1993).

118 . S. M. R. Rivkin, Photoelectric Effects in Semiconductors (Consultants Bureau, New York, 1964).

119. E. Peeters, A. M. Ramos, S. C. J. Meskers, and R. A. J. Janssen, "Singlet and triplet excitations of chiral dialkoxy-p-phenylene oligomers", J. Chem. Phys., **112**, 9445-9454 (2000).

120. Haugeneder, M. Neges, C. Kallinger, W. Spirkl, U. Lemmer, J. Feldmann, U. Scherf, E. Harth, A. Gügel, and K. Müllen, "Exciton diffusion and dissociation in conjugated polymer/fullerene blends and heterostructures", Phys. Rev. B, **59**, 15346 (1999).

121. D. Markovitsi, Lécuyer, and J. Simon, "One-dimensional triplet energy migration in columnar liquid crystals of octa-substituted pthalocyanines", J. Phys. Chem. **95**, 3620-3626 (1991).

122. S. Chandrasekhar, "Stochastic problems in physics & astronomy", Rev. Mod. Phys., **15**(1), 1-89 (1943).

123. D. C. Northrop and O. Simpson, "Electronic Properties of aromatic hydrocarbons. II. Fluorescence transfer in solid solutions", Proc. R. Soc. London, Ser. A, **234**, 136-149 (1956).

124. J. E. Kroeze, T. J. Savenije, L. P. Candeias, J. M. Warman, and L. D. A. Siebbeles, "Triplet exciton diffusion and delayed interfacial charge separation in a TiO2/PdTPPC bilayer: Monte Carlo simulations", Sol. Energy Mater. Sol. Cells, **85**, 189-203 (2005).

125. K. Paudel, D. Moghe, M. Chandrasekhar, P. Yu, S. Ramasesha, U. Scherf and S. Guha1, "Pressure dependence of singlet and triplet excitons in amorphous polymer semiconductors", EPL, **104**, 270081-270085 (2013).

VITA

Dhanashree Moghe was born in Mumbai (Bombay), India. I attended St. Xavier's College (previously under University of Mumbai, now autonomous), Mumbai, from where I obtained my Bachelors degree in Physics. After completing Masters in Physics from the University of Mumbai, I worked at the Society for Applied Microwave Electronic Engineering and Research (SAMEER, Mumbai, India) as a Research Scientist with the Medical Linear Accelerator group. I came to the University of Missouri-Columbia in Fall-2008 to pursue Ph.D. in the Department of Physics and Astronomy under Dr. Suchi Guha.

After a successful Dissertation Defense, I have joined Dr. Richard Lunt's group as a Research Associate at the Michigan State University in the Department of Chemical Engineering and Materials Science. I will be graduating in May 2014.

PUBLICATIONS

1. **D. Moghe**, G. Dutta, S. Patil, and S. Guha, "*Photocurrent spectroscopic studies of diketopyrrolopyrrole-based statistical copolymers",* Phys. Chem. Chem. Phys., **16**, 4291 (2014).

2. K. Paudel, **D. Moghe**, M. Chandrasekhar, P. Yu, S. Ramasesha, U. Scherf, and S. Guha, "*Pressure dependence of singlet and triplet excitons in amorphous polymer semiconductors",* EPL, **104**, 27008 (2013).

3. **D. Moghe**, P. Yu, C. Kanimozhi. S. Patil, and S. Guha, "*Charge transfer complex states in diketopyrrolopyrrole polymers and fullerene blends: Implications for organic solar cell efficiency",* Appl. Phys. Lett., **99**, 233307 (2011).

4. M. Samiullah, **D. Moghe**, U. Scherf, and S. Guha, "*Diffusion length of triplet excitons in organic semiconductors",* Phys. Rev. B, **82**, 205211 (2010).